Experimental and Theoretical Aerodynamic Characteristics of a High-Lift Semispan Wing Model

Zachary T. Applin
and Garl L. Gentry, Jr.

NASA

Experimental and Theoretical Aerodynamic Characteristics of a High-Lift Semispan Wing Model

Zachary T. Applin
and Garl L. Gentry, Jr.
Langley Research Center
Hampton, Virginia

Summary

A study was conducted to compare experimental and theoretical aerodynamic characteristics of a high-lift semispan wing configuration. Experimental data were obtained from a large semispan wing model that incorporated a slightly modified version of the NASA Advanced Laminar Flow Control (LFC) airfoil section. The experimental investigation was conducted in the Langley 14- by 22-Foot Subsonic Tunnel at test-section dynamic pressures of 15 and 30 psf. This provided reference chord Reynolds numbers of 2.36×10^6 and 3.33×10^6, respectively. A two-dimensional airfoil code and a three-dimensional panel code were used to obtain aerodynamic predictions. Two-dimensional data were corrected for three-dimensional effects. Comparisons between predicted and measured values were made for the cruise configuration and for various high-lift configurations. Both codes predicted lift and pitching-moment coefficients that agreed well with experiment for the cruise configuration. These parameters were overpredicted for all high-lift configurations. Drag coefficient was underpredicted for all cases. Corrected two-dimensional pressure distributions typically agreed well with experiment, whereas the panel code overpredicted the leading-edge suction peak on the wing.

One important feature missing from both these codes was a capability for separated flow analysis. The major cause of disparity between the measured data and predictions presented herein was attributed to separated flow conditions.

Introduction

The purpose of the present effort was to compare experimental and theoretical aerodynamic characteristics of a high-lift semispan wing configuration. The experimental data were obtained during an investigation in the Langley 14- by 22-Foot Subsonic Tunnel. Theoretical predictions were obtained with a two-dimensional airfoil code and a three-dimensional panel code.

Current analytical techniques provide adequate aerodynamic predictions for basic airplane configurations which have little or no flow separation. However, these techniques typically lack the capability to determine aerodynamic characteristics for conditions of extensive flow separation. Significant flow separation can exist on airplanes for several common operational situations. For example, separation may be present on the upper surface of trailing-edge flaps during high-lift takeoff and landing conditions. In addition, recent geometries developed for highly maneuverable fighter airplanes are designed for operation at extreme angles of attack where separated flow is certain to occur.

The primary interest of the present study is in configurations with trailing-edge and leading-edge flaps deployed, where highly viscous interactions and flow separation cause inaccurate and sometimes misleading predictions of aerodynamic characteristics. However, comparisons are also presented for the cruise and trailing-edge-flap-only configurations.

The airfoil code used to calculate two-dimensional aerodynamic characteristics was the Multi-Component Airfoil (MCARF) program described in references 1 and 2. This program combines boundary-layer solutions with potential flow pressure distributions to obtain viscous aerodynamic characteristics of airfoil geometries.

The panel code, VSAERO, calculates nonlinear aerodynamic characteristics of partial or complete configurations in the subsonic flow regime (refs. 3 and 4). Nonlinear effects of vortex flow interaction with flow fields and surfaces are treated with wake relaxation techniques in an iterative procedure. In an approach that is similar to MCARF, VSAERO can account for viscous effects by coupling a potential flow solution with strip boundary-layer calculations. Several wing configurations were analyzed to determine the viscous effect as predicted by VSAERO. The difference between viscid and inviscid solutions was insignificant; therefore, only inviscid solutions are presented herein.

Symbols

All longitudinal aerodynamic data are referred to the wind axis system. Dimensions of the cruise configuration were used to nondimensionalize aerodynamic force and moment data.

b	wing semispan, 116.01 in.
C_D	drag coefficient, $\dfrac{\text{Drag}}{q_\infty S}$
C_L	lift coefficient, $\dfrac{\text{Lift}}{q_\infty S}$
C_{L_α}	lift-curve slope, per deg
C_m	pitching-moment coefficient about quarter-chord, $\dfrac{\text{Pitching moment}}{q_\infty S c}$
C_p	static pressure coefficient, $\dfrac{p_s - p_\infty}{q_\infty}$
c	reference wing chord, 39.37 in.
c_l	section lift coefficient, $\dfrac{\text{Lift}}{q_\infty c}$
p_s	surface static pressure, lb/ft^2

p_∞	free-stream static pressure, lb/ft^2
q_∞	free-stream dynamic pressure, lb/ft^2
S	reference wing area, 31.72 ft^2
x, y, z	coordinates of pressure taps, in.
α	angle of attack of WRP, deg
α_{MCARF}	MCARF angle of attack used for pressure distribution comparisons, deg
δ_{LE}	leading-edge flap deflection angle, positive trailing edge down, deg
δ_{TE}	trailing-edge flap deflection angle, positive trailing edge down, deg
η	$= \frac{y}{b}$

Abbreviations:

L.E.	leading edge
LFC	laminar flow control
T.E.	trailing edge
WRP	wing reference plane of cruise configuration

Test Setup

The unswept semispan wing model was tested in the Langley 14- by 22-Foot Subsonic Tunnel which is a closed, single-return, atmospheric wind tunnel with a test section 14.50 ft high by 21.75 ft wide by 50.00 ft long. (See ref. 5.) The test-section dynamic pressure is continuously variable from 0 to 144 psf. The tunnel is equipped with a floor boundary-layer removal system consisting of a floor-mounted suction grid located 8.2 ft upstream of the wing leading edge. The suction grid spans the floor of the test section between the tunnel walls and reduces the boundary-layer thickness to approximately 1.6 in. at the wing location for the empty tunnel condition. The model was mounted vertically, protruding through the floor, on a six-component strain-gauge balance which was located below a 15.8-ft-diameter turntable which could be rotated throughout the angle-of-attack range of the wing. Angle of attack of all configurations was referenced to the wing reference plane of the cruise configuration. The yaw angle of the turntable was detected by a digital shaft encoder geared to the turntable mechanism. This provided an angle-of-attack accuracy to within ±0.02°.

The 116.01-in. semispan, rectangular, untwisted wing model had a 39.37-in. chord incorporating a slightly modified version of the NASA Advanced Laminar Flow Control (LFC) airfoil section presented in references 6 through 8. Maximum thickness of the airfoil section was 0.13c. The unmodified airfoil section was designed to provide shock-free flow over the upper surface at high subsonic Mach numbers as described in reference 6. The current study investigates the low-speed characteristics of the modified airfoil shape, with and without high-lift devices. Modifications to the airfoil shape included a shift in the lower surface lobe rearward by 2 percent of the chord and a slight increase in trailing-edge camber. These modifications allowed sufficient length in the chordwise direction, forward of the lower surface lobe, for storage of a Krueger-type flap of up to 12 percent chord. A Krueger-type flap was chosen because possible surface discontinuities when stowed (i.e., steps, gaps) would be in a region of favorable pressure gradients generated by the airfoil contour. (See ref. 6.) No analysis has been made of the internal volume required for storage of the Krueger-type flap or for the necessary deployment mechanism.

This model was fabricated to investigate aerodynamic characteristics for the high-lift configuration (a condition for which LFC is not practical). Therefore, no provisions were made for an LFC suction system.

The model high-lift components included either a 0.10c or a 0.12c full-span leading-edge flap and a full-span 0.25c trailing-edge flap. All components of this semispan model had rounded tips. A sketch of the model planform and photographs of the model installed in the tunnel are presented in figure 1. A single row of pressure taps located at $\frac{y}{b} = 0.44$ was used to obtain surface pressure distributions. Coordinates of the wing airfoil section for the cruise and main element of the high-lift configurations are given in terms of the locations of surface pressure taps and are presented in tables I and II, respectively. Coordinates of the trailing-edge flap are presented in table III; coordinates of the two leading-edge flaps are presented in table IV. Section contours of the configurations tested during this investigation are shown in figure 2.

The leading- and trailing-edge flaps were positioned using the definitions for deflection, gap, and overlap presented in reference 9. Reference lines for these definitions pass through the leading and trailing edge of each component, including the main element of the high-lift configurations. For the trailing-edge flap, the gap and overlap were 0.02c and 0.00c, respectively. For both leading-edge flaps, the gap and overlap were 0.012c and 0.016c, respectively. These settings were used for all deflection angles tested in this investigation.

The wing was fabricated from solid aluminum by a numerically controlled milling machine. The

resultant contour was within ±0.005 in. of the specified airfoil coordinates. Surface pressure tubes were routed internally to pressure measurement instrumentation located below the tunnel floor. For configurations with the trailing-edge flap installed (fig. 1(b)), the cruise trailing edge was replaced by a cove section which provided support brackets and pressure-tube routing recesses for the flap pressure tubes. Leading-edge flaps were supported by brackets mounted on the lower surface of the leading edge of the cruise wing. Pressure tubes from the high-lift components were routed externally along the support brackets ($\eta = 0.377$) to the wing. These tubes were then internally routed through the wing to the pressure instrumentation located below the tunnel floor. The external tubes were tightly taped to the flap brackets and streamlined with the use of modeling clay to produce a smooth surface. Modeling clay was also used to streamline the remaining flap brackets not used to route pressure tubes. Spanwise locations of the flap bracket centerlines are given in table V.

There was a 1.5-in-wide gap between the wing upper surface and the tunnel floor plates (0.25 in. thick) where the wing protruded through the tunnel floor. This gap was provided to prevent fouling when aerodynamic loading caused the balance and wing to deflect. A 1.0-in-wide gap was provided for the lower surface. To reduce airflow through this gap, a 2-in-thick pad of closed-cell foam rubber (which overlapped the tunnel floor) was attached to the wing just below the tunnel floor. An electrical fouling circuit alerted the tunnel operator if any contact occurred between the wing and tunnel floor.

Boundary-layer transition strips 1/8 in. wide were applied using No. 60 Carborundum grit. The transition roughness was sized according to the procedure outlined in reference 10. These transition strips were located on both the upper and lower surfaces at the 5-percent-chord station for the cruise configuration and extended across the entire span. For the high-lift configuration, the same grit was located 2 in. from the leading edge on the main component and 1 in. from the leading edge on all the flaps.

Pressure measurements were obtained with an electronically scanned pressure (ESP) system. This system consisted of modules which contained a 720-psf-range silicon pressure transducer for every port. These transducers were operated as 144-psf-range transducers by the addition of sensitizing electronics. The manufacturer's quoted accuracy for the system when operated in this range is ±0.5 psf. The pressure transducers were referenced to atmospheric pressure and had an over range capability. Sixteen pressure ports near the leading edge of the wing were connected in parallel to a 720-psf and a 144-psf trans-

ducer to assure accurate measurement of pressure above 144 psf. On-line calibration was possible with this system and was done before every run to maintain a high degree of accuracy. When a data point was measured, each of the pressure transducers was scanned electronically at up to 20 000 measurements per second; thus all pressure data were acquired at essentially the same time.

Aerodynamic force and moment measurements were obtained with an existing six-component, strain-gauge balance, which had previously been used on a semispan wing similar in size to the LFC wing. Balance load characteristics, as well as its effect on the accuracy of aerodynamic coefficients, are presented in table VI. The previous model incorporated an NACA 0012 airfoil section (ref. 11). The LFC wing used the same mounting hardware as used for the NACA 0012 wing. It was determined that the existing balance did not have sufficient load capacity to allow operation of the LFC wing at the maximum lift condition (stall angle of attack). The investigation of the aerodynamic characteristics of the LFC wing was therefore limited to moderate angles of attack.

Test Procedures

The model was tested in four different configurations as shown in the following table:

Configuration	δ_{TE}, deg	δ_{LE}, deg
Cruise		
Trailing-edge flap only	15	
10-percent leading-edge flap	15, 30	−50, −55, −60
12-percent leading-edge flap	15, 30	−50, −60

The angle-of-attack range varied with model configuration and was limited by the load capacity and stability of the balance. Test-section dynamic pressures of 15 and 30 psf (Mach numbers of 0.10 and 0.14) were used throughout the investigation; this provided reference chord Reynolds numbers of 2.36×10^6 and 3.33×10^6, respectively. Unfortunately, due to a malfunction in the data acquisition system, no data were obtained at $q_\infty = 30$ psf for the 10-percent leading-edge flap configuration with $\delta_{LE} = -50°$ and $\delta_{TE} = 15°$.

Although all six force and moment components were measured with the balance, only the longitudinal aerodynamic data are presented. Since the model was mounted perpendicular to the tunnel

floor, model angle-of-attack variation (referenced to the WRP) was accomplished by yawing the tunnel floor turntable. A correction for blockage effects on the model was applied to the free-stream dynamic pressure by using the method presented by Herriot in reference 12. A correction for jet-boundary effects was applied to the angle of attack by using the method described by Polhamus in reference 13. Wall corrections were estimated with the procedure of Heyson in reference 14. The wall corrections on the aerodynamic data were small for the conditions investigated and consequently were not used.

Experimental Results

Longitudinal Aerodynamic Characteristics

Longitudinal aerodynamic characteristics for all configurations are presented in figures 3 through 6. Only two configurations were tested through the stall angle of attack: the trailing-edge flap configuration ($\delta_{TE} = 15°$, fig. 4) and the 10-percent leading-edge flap configuration ($\delta_{LE} = -60°$, $\delta_{TE} = 15°$, fig. 5(e)), both at $q_\infty = 15$ psf.

The pitching-moment coefficient exhibits a fairly neutral slope throughout the angle-of-attack range for most configurations. The only exception is in the vicinity of $\alpha = -4°$ to $0°$ for both leading-edge flap configurations. In this range, the pitching-moment coefficient becomes more negative as angle of attack is increased. The lift coefficient displays a large increase in slope over the same angle-of-attack range. This phenomenon is due to extensive flow separation over the wing and flaps at negative angles of attack. At positive angles of attack, the flow is mostly attached and therefore generates a larger lift-curve slope.

Effect of Trailing-Edge Flap Deflection

The effect of trailing-edge flap deflection on the longitudinal aerodynamic characteristics of both leading-edge flap configurations is presented in figures 7 and 8. The increment in lift and pitching-moment coefficients due to a differential trailing-edge flap deflection of 15° is presented in figure 9 for $q_\infty = 30$ psf.

For the trailing-edge flap configuration (fig. 9(a)), the increments in lift and pitching-moment coefficients between δ_{TE} of 0° (cruise configuration) and 15° are almost constant over the angle-of-attack range presented. These results indicate very little flap separation for these angles.

Both leading-edge flap configurations exhibit characteristics drastically different from those of the trailing-edge flap configuration. Data presented for

these configurations were obtained with increments between $\delta_{TE} = 15°$ and 30°, again providing an increment in trailing-edge flap deflection of 15°. For negative angles of attack, large changes in increments in lift and pitching-moment coefficients occur with increasing angle of attack, particularly for the 10-percent leading-edge flap configuration. This indicates transition from a condition of largely separated flow to a condition of basically attached flow. Smaller changes are noted with further increases in angle of attack, since the flow is mostly attached.

Pressure Distributions

Pressure distributions at selected angles of attack are presented in figures 10 through 15 for the cruise, trailing-edge flap, and both leading-edge flap configurations with $\delta_{TE} = -55°$. As previously discussed, this airfoil contour was designed to generate a favorable pressure distribution on the lower surface near the leading edge. This can be seen in the pressure distribution plots for the cruise and trailing-edge flap configurations for $\alpha = 4°$ or greater. For leading-edge flap configurations this phenomenon occurs at slightly greater angles of attack.

Flow separation over the upper surface of the trailing-edge flap is observed for both leading-edge flap configurations with $\delta_{TE} = 30°$ (figs. 13(c)–(e), 15(a), and 15(c)–(f)). This is evident by the very steep decline in the magnitude of the pressure coefficient near the leading edge of the trailing-edge flap followed by a flat profile over the remaining portion of the flap. Theoretical methods typically have the most difficulty predicting this characteristic.

Prediction Techniques

Airfoil Code

The airfoil code used to calculate the two-dimensional aerodynamic characteristics of configurations presented herein was the Multi-Component Airfoil (MCARF) program described in references 1 and 2. This program combines an inviscid potential-flow solution with both an ordinary boundary-layer solution and a confluent boundary-layer solution (for multiple components) to determine the overall two-dimensional, viscous aerodynamic characteristics of a multicomponent configuration.

The primary reason for selecting this particular program was its confluent boundary-layer analysis capability. This option allows for merging of the upper surface boundary layer with slot efflux to improve prediction accuracy of the pressure distributions. This program was designed to account for the highly viscous interactions present on many high-lift

configurations. The MCARF program was also used as a design tool to define geometries and positions of the high-lift system components for this particular model as described in reference 15.

The MCARF program represents each airfoil element using closed polygons composed of individual linear segments. These segments are distributed based on the curvature of the airfoil surface, with smaller segments used in regions of high curvature such as the leading and trailing edges. This procedure is described in reference 2. The number of segments used to represent each configuration is presented in table VII. Figure 16(a) shows the MCARF representation of the cruise configuration.

The output of this program is in the form of pressure coefficient distributions and lift, drag, and pitching-moment coefficients and is presented for individual components as well as for the overall configuration. In this report, only the aerodynamic characteristics for the overall configuration are presented.

Panel Code

The panel code used to calculate three-dimensional aerodynamic characteristics was VSAERO, described in references 3 and 4. VSAERO is a low-order panel method which uses a piecewise constant source and doublet distribution to model arbitrary configurations in the subsonic flow regime.

VSAERO was chosen primarily because of its ease of use in paneling configuration geometries and its low cost compared with other panel methods. Scheib and Sandlin (ref. 16) conducted a comparison of various panel methods and selected VSAERO for basically the same reasons. An aerodynamic configuration is represented with quadrilateral panels. For this particular model, panels were distributed evenly along the span. Panels were distributed in the chordwise direction of each component based on a cosine distribution resulting in increased panel density near the leading and trailing edges. The number of panels used to represent each configuration is presented in table VIII. Figures 16(b) and (c) show the VSAERO representation of the cruise configuration.

Nonlinear effects of vortex flow interaction with configuration flow fields and surfaces are treated in an iterative procedure with wake relaxation techniques. During the course of the present study, the VSAERO program was under continued development to add various capabilities. The scope of the program version used to calculate aerodynamic characteristics presented in this report included a flexible wake relaxation option and a viscous-potential iteration procedure. The number of wake panels and iterations is selected by the user. The number of wake panels and iterations used was 212 wake panels and 6 iterations for the cruise configuration, 378 wake panels and 8 iterations for the trailing-edge configuration, and 806 wake panels and 10 iterations for both of the leading-edge flap configurations.

In an approach that is similar to MCARF, VSAERO is designed to combine potential flow solutions with boundary-layer calculations to determine aerodynamic characteristics. As discussed previously, several configurations (cruise, trailing-edge flap only, and 10-percent leading-edge flap) were analyzed with up to 10 boundary-layer iterations. The differences between the viscid and inviscid solutions were insignificant. For example, the cruise configuration inviscid solution predicted $C_L = 1.080$ and $C_D = 0.061$ at $\alpha = 12°$. After 10 boundary-layer iterations, the viscid solution predicted $C_L = 1.050$ and $C_D = 0.060$ at $\alpha = 12°$. These differences did not warrant the additional expenses incurred by the viscid solution option.

One important option under development, but not functional during the present study, was modeling of extensive flow separation. As evident by many of the measured pressure distributions presented, extensive separation exists on the high-lift components at certain angles of attack. A functional separated flow model would be invaluable in the prediction of aerodynamic characteristics under these conditions.

Theoretical and Experimental Results

Longitudinal Aerodynamic Characteristics

Predicted and measured longitudinal aerodynamic characteristics at $q_\infty = 30$ psf are presented in figures 17 through 20. In all figures, measured values are plotted in a symbol-only format.

For the cruise configuration (fig. 17), VSAERO predictions of lift coefficient agree well with experimental results over most of the angle-of-attack range. Two-dimensional lift coefficients determined by MCARF were used to calculate a three-dimensional lift coefficient using lifting-line theory. This calculated three-dimensional lift coefficient agrees well with measured data for this configuration. In addition, an induced drag increment was added to the MCARF drag prediction. Both codes greatly underpredict the drag coefficient at large positive and negative angles of attack, in addition to slightly overpredicting the pitching-moment coefficient at positive angles of attack.

For the trailing-edge flap configuration (fig. 18), three-dimensionally corrected MCARF and

5

VSAERO overpredict lift coefficient and underpredict drag coefficient, although MCARF predictions are closer to the measured data. The pitching-moment coefficient is again overpredicted by both methods. The underprediction of drag agrees with the results obtained by Scheib and Sandlin (ref. 16) for VSAERO.

For both leading-edge flap configurations (figs. 19 and 20), MCARF predictions again match the experimental results better than VSAERO. Neither code predicts the large discontinuity in the lift curve between $\alpha = -5°$ and $0°$, primarily because of extensive flow separation for these angles as discussed in a later section.

Lift-Curve Slope

Predicted and measured lift-curve slopes are presented in figures 21 through 24. For the cruise and trailing-edge flap configurations, the lift-curve slope was determined from a linear least-squares curve fit to the data between $\alpha = 0°$ and $8°$. For both leading-edge flap configurations, the least-squares curve fit was applied to the data between $\alpha = 0°$ and $10°$. The prediction of lift-curve slope by both codes is in excellent agreement with measured results for most configurations. The only large differences are for both leading-edge flap configurations with $\delta_{LE} = -55°$, $\delta_{TE} = 15°$.

Effect of Trailing-Edge Flap Deflection

The effect of trailing-edge flap deflection as predicted by MCARF and VSAERO is presented in figures 25 and 26. Figure 27 presents the predicted and measured effects of trailing-edge flap deflection on lift and pitching-moment coefficients.

For the trailing-edge-flap-only configuration, both codes predict trends well but overpredict the increment in lift and pitching-moment coefficients.

For leading-edge flap configurations, neither method predicts the large change in lift and pitching-moment coefficients at negative angles of attack. As previously discussed, this phenomenon is associated with severe flow separation and is not modeled by either of the prediction methods. For these configurations, not even the trends of predicted results appear to be reliable indicators of the measured results.

Pressure Distributions

Predicted and measured pressure distributions at $q_\infty = 30$ psf are presented in figures 28 through 31 for selected angles of attack.

MCARF predictions are, by definition, two-dimensional and provide pressure distributions that are not appropriate for the three-dimensionally corrected MCARF lift coefficients. Therefore, a method for determining MCARF pressure distributions that were appropriate for comparison with measured data was devised. This simply amounted to calculating MCARF pressure distributions at an angle of attack which had a lift coefficient (two-dimensional) equivalent to the three-dimensionally corrected MCARF lift coefficient.

The following table shows the model angle of attack and the appropriate MCARF angle of attack, as discussed, for each wing configuration:

Configuration	α, deg	α_{MCARF}, deg
Cruise	8	5
T.E. flap only	8	3
10-percent L.E. flap, $\delta_{TE} = 15°$	10	4
10-percent L.E. flap, $\delta_{TE} = 30°$	10	2
12-percent L.E. flap, $\delta_{TE} = 15°$	10	4
12-percent L.E. flap, $\delta_{TE} = 30°$	10	2

For the cruise configuration, pressure distributions predicted by both codes have reasonably good agreement with the measured pressure distribution (fig. 28). The only discrepancies are on the upper surface at the leading edge and the lower surface lobe.

For the trailing-edge flap configuration (fig. 29), VSAERO predictions greatly overpredict the suction peak on the wing, whereas MCARF shows good agreement with measured data. Both codes predict pressure distributions that agree well with measured trailing-edge flap pressures.

In general, for both leading-edge flap configurations (figs. 30 and 31), MCARF predictions are in good agreement with experiment. The only exceptions are for cases with $\delta_{TE} = 30°$. VSAERO overpredicts the leading-edge suction peak for each component. Typically, large interactions exist between leading-edge flap and wing flow fields. It is possible that the discrepancy in the calculations of the leading-edge flap pressure distribution is, in large part, responsible for the inaccurate determination of the wing pressure distribution.

Concluding Remarks

A study was conducted to compare experimentally determined aerodynamic characteristics of a high-lift, semispan wing configuration with calculated results by a two-dimensional airfoil code (MCARF) and a three-dimensional panel code (VSAERO). A two-dimensional lift coefficient was used to calculate a three-dimensional lift coefficient

using lifting-line theory and an induced-drag increment added to the two-dimensional drag coefficient. Comparisons between predicted and measured values were made for the cruise and trailing-edge flap configurations. However, primary interest was in the leading-edge flap configurations because of highly viscous interactions and extensive flow separation usually present for these configurations. These phenomena typically cause poor predictions by theoretical techniques.

VSAERO calculations agreed well with measured lift coefficients for the cruise configuration over most of the angle-of-attack range. Three-dimensional lift coefficients from the MCARF two-dimensional values using lifting-line theory also agreed well with measured data. Drag coefficient was underpredicted by both methods. Pitching-moment coefficient calculations from both methods were approximately the same and were in fairly good agreement with experimental results.

Both prediction methods overpredicted lift and pitching moment and underpredicted drag for the trailing-edge flap and leading-edge flap configurations. VSAERO and MCARF calculations of lift-curve slope were in excellent agreement with experimentally determined slopes for all configurations' except for both leading-edge flap configurations with a trailing-edge flap deflection of 15°.

The effect of trailing-edge flap deflection was not predicted correctly by either code. Calculated trends were in good agreement with experimental results for the trailing-edge flap configuration, but the magnitudes differed significantly. Because large areas of

flow separation existed for the leading-edge flap configurations, neither code provided good predictions of trends or magnitudes.

Predicted pressure distributions were compared with experiment at selected angles of attack. A method was devised to determine the two-dimensional pressure distribution that was appropriate for the three-dimensionally corrected lift coefficient. For the cruise configuration, calculated pressure distributions agreed fairly well with measured values. MCARF predictions agreed well with measured data, whereas VSAERO greatly overpredicted the leading-edge suction peak for the high-lift configurations. The only large discrepancies for MCARF were on the trailing-edge flap with a deflection of 30°.

For the configurations presented herein, the two-dimensional analysis (MCARF) proved important in the design of basic geometries of the high-lift system as discussed in NASA Conference Publication 2218, pages 43–61. Three-dimensional corrections proved to be a viable technique for using MCARF results to predict aerodynamic characteristics of the finite span model. An important feature lacking in both prediction techniques was a separated flow model. As indicated by the comparisons presented in this report, the major cause of disparity between predicted and experimental results was flow separation.

Appendix

Integration of Pressure Distributions

Pressure distributions presented in this report were numerically integrated to obtain longitudinal aerodynamic coefficients. These values were compared with aerodynamic coefficients determined from balance force and moment measurements. One reason for making this comparison was to provide a mechanism for cross-checking the balance and pressure measurements. The assumption was made that the constant span load assumed by integration of pressures measured at a single chordwise station near the midspan ($\eta = 0.44$) is comparable in magnitude with the actual span load which has a spanwise variation. This is depicted graphically in figure A1 for the cruise configuration. The spanwise distribution of lift coefficient as predicted by VSAERO is compared with the lift coefficient determined from pressure measurements. It was assumed that VSAERO predictions of span load distribution are indicative of the actual conditions on the wing.

For the cruise configuration (fig. A2), there is excellent agreement between balance measurements and pressure distribution integrations. The only exception is for the drag polar at large positive angles of attack. Similar characteristics existed for the trailing-edge flap configuration (fig. A3) and both leading-edge flap configurations (figs. A4 and A5). There is surprisingly good agreement between lift and pitching-moment coefficients for some of the leading-edge flap configurations.

As evidenced by the data in figures A2 through A5, both techniques were functioning properly. The differences between the data obtained from each technique were generally as expected. For example, lift coefficient determined from pressure distribution integration was expected to be greater than that determined from balance measurements. The balance measured the entire lift which, as mentioned before, varied over the span of the model, whereas the lift coefficient determined from pressure integration was assumed constant across the span.

The drag coefficient calculated from pressure distribution integration would naturally be smaller than that determined from balance measurements. In addition to not accounting for the influence of the finite span, the pressure distribution also does not account for drag due to surface friction.
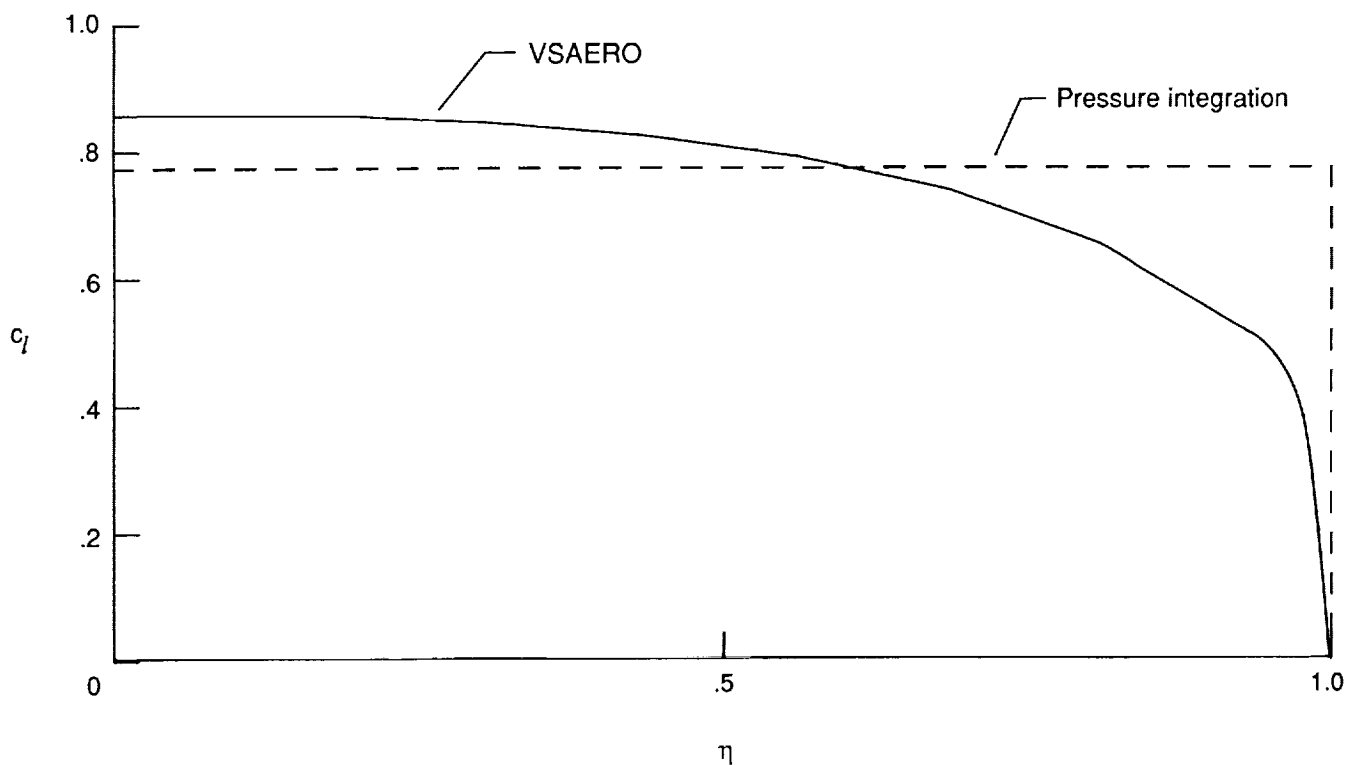
Figure A1. Estimation of span load characteristics for cruise configuration. $\alpha = 8°$.
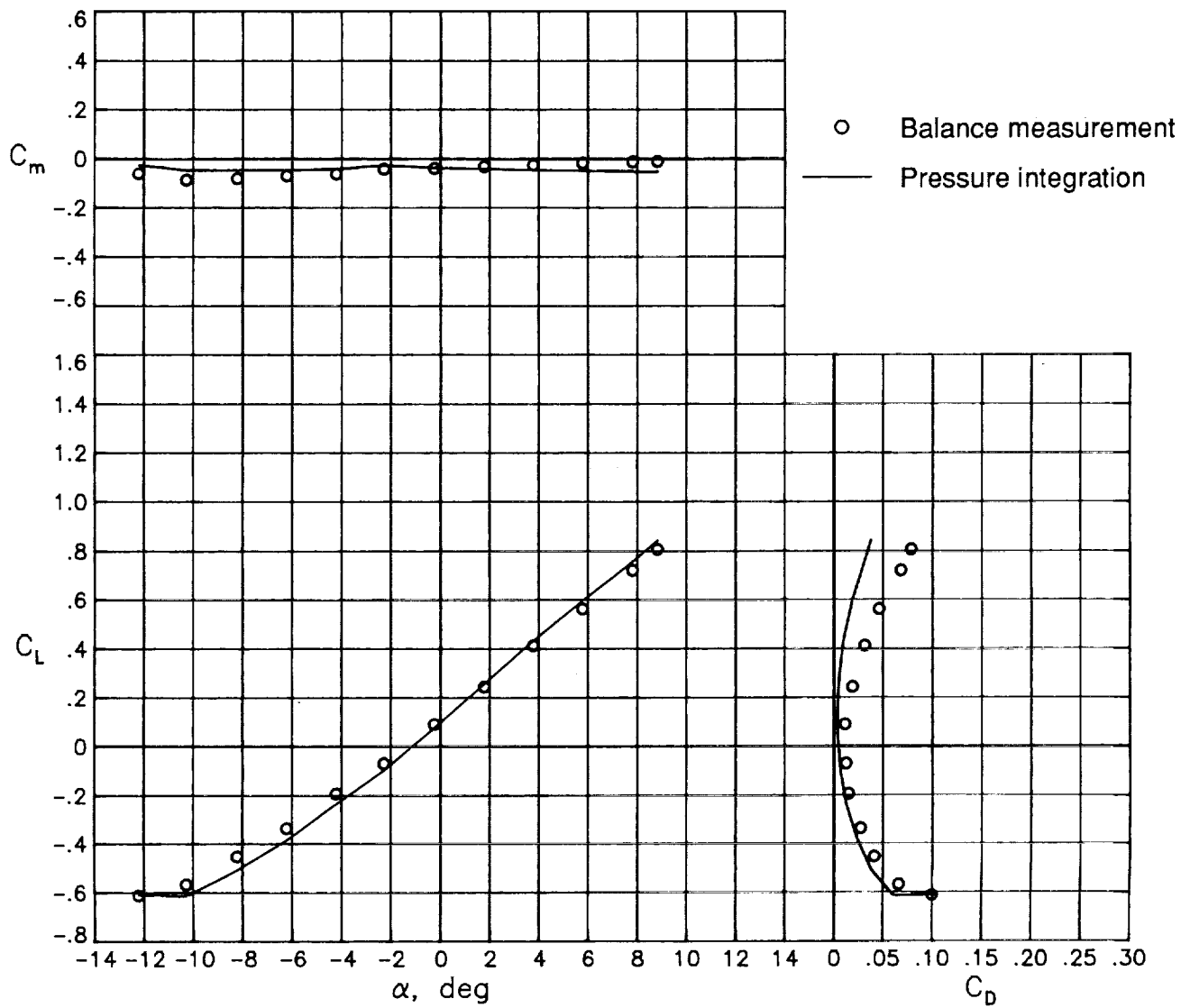
Figure A2. Longitudinal aerodynamic coefficients determined from balance measurements and pressure distribution integration for cruise configuration. $q_\infty = 30$ psf.
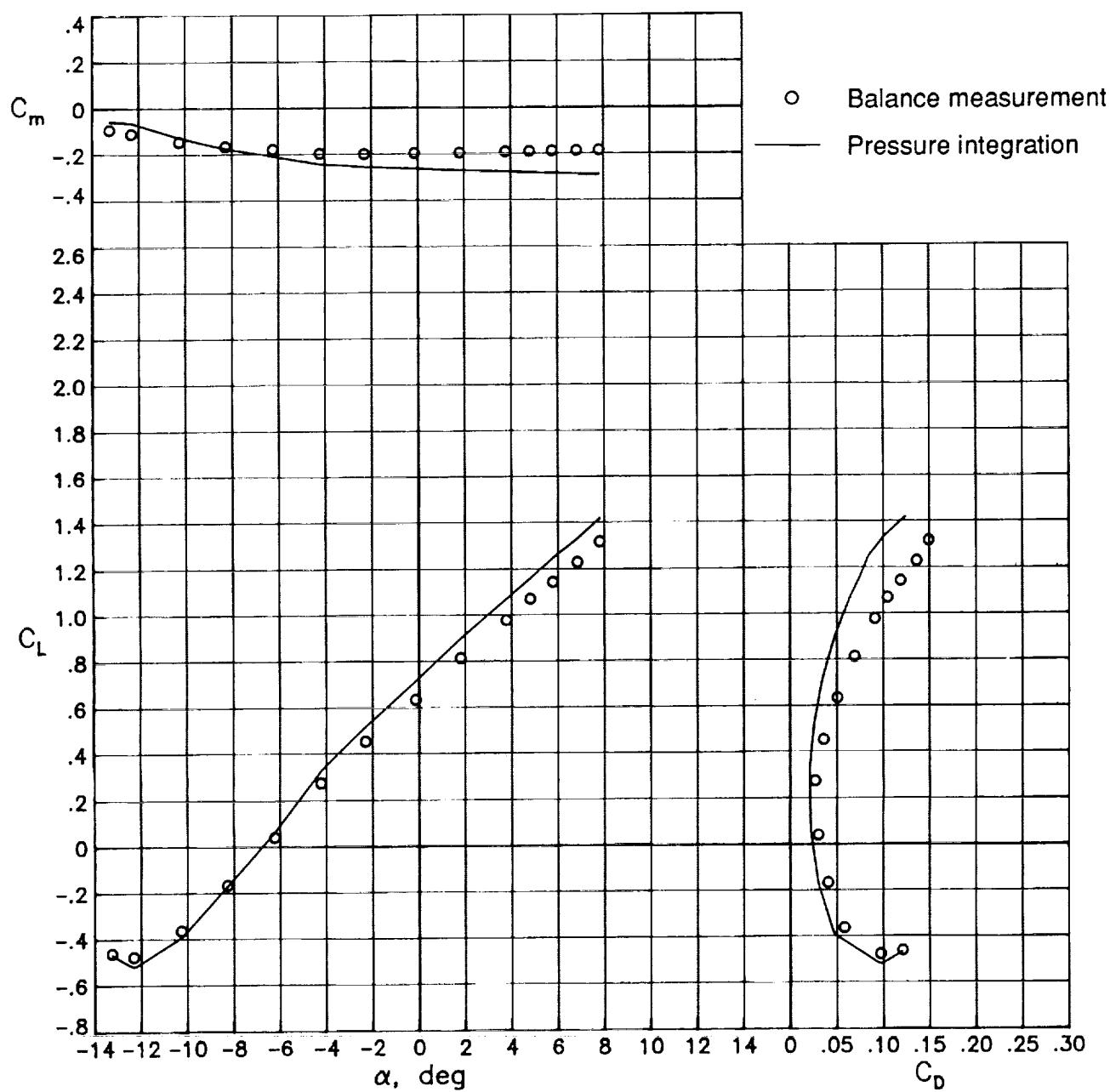
Figure A3. Longitudinal aerodynamic coefficients determined from balance measurements and pressure distribution integration for trailing-edge flap configuration. $q_\infty = 30$ psf; $\delta_{TE} = 15°$.
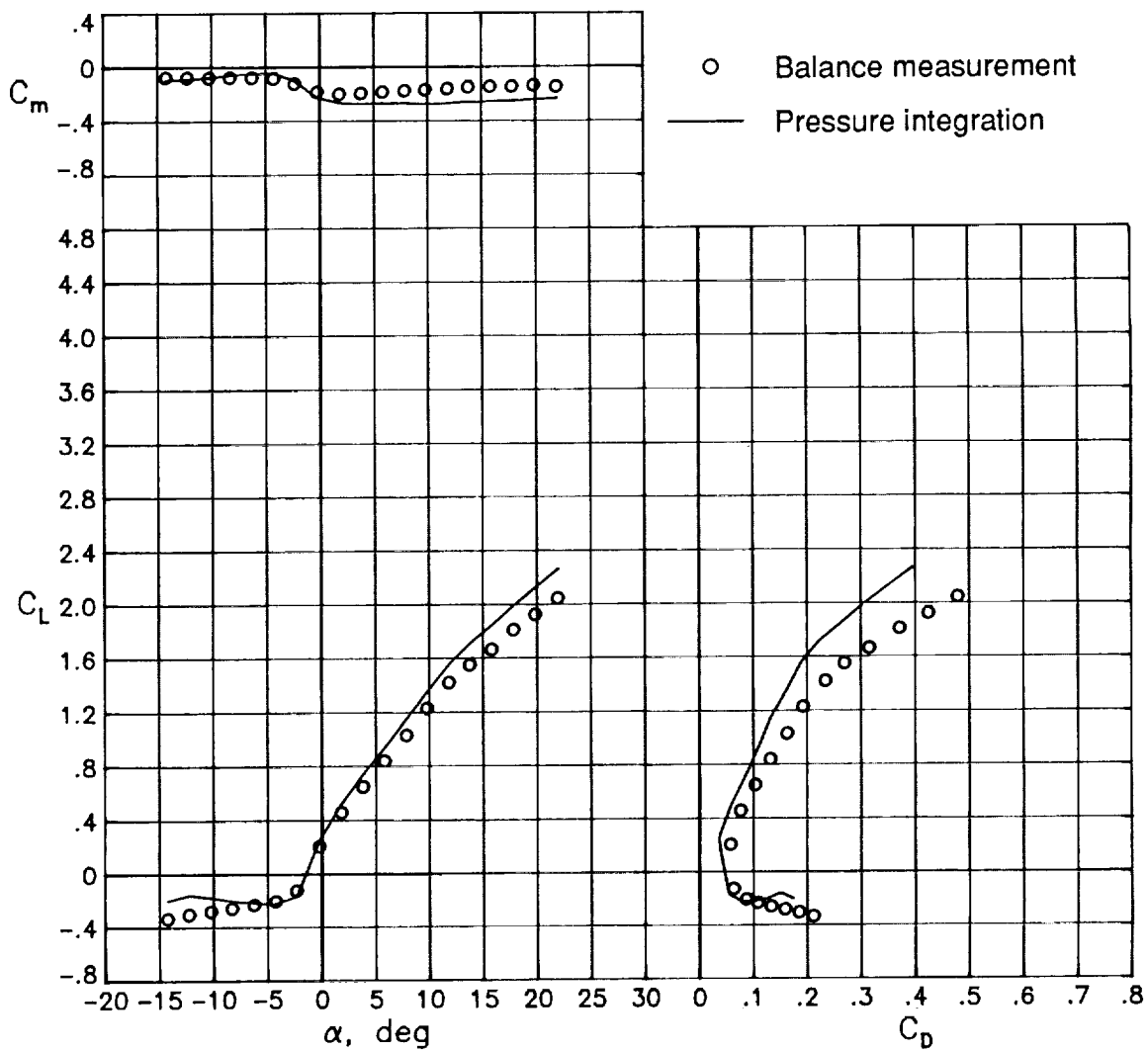
(a) $q_\infty = 15$ psf; $\delta_{LE} = -50°$; $\delta_{TE} = 15°$.

Figure A4. Longitudinal aerodynamic coefficients determined from balance measurements and pressure distribution integration for 10-percent leading-edge flap configuration.
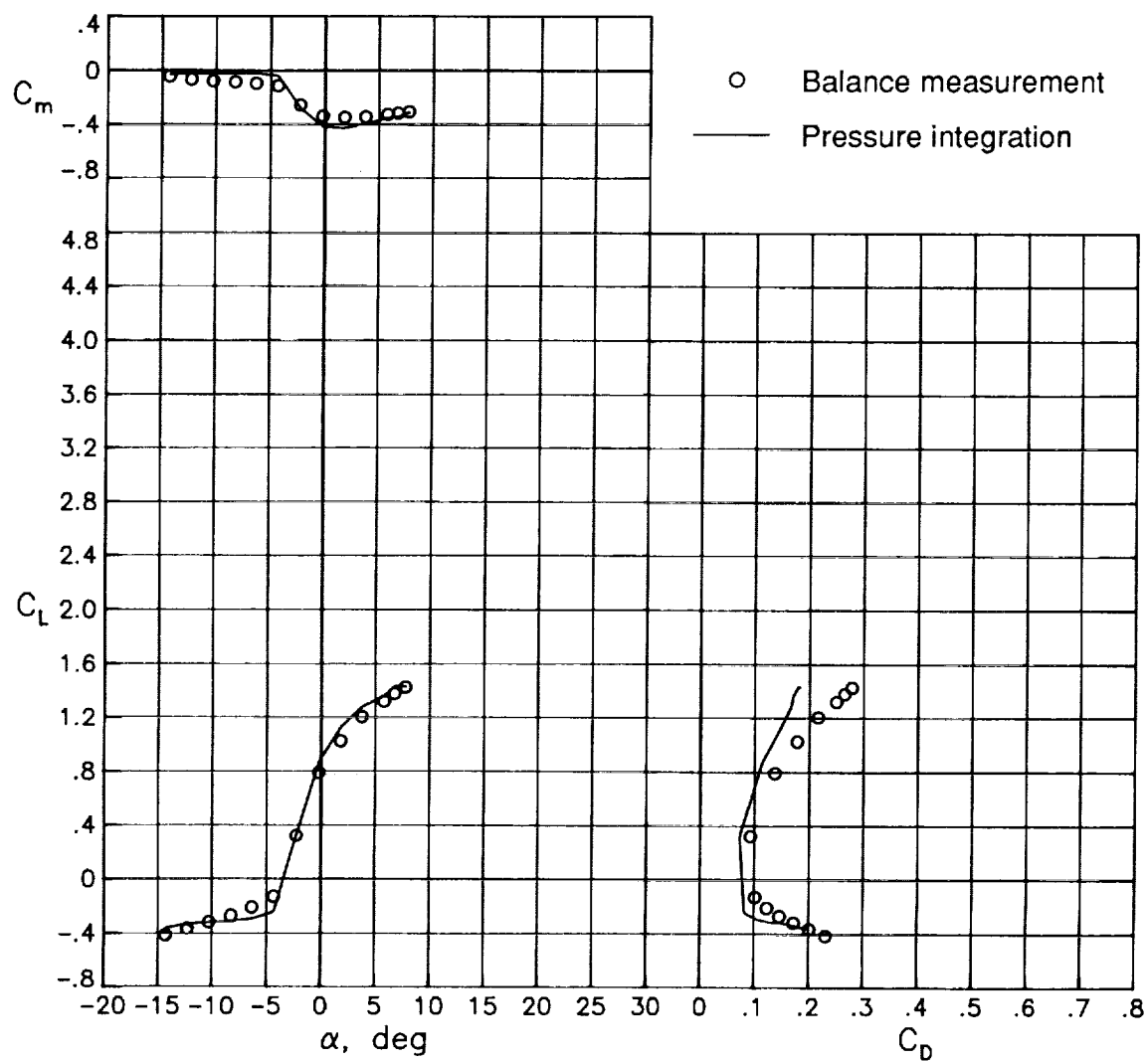
(b) $q_\infty = 30$ psf; $\delta_{LE} = -50°$; $\delta_{TE} = 30°$.

Figure A4. Continued.
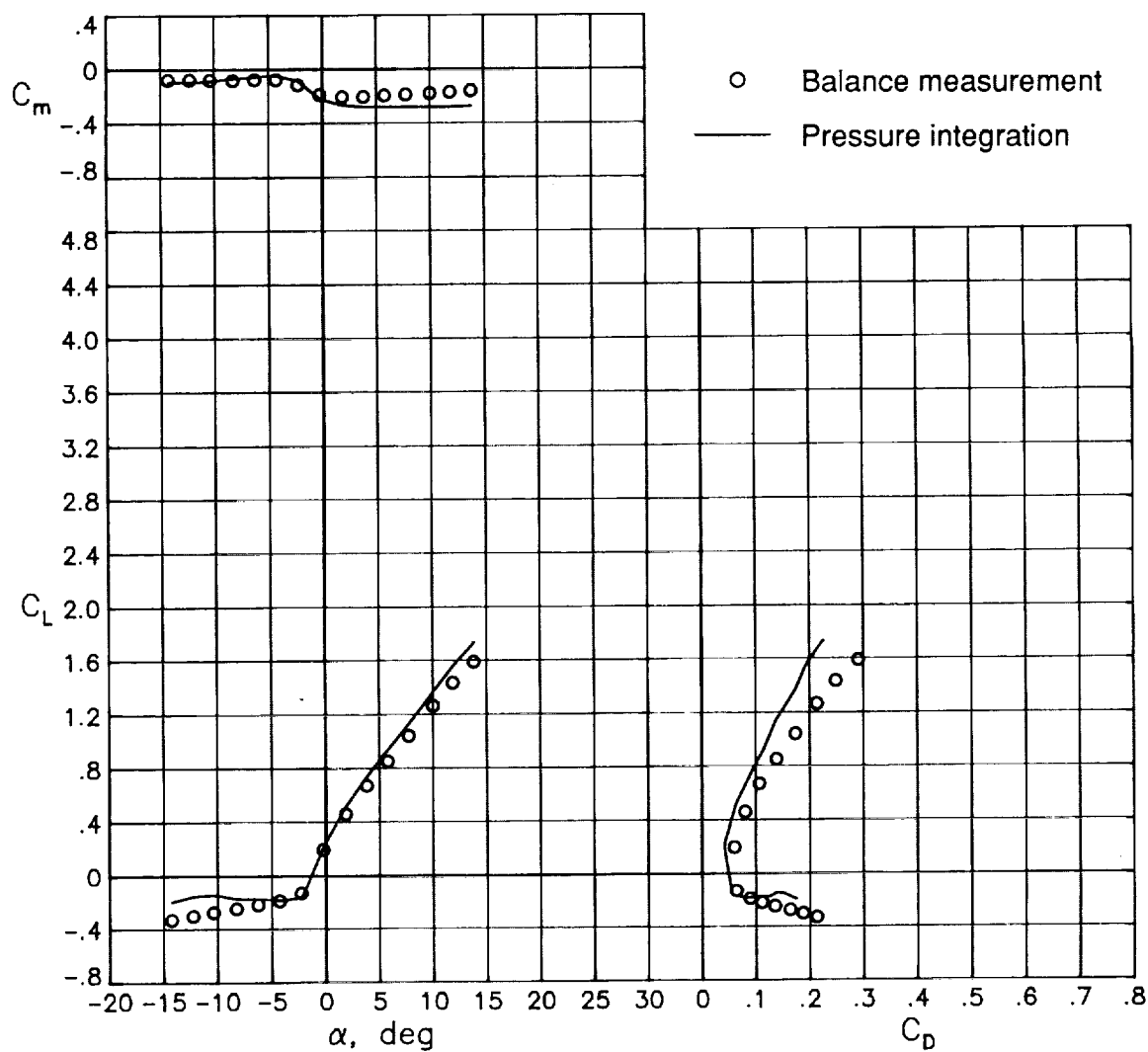
(c) $q_\infty = 30$ psf; $\delta_{LE} = -55°$; $\delta_{TE} = 15°$.

Figure A4. Continued.
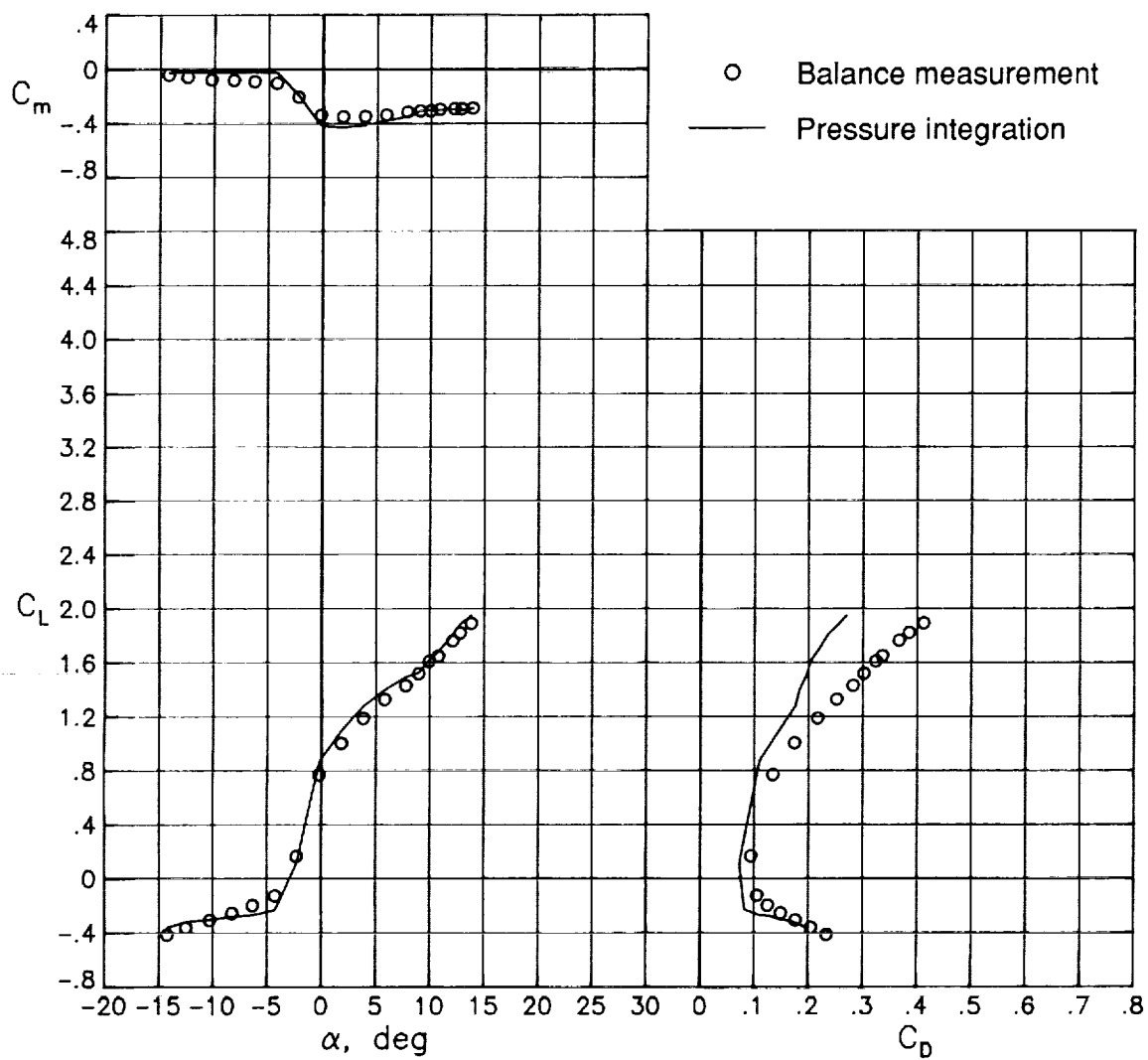
(d) $q_\infty = 30$ psf; $\delta_{LE} = -55°$; $\delta_{TE} = 30°$.

Figure A4. Continued.
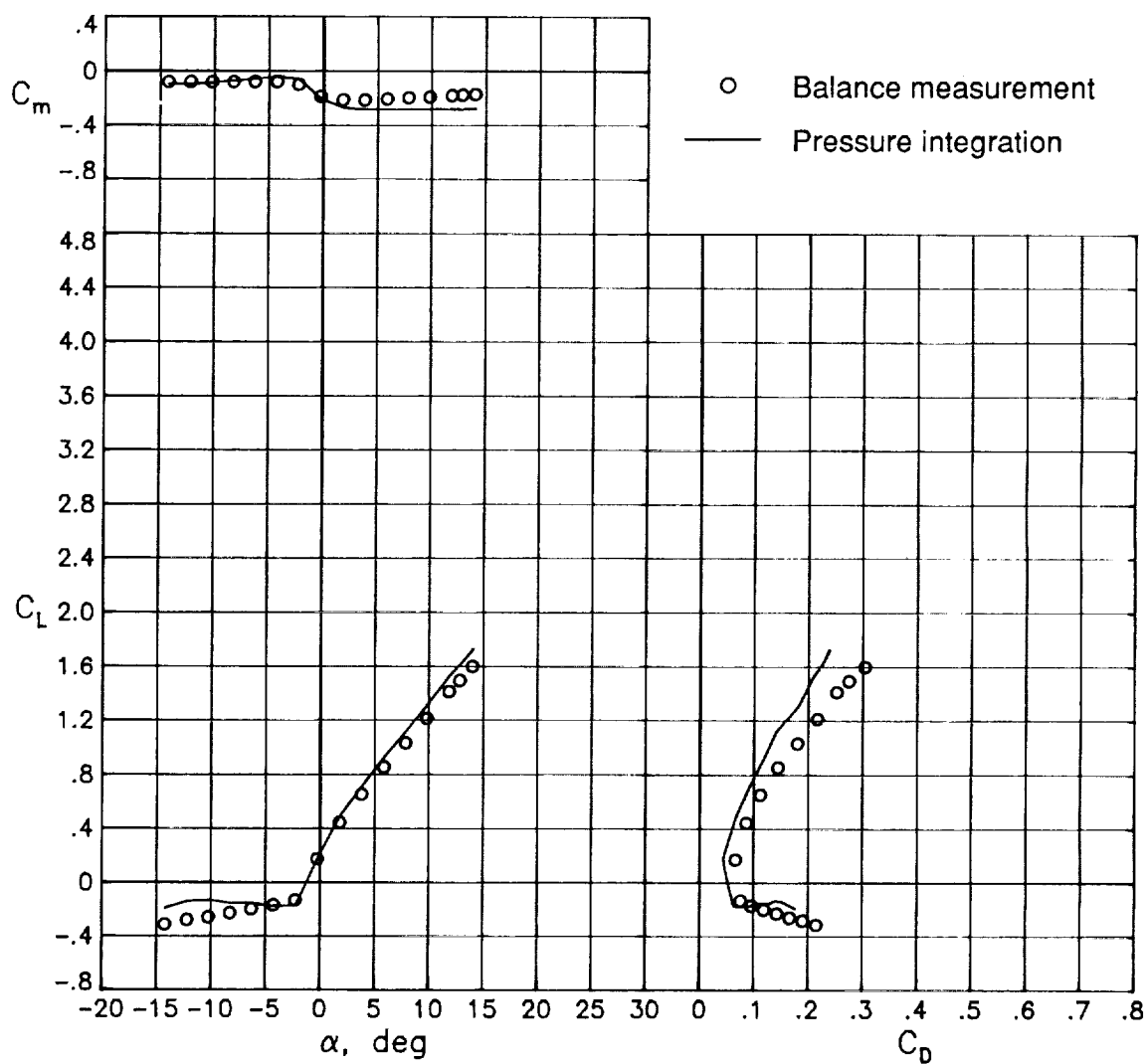
(e) $q_\infty = 30$ psf; $\delta_{LE} = -60°$; $\delta_{TE} = 15°$.

Figure A4. Continued.
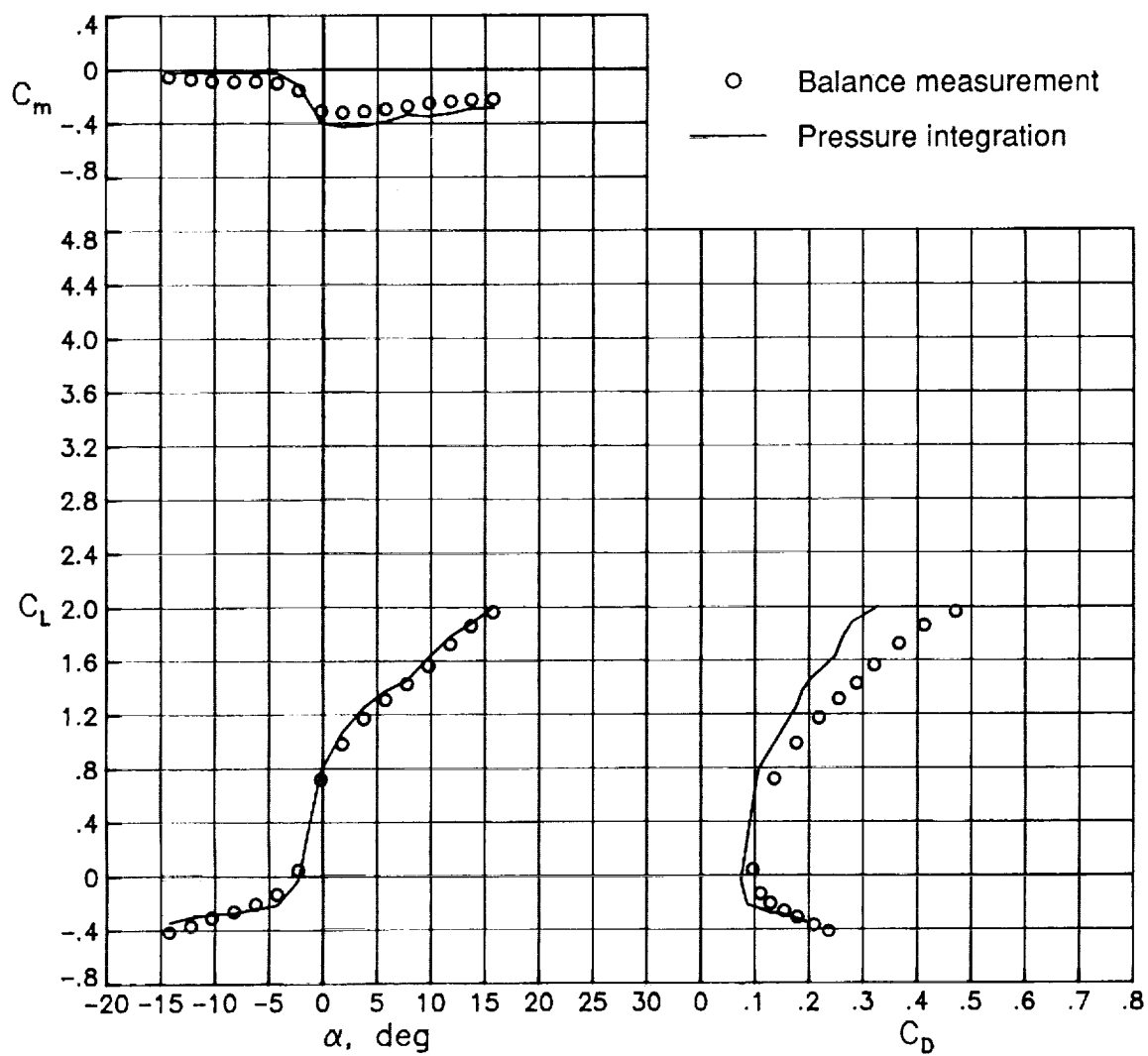
(f) $q_\infty = 30$ psf; $\delta_{LE} = -60°$; $\delta_{TE} = 30°$.

Figure A4. Concluded.
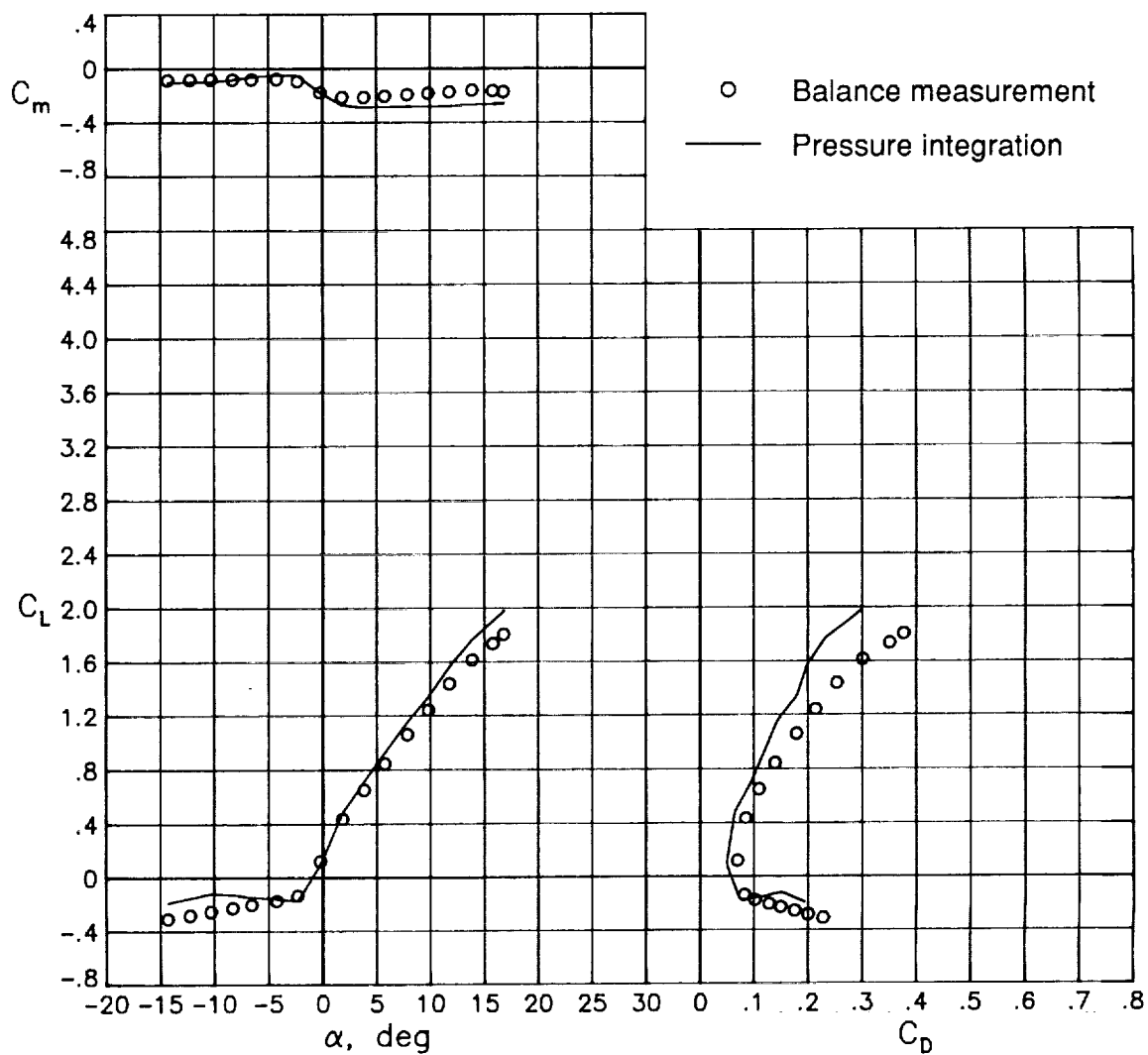
(a) $\delta_{LE} = -50°$; $\delta_{TE} = 15°$.

Figure A5. Longitudinal aerodynamic coefficients determined from balance measurements and pressure distribution integration for 12-percent leading-edge flap configuration. $q_\infty = 30$ psf.
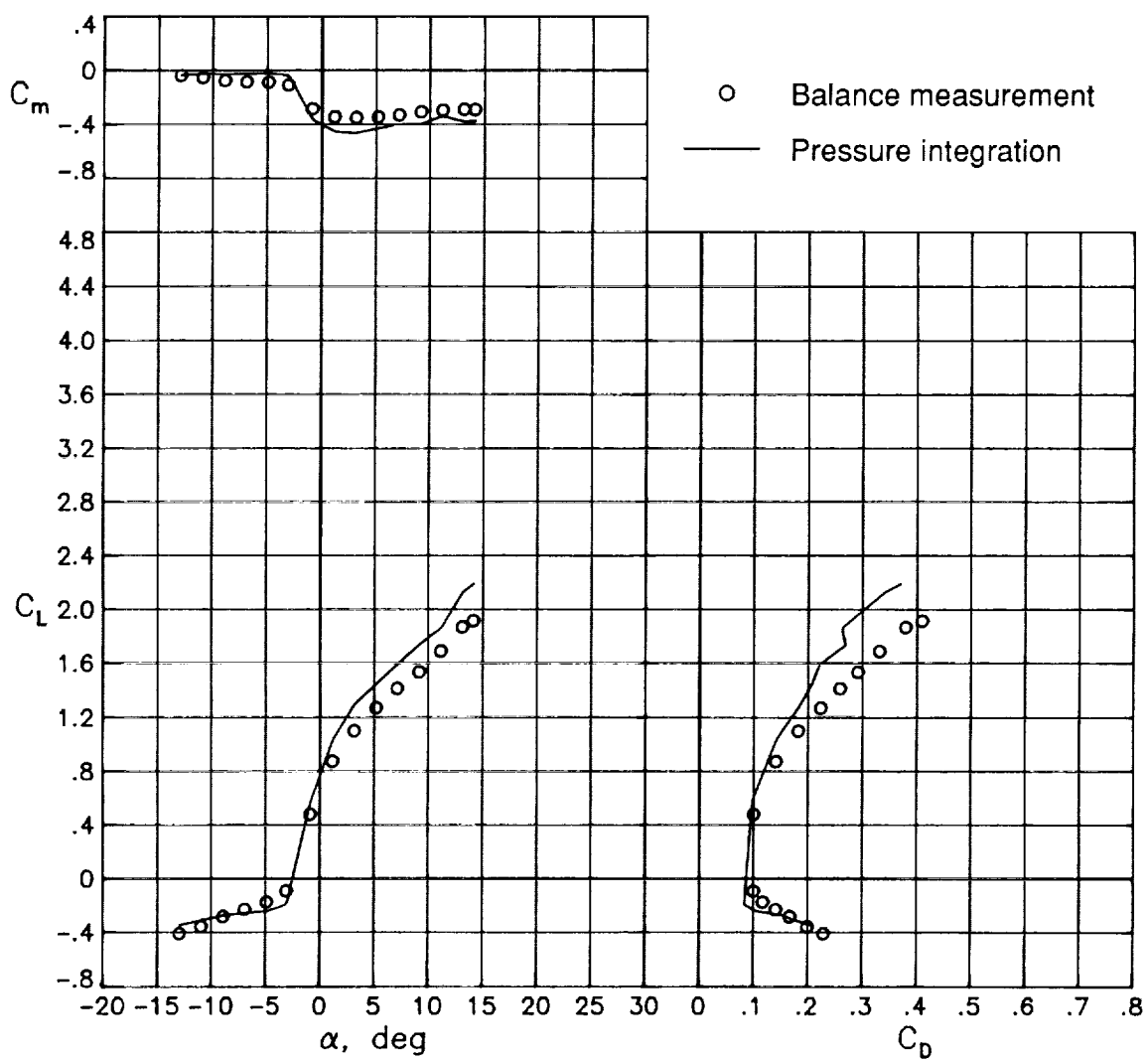
(b) $\delta_{LE} = -50°$; $\delta_{TE} = 30°$.

Figure A5. Continued.
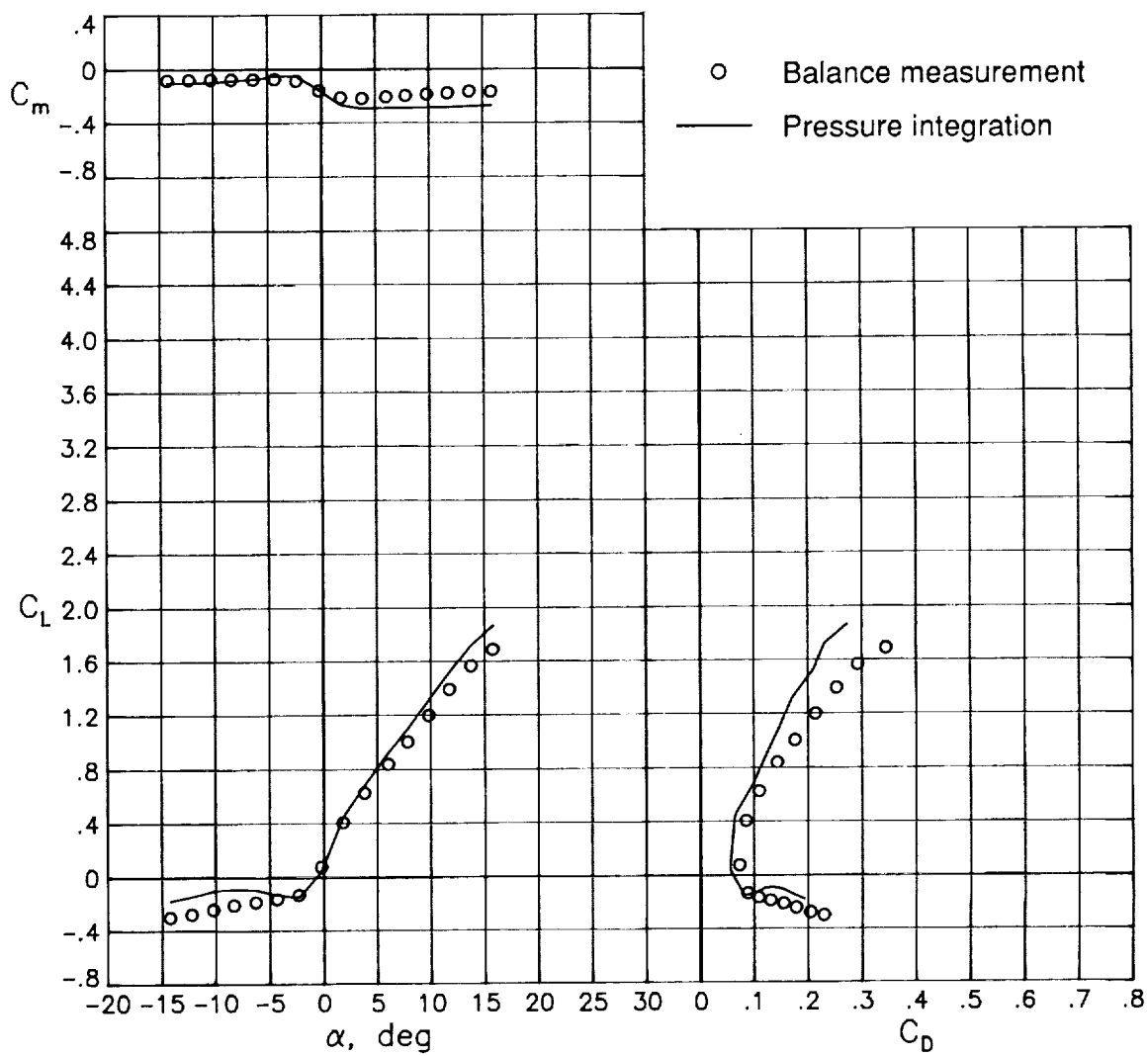
(c) $\delta_{LE} = -55°$; $\delta_{TE} = 15°$.

Figure A5. Continued.
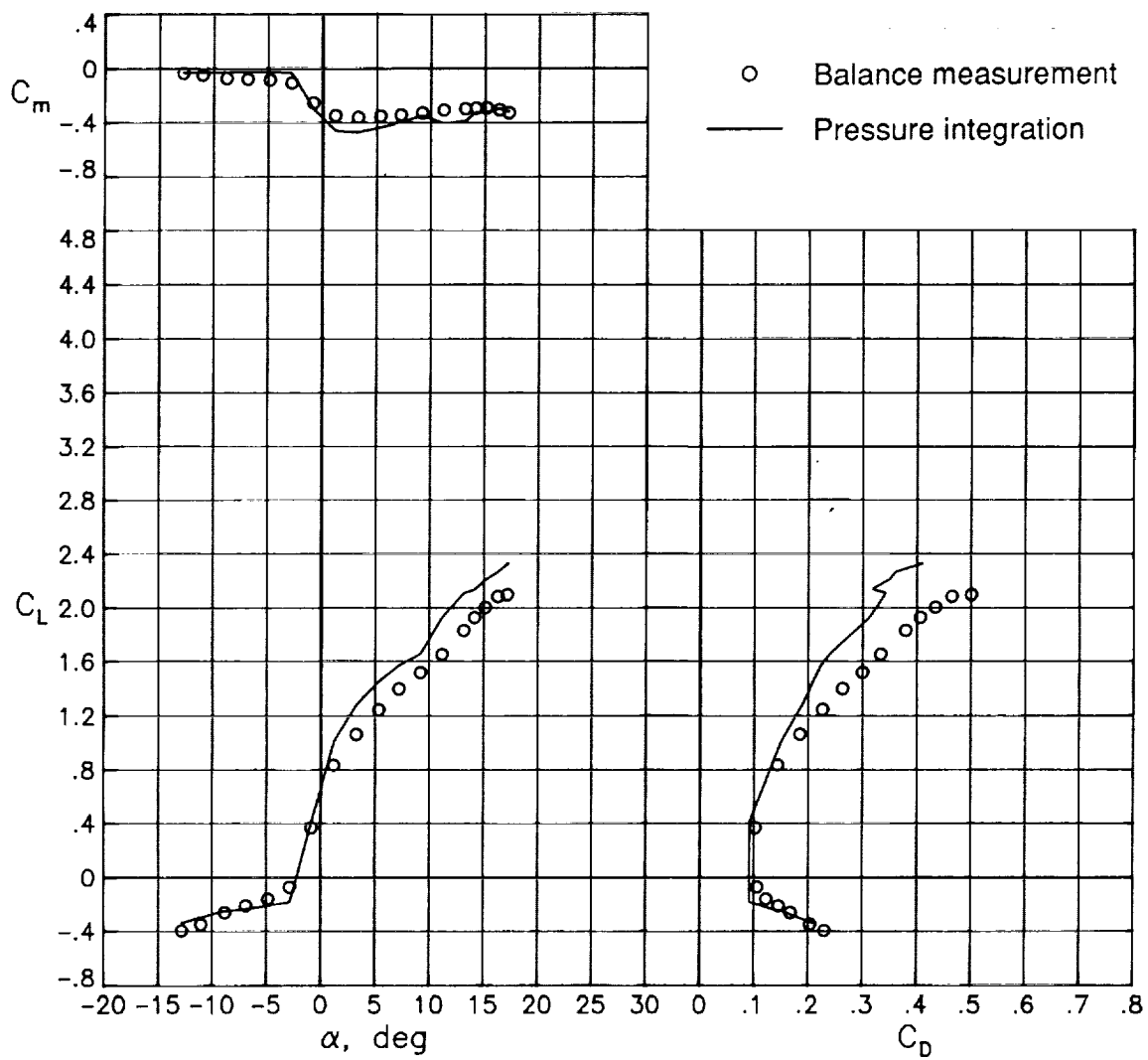
(d) $\delta_{LE} = -55°$; $\delta_{TE} = 30°$.

Figure A5. Concluded.

References

1. Stevens, W. A.; Goradia, S. H.; and Braden, J. A.: *Mathematical Model for Two-Dimensional Multi-Component Airfoils in Viscous Flow.* NASA CR-1843, 1971.

2. Brune, G. W.; and Manke, J. W.: *An Improved Version of the NASA-Lockheed Multielement Airfoil Analysis Computer Program.* NASA CR-145323, 1978.

3. Maskew, B.: *Program VSAERO—A Computer Program for Calculating the Non-Linear Aerodynamic Characteristics of Arbitrary Configurations, User's Manual.* NASA CR-166476, 1983.

4. Maskew, Brian: Prediction of Subsonic Aerodynamic Characteristics: A Case for Low-Order Panel Methods. *J. Aircr.*, vol. 19, no. 2, Feb. 1982, pp. 157–163.

5. Applin, Zachary T.: *Flow Improvements in the Circuit of the Langley 4- by 7-Meter Tunnel.* NASA TM-85662, 1983.

6. Pfenninger, W.; Reed, Helen L.; and Dagenhart, J. R.: Design Considerations of Advanced Supercritical Low Drag Suction Airfoils. *Viscous Flow Drag Reduction*, Gary R. Hough, ed., American Inst. of Aeronautics and Astronautics, c.1980, pp. 249–271.

7. Harvey, W. D.; and Pride, J. D.: The NASA Langley Laminar Flow Control Airfoil Experiment. AIAA-82-0567, Mar. 1982.

8. Allison, Dennis O.; and Dagenhart, J. Ray: *Two Experimental Supercritical Laminar-Flow-Control Swept-Wing Airfoils.* NASA TM-89073, 1987.

9. Morgan, Harry L., Jr.; and Paulson, John W., Jr.: *Low-Speed Aerodynamic Performance of a High-Aspect-Ratio Supercritical-Wing Transport Model Equipped With Full-Span Slat and Part-Span Double-Slotted Flaps.* NASA TP-1580, 1979.

10. Braslow, Albert L.; and Knox, Eugene C.: *Simplified Method for Determination of Critical Height of Distributed Roughness Particles for Boundary-Layer Transition at Mach Numbers From 0 to 5.* NACA TN 4363, 1958.

11. Weston, Robert Paul: Refinement of a Method for Determining the Induced and Profile Drag of a Finite Wing From Detailed Wake Measurements. Ph.D. Diss., Univ. of Florida, 1981.

12. Herriot, John G.: *Blockage Corrections for Three-Dimensional-Flow Closed-Throat Wind Tunnels, With Consideration of the Effect of Compressibility.* NACA Rep. 995, 1950. (Supersedes NACA RM A7B28.)

13. Polhamus, Edward C.: *Jet-Boundary-Induced-Upwash Velocities for Swept Reflection-Plane Models Mounted Vertically in 7- by 10-Foot, Closed, Rectangular Wind Tunnels.* NACA TN 1752, 1948.

14. Heyson, Harry H.: *Rapid Estimation of Wind-Tunnel Corrections With Application to Wind-Tunnel and Model Design.* NASA TN D-6416, 1971.

15. Applin, Zachary T.: Status of NASA Advanced LFC Airfoil High-Lift Study. *Laminar Flow Control—1981 Research and Technology Studies*, NASA CP-2218, 1982, pp. 43–61.

16. Scheib, James Scott; and Sandlin, Doral R.: *The Use of a Panel Code on High Lift Configurations of a Swept Forward Wing.* NASA CR-176968, 1986.

Table I. Pressure Tap Locations for Cruise Configuration

Upper surface		Lower surface	
x, in.	z, in.	x, in.	z, in.
0.0724	0.2047	0	0
.2079	.3622	.3835	−.2283
.4298	.5079	.7838	−.2953
.7920	.6654	1.1732	−.3543
1.1890	.7913	1.7644	−.4449
1.7865	.9409	2.5509	−.5669
2.3639	1.0630	3.3394	−.6850
3.1544	1.2008	4.3161	−.8346
3.9450	1.3189	5.3051	−.9803
4.7277	1.4213	6.4898	−1.2953
5.5042	1.5079	7.6650	−1.8228
6.4978	1.6102	8.8491	−2.2756
7.4852	1.7008	10.0387	−2.5236
8.4663	1.7756	11.8055	−2.7559
9.8411	1.8661	13.7753	−2.9055
11.8143	1.9724	17.7192	−2.9724
13.7797	2.0512	21.6548	−2.7677
17.7183	2.1339	25.6013	−2.2283
21.6521	2.1181	27.5584	−1.7244
25.5970	2.0000	29.5269	−1.1299
27.5640	1.8937	31.4947	−.5354
29.5324	1.7402	33.0682	−.0551
31.5072	1.5276	34.6318	.1693
33.2883	1.2559	36.2100	.2244
35.0473	.9291	37.3927	.1969
36.6332	.6181	38.5836	.0945
37.7970	.3701	39.3624	.0236
38.5954	.2008		

Table II. Pressure Tap Locations for High-Lift Configuration

Upper surface		Lower surface	
x, in.	z, in.	x, in.	z, in.
0.0724	0.2047	0	0
.2079	.3622	.3835	−.2283
.4298	.5079	.7838	−.2953
.7920	.6654	1.1732	−.3543
1.1890	.7913	1.7644	−.4449
1.7865	.9409	2.5509	−.5669
2.3639	1.0630	3.3394	−.6850
3.1544	1.2008	4.3161	−.8346
3.9450	1.3189	5.3051	−.9803
4.7277	1.4213	6.4898	−1.2953
5.5042	1.5079	7.6650	−1.8228
6.4978	1.6102	8.8491	−2.2756
7.4852	1.7008	10.0387	−2.5236
8.4663	1.7756	11.8055	−2.7559
9.8411	1.8661	13.7753	−2.9055
11.8143	1.9724	17.7192	−2.9724
13.7797	2.0512	21.6548	−2.7677
17.7183	2.1339	25.6013	−2.2283
21.6521	2.1181	27.5584	−1.7244
25.5970	2.0000	29.4906	−1.1220
27.5640	1.8937	30.6853	−.6575
29.5324	1.7402	31.6770	−.0315
31.4924	1.5472	32.4759	.5079
32.4702	1.4094	33.0524	.8425
33.2612	1.2795	33.6629	1.0433
34.0315	1.1417	34.2513	1.1024

Table III. Pressure Tap Locations for Trailing-Edge Flap

Upper surface		Lower surface	
x, in.	z, in.	x, in.	z, in.
0.1978	0.4961	0	0
.5840	.8386	.2033	−.4291
1.1710	1.1024	.5807	−.6732
2.3478	1.2677	1.1691	−.7559
3.5381	1.2480	1.7593	−.5984
5.1094	1.0079	2.3631	−.4173
6.6937	.7008	3.5337	−.0591
8.2727	.3661	5.1106	.1693
		6.6900	.2240
		7.8735	.1969
		9.0439	.0984
		9.8379	0

Table IV. Pressure Tap Location for Leading-Edge Flaps

Upper surface		Lower surface	
x, in.	z, in.	x, in.	z, in.
(a) 10-percent leading-edge flap			
0.1035	0.2874	0	0
.2969	.5118	.1040	−.2441
.5365	.6654	.2973	−.4094
.7872	.7756	.5743	−.4921
1.1845	.8583	.8860	−.4922
1.7797	.8346	1.1696	−.4055
2.3661	.6968	1.5777	−.2205
2.9495	.4882	1.9658	−.0157
3.5506	.2126	2.4654	.1457
		2.9431	.1890
		3.4362	.1378
		3.9335	0
(b) 12-percent leading-edge flap			
0.1060	0.2677	0	0
.3077	.4764	.0894	−.2165
.5512	.6181	.2911	−.3701
.7785	.7323	.5856	−.4724
1.1877	.8346	.8737	−.5079
1.7703	.8661	1.1635	−.4764
2.3624	.8031	1.5679	−.3543
2.9436	.6654	1.9634	−.1890
3.5344	.4882	2.4598	.0157
4.1245	.2667	2.9533	.1457
		3.4378	.1850
		3.9350	.1654
		4.4206	.0787
		4.7246	0

Table V. Spanwise Location of Flap Bracket Centerlines

Bracket	y, in.	y/b
1	5.125	0.043
2	34.245	.290
3	44.495	.377
4	73.615	.623
5	83.865	.710
6	112.985	.957

Table VI. Balance Load Characteristics and Effect on Accuracy
of Aerodynamic Coefficients

Component	Maximum load	Accuracy
Normal force, lb	7 500	±37.5
Axial force, lb	3 500	±24.5
Pitching moment, in-lb	90 000	±450
Rolling moment, in-lb	24 000	±120
Yawing moment, in-lb	12 000	±90
Side force, lb	1 000	±5

Aerodynamic coefficient	Accuracy for—	
	$q_\infty = 15$ psf	$q_\infty = 30$ psf
Lift	±0.079	±0.039
Drag	±0.011	±0.005
Pitching moment	±0.288	±0.144
Rolling moment	±0.026	±0.013
Yawing moment	±0.020	±0.0098
Side force	±0.051	±0.026

Table VII. Number of Segments Used by MCARF To Represent
Airfoil Section

Configuration	Number of segments
Cruise: Main element	65
T.E. flap:	102 (total)
Main element	61
T.E. flap	41
L.E. flap:	143 (total)
Main element	61
L.E. flap	41
T.E. flap	41

Table VIII. Number of Panels Used by VSAERO To Represent Semispan Model

Configuration	Number of segments
Cruise:	285 (total)
Wing:	
Chordwise panels	30
Spanwise panels	8
Total	240
Wing tip:	
Chordwise panels	3
Spanwise panels	15
Total	45
T.E. flap:	475 (total)
Wing:	
Chordwise panels	30
Spanwise panels	8
Total	240
Wing tip:	
Chordwise panels	3
Spanwise panels	15
Total	45
T.E. flap:	
Chordwise panels	20
Spanwise panels	8
Total	160
T.E. flap tip:	
Chordwise panels	3
Spanwise panels	10
Total	30
L.E. flap:	665 (total)
Wing:	
Chordwise panels	30
Spanwise panels	8
Total	240
Wing tip:	
Chordwise panels	3
Spanwise panels	15
Total	45
L.E. flap:	
Chordwise panels	20
Spanwise panels	8
Total	160
L.E. flap tip:	
Chordwise panels	3
Spanwise panels	10
Total	30
T.E. flap:	
Chordwise panels	20
Spanwise panels	8
Total	160
T.E. flap tip:	
Chordwise panels	3
Spanwise panels	10
Total	30
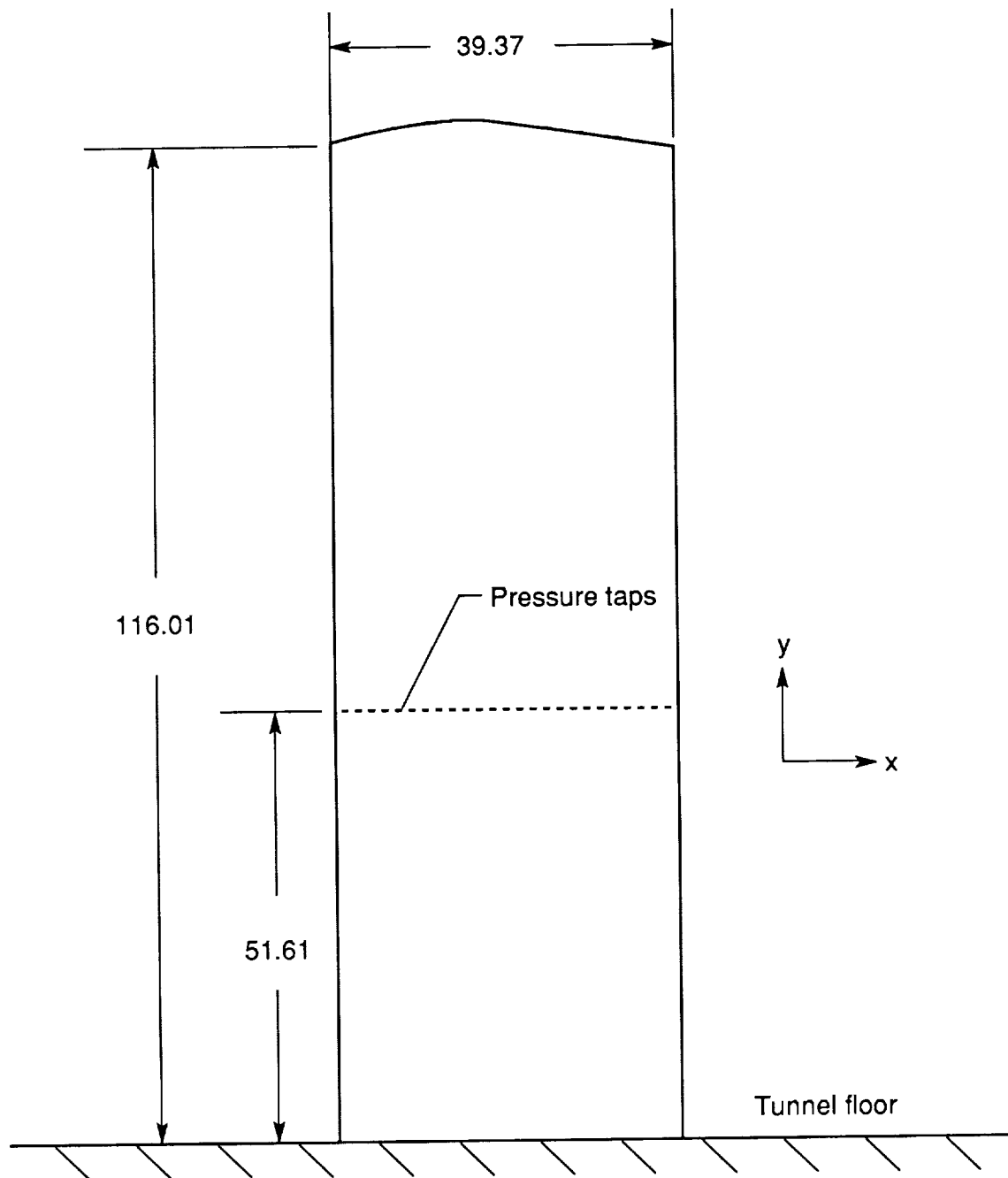
(a) Sketch of cruise planform. Dimensions are in inches.

Figure 1. Semispan wing model installed in Langley 14- by 22-Foot Subsonic Tunnel.
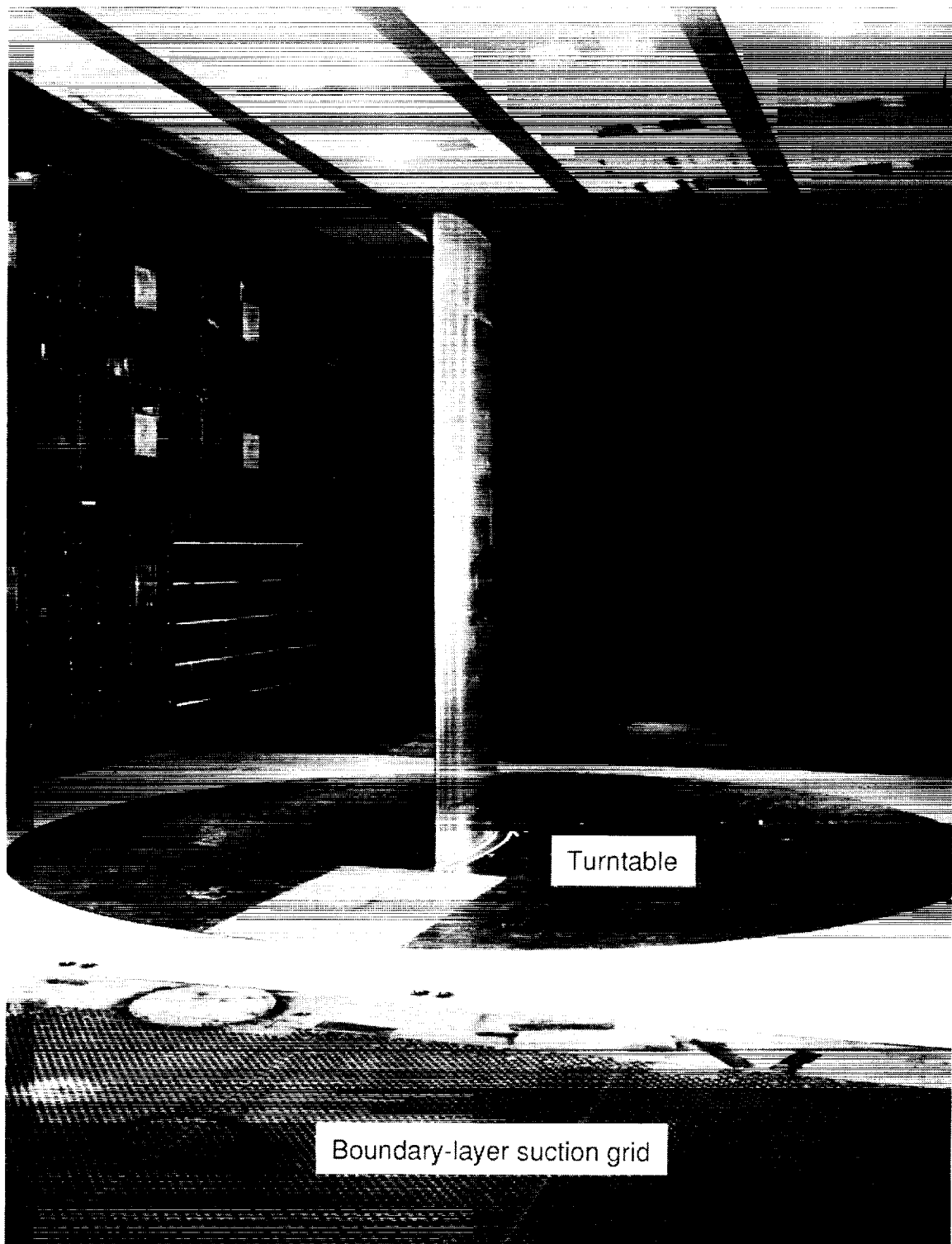
L-90-24

(b) Photograph of cruise configuration.

Figure 1. Continued.
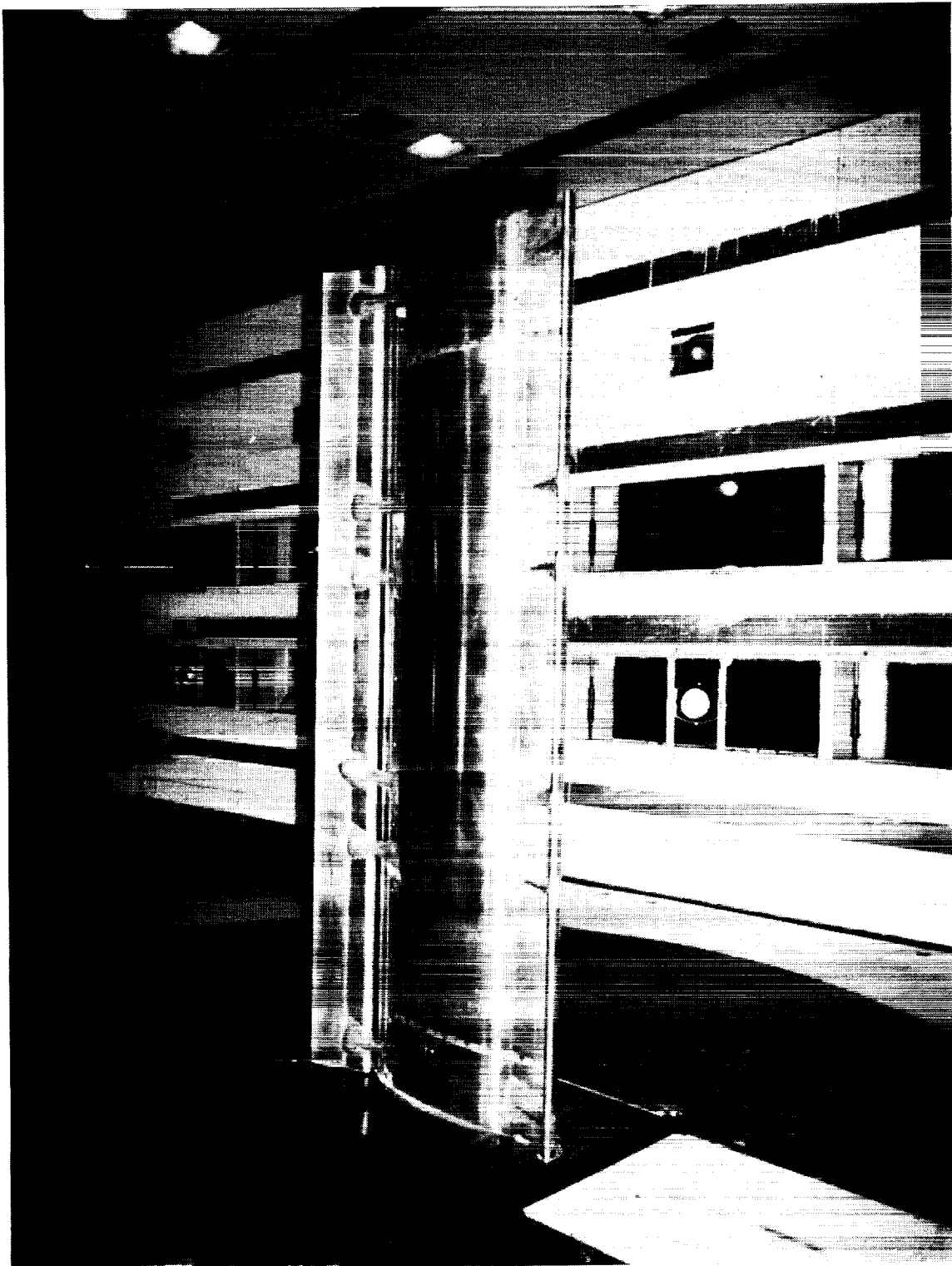
L-83-3130

(c) Photograph of high-lift configuration.

Figure 1. Concluded.
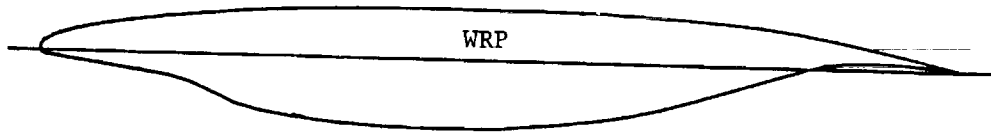
(a) Cruise configuration.

(b) Trailing-edge flap configuration.

(c) 10-percent leading-edge flap configuration.

(d) 12-percent leading-edge flap configuration.

Figure 2. Section contours of wing configurations tested.
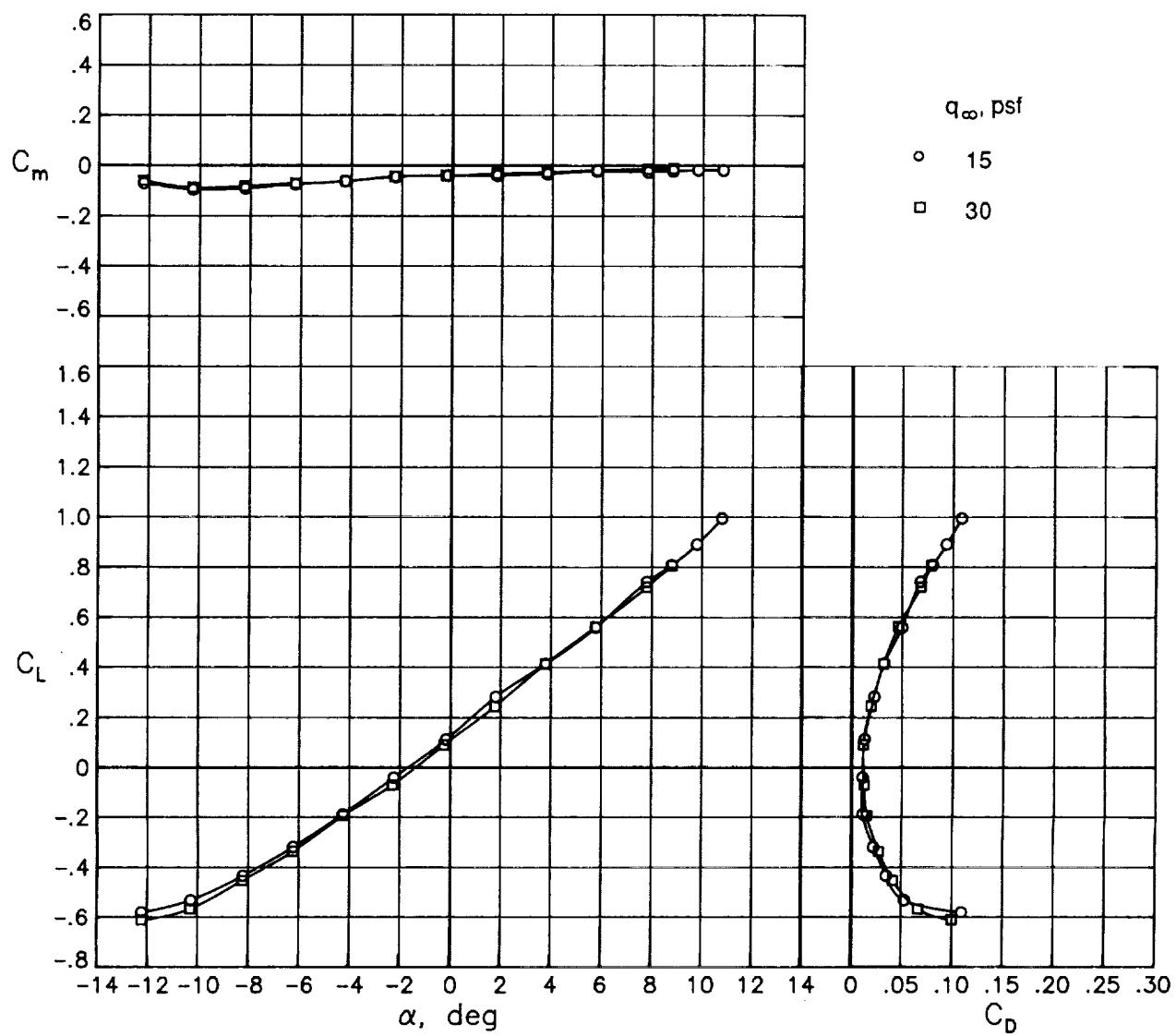
Figure 3. Longitudinal aerodynamic characteristics of cruise configuration.
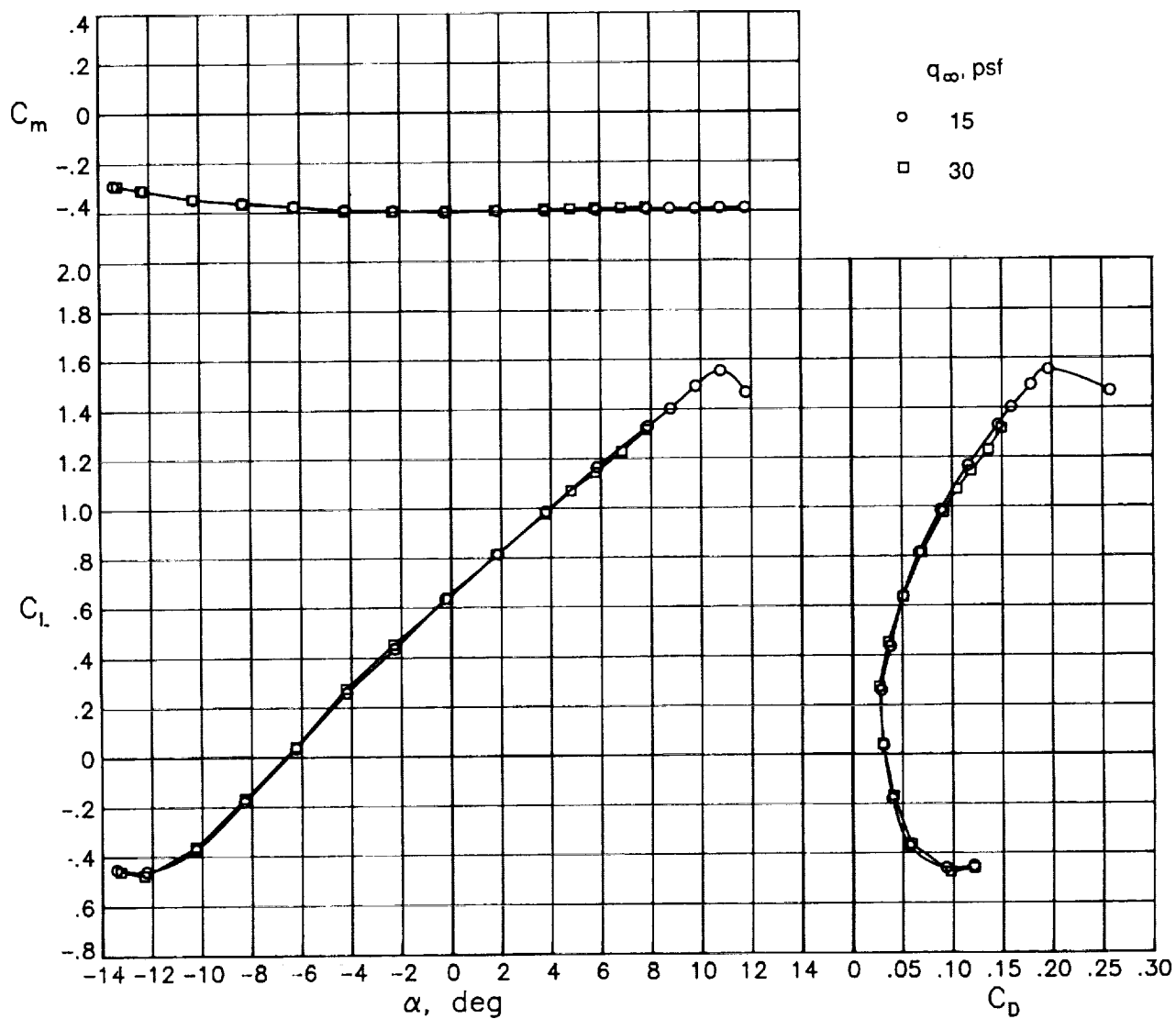
Figure 4. Longitudinal aerodynamic characteristics of trailing-edge flap configuration. $\delta_{TE} = 15°$.
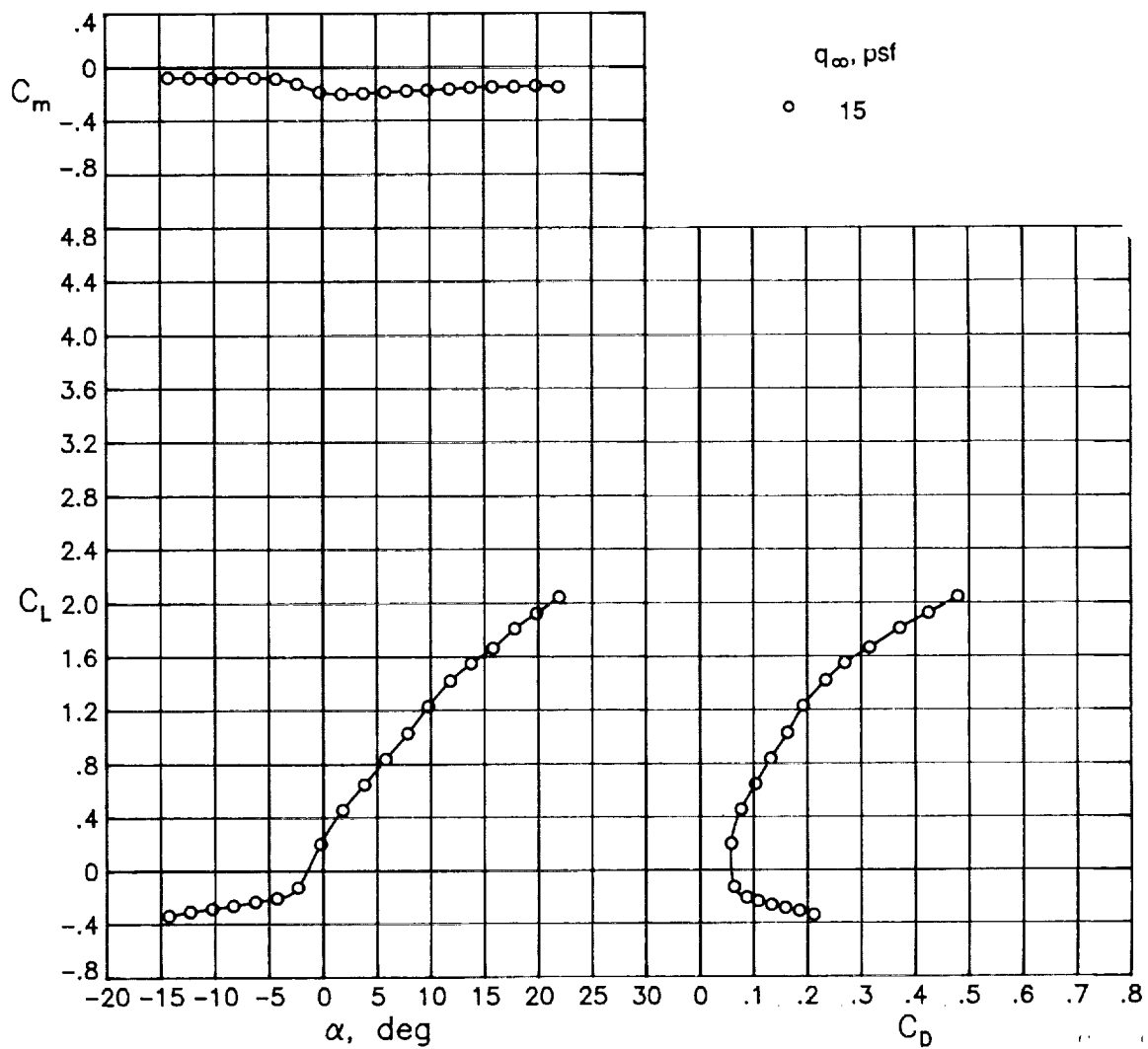
(a) $\delta_{LE} = -50°$; $\delta_{TE} = 15°$.

Figure 5. Longitudinal aerodynamic characteristics of 10-percent leading-edge flap configuration.
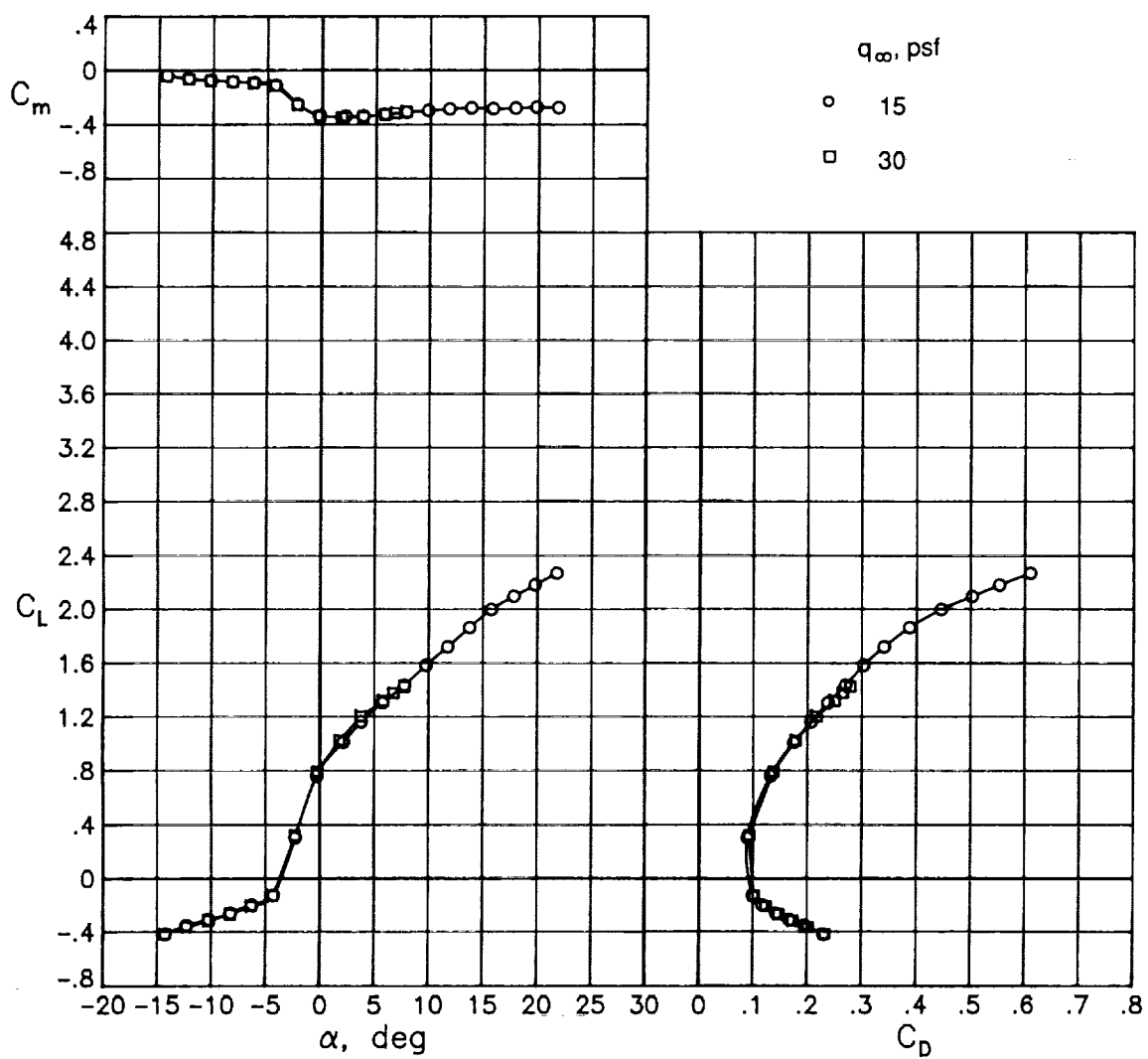
(b) $\delta_{LE} = -50°$; $\delta_{TE} = 30°$.

Figure 5. Continued.
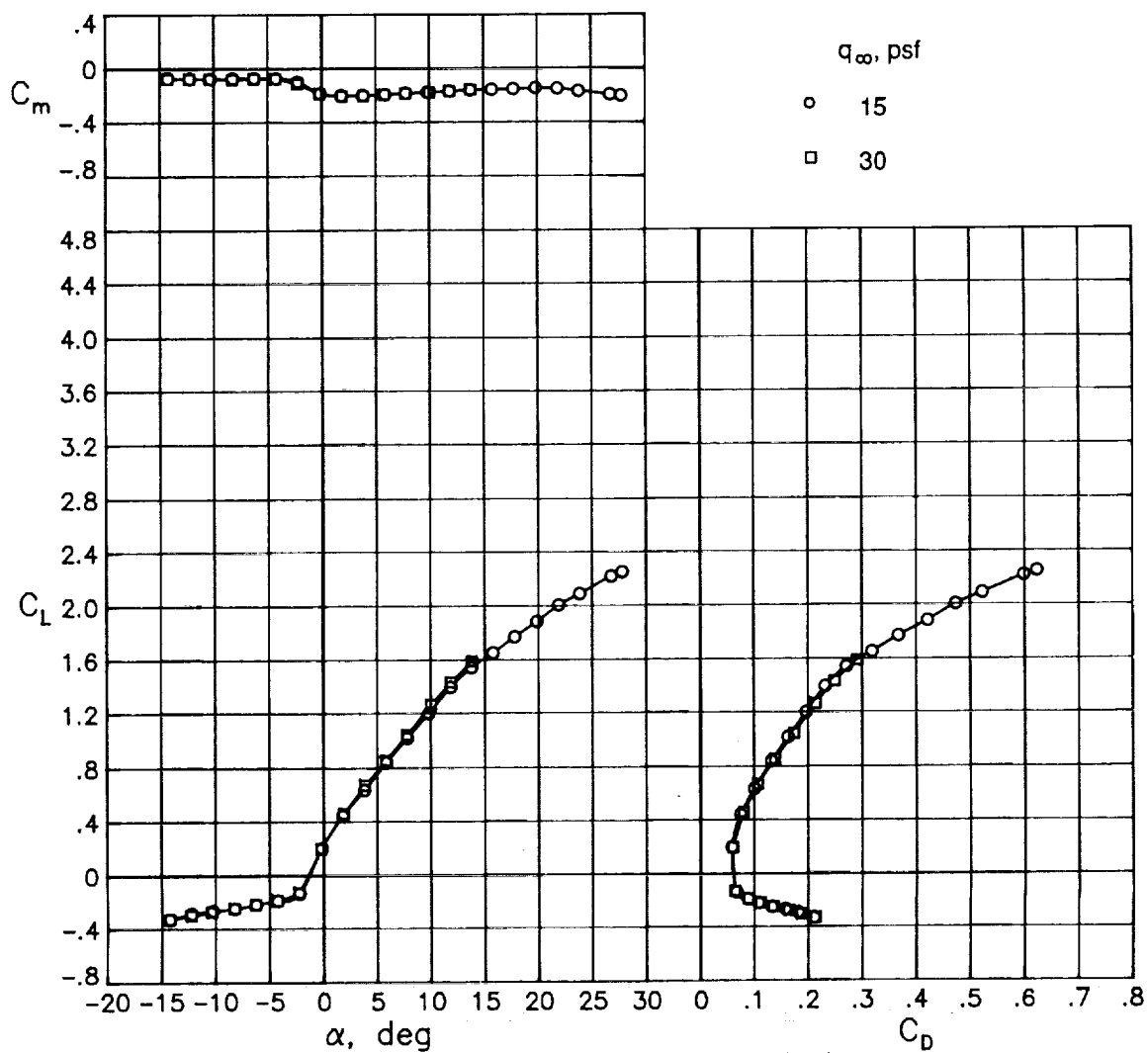
(c) $\delta_{LE} = -55°$; $\delta_{TE} = 15°$.

Figure 5. Continued.
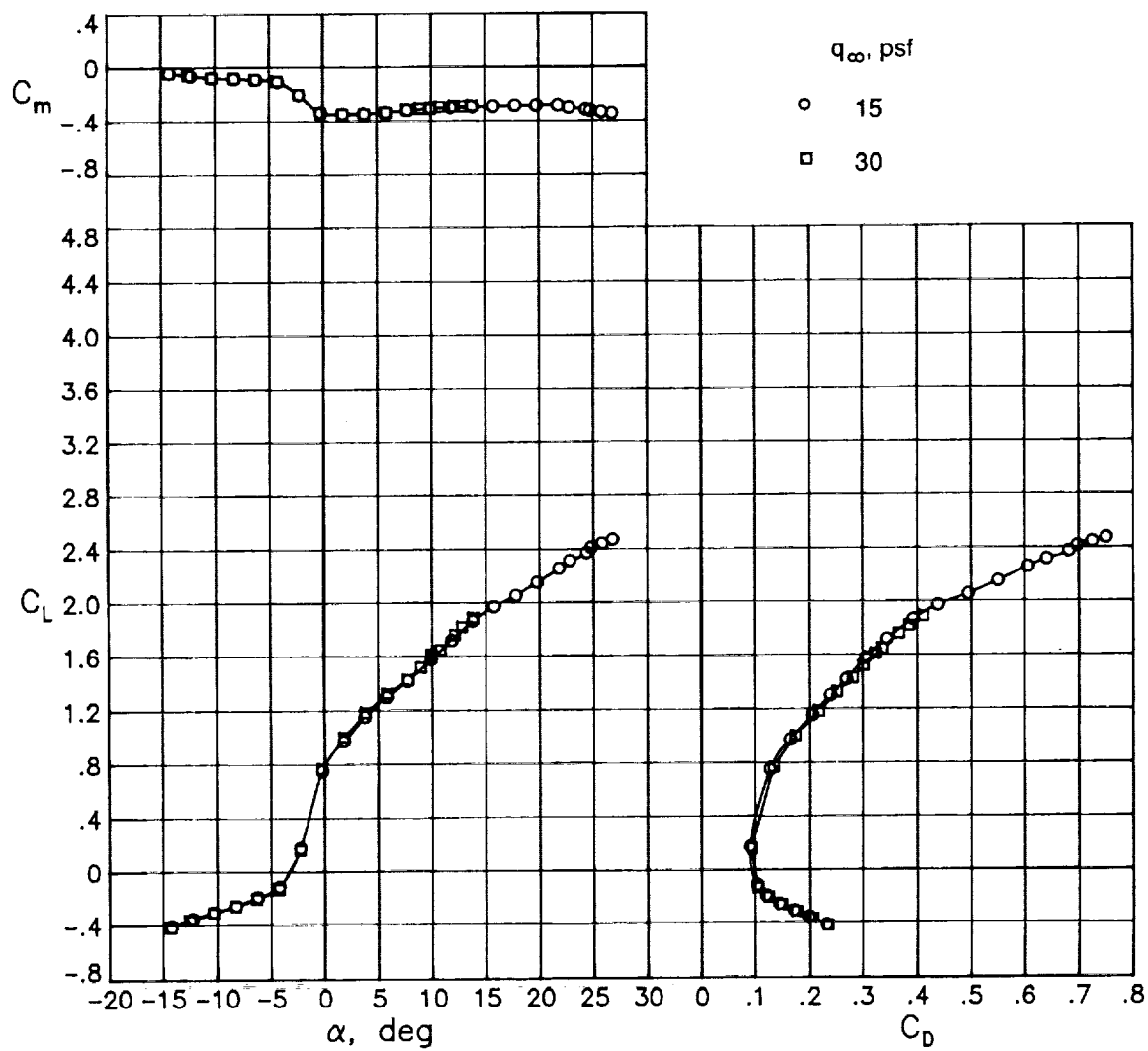
(d) $\delta_{LE} = -55°$; $\delta_{TE} = 30°$.

Figure 5. Continued.
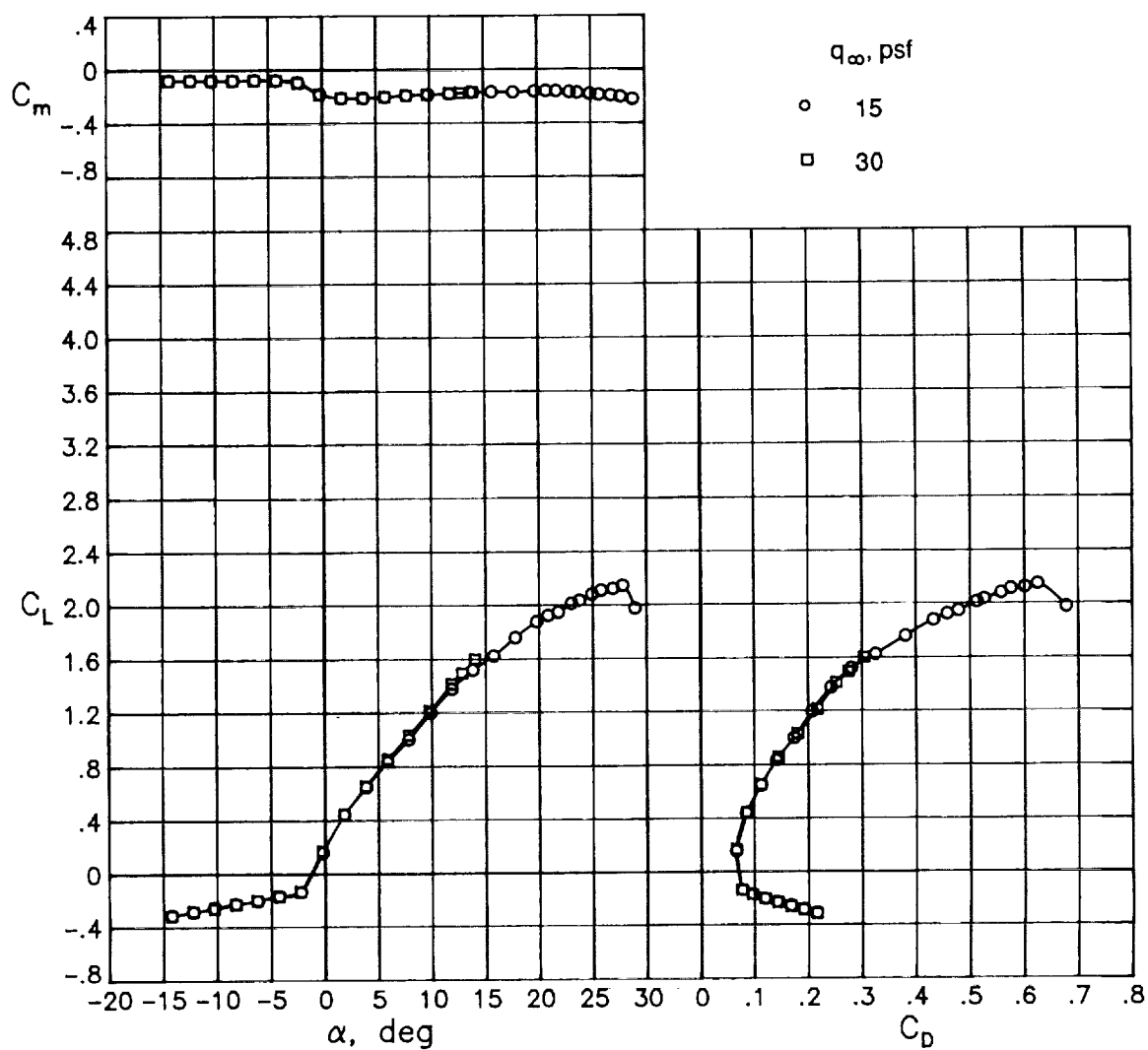
(e) $\delta_{LE} = -60°$; $\delta_{TE} = 15°$.

Figure 5. Continued.
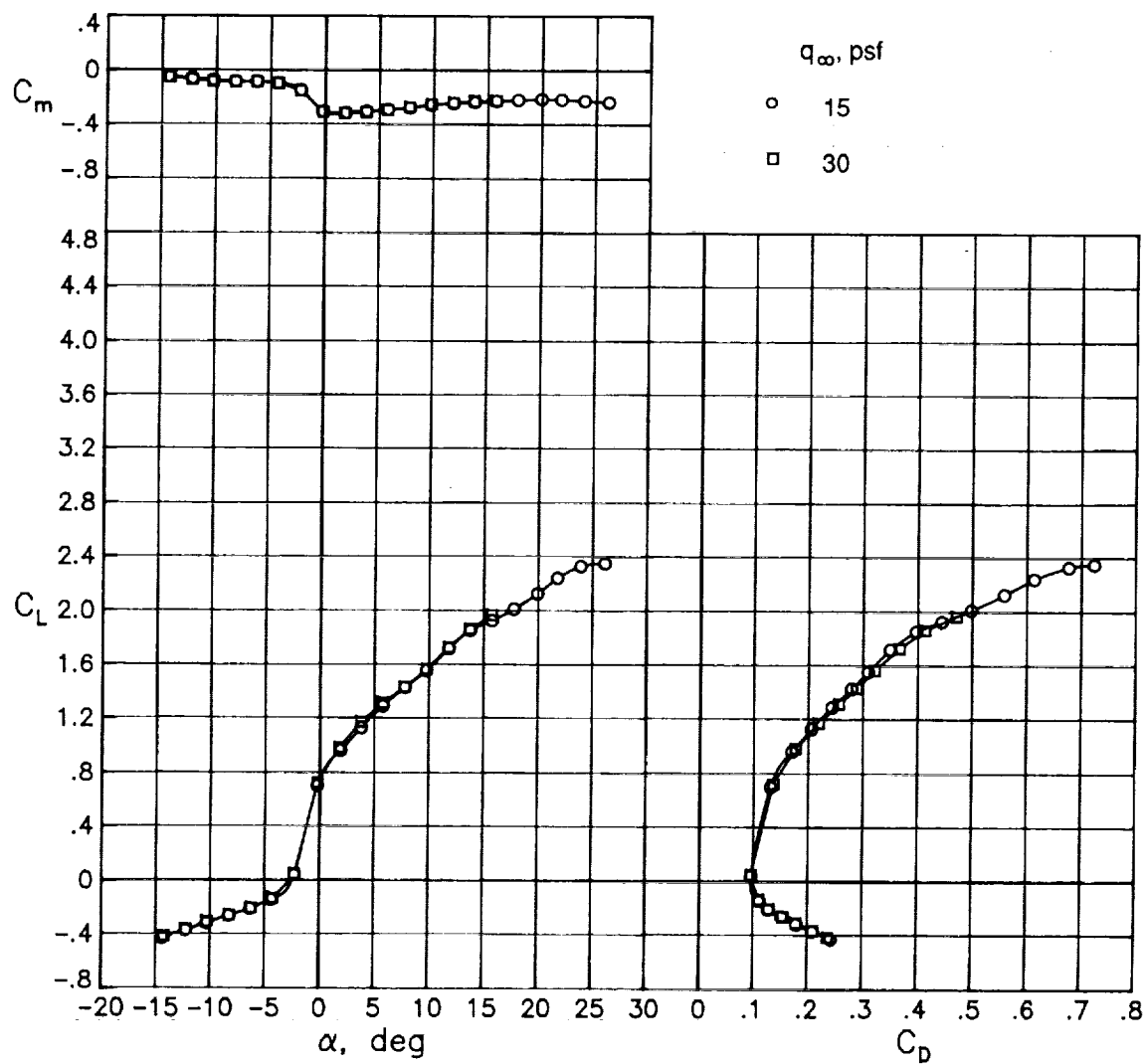
(f) $\delta_{LE} = -60°$; $\delta_{TE} = 30°$.

Figure 5. Concluded.
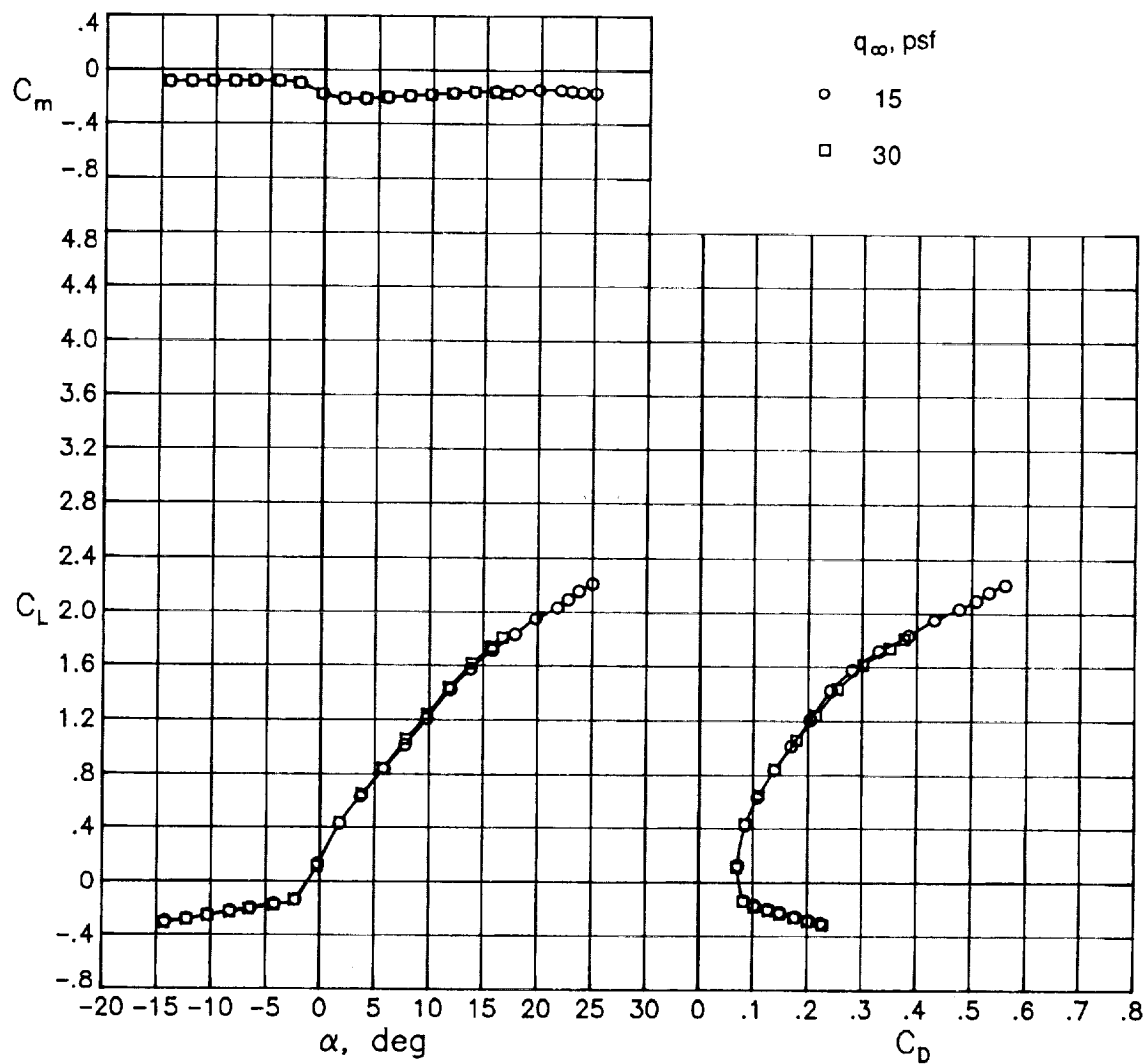
(a) $\delta_{LE} = -50°$; $\delta_{TE} = 15°$.

Figure 6. Longitudinal aerodynamic characteristics of 12-percent leading-edge flap configuration.
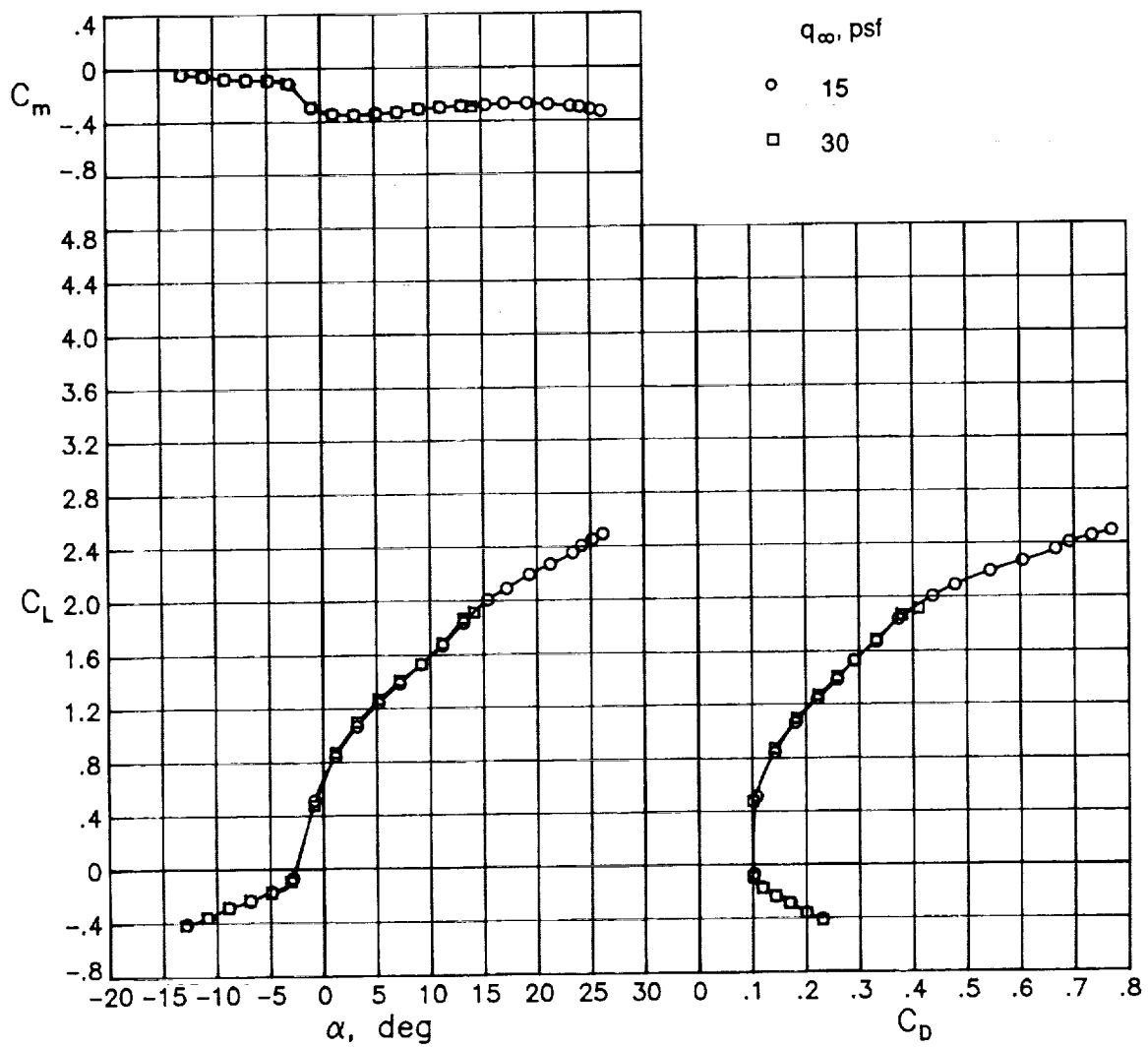
(b) $\delta_{LE} = -50°$; $\delta_{TE} = 30°$.

Figure 6. Continued.
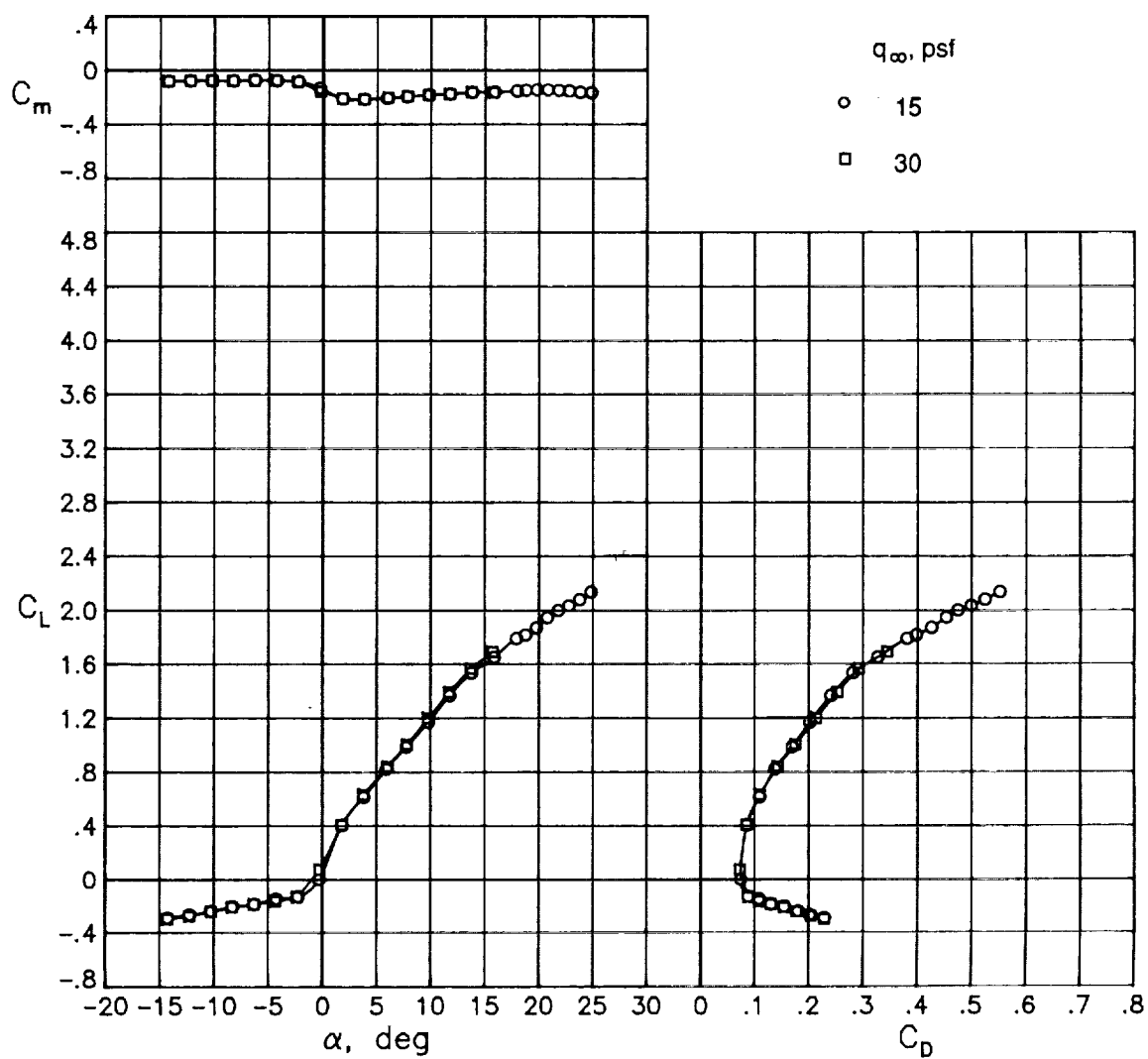
(c) $\delta_{LE} = -55°$; $\delta_{TE} = 15°$.

Figure 6. Continued.
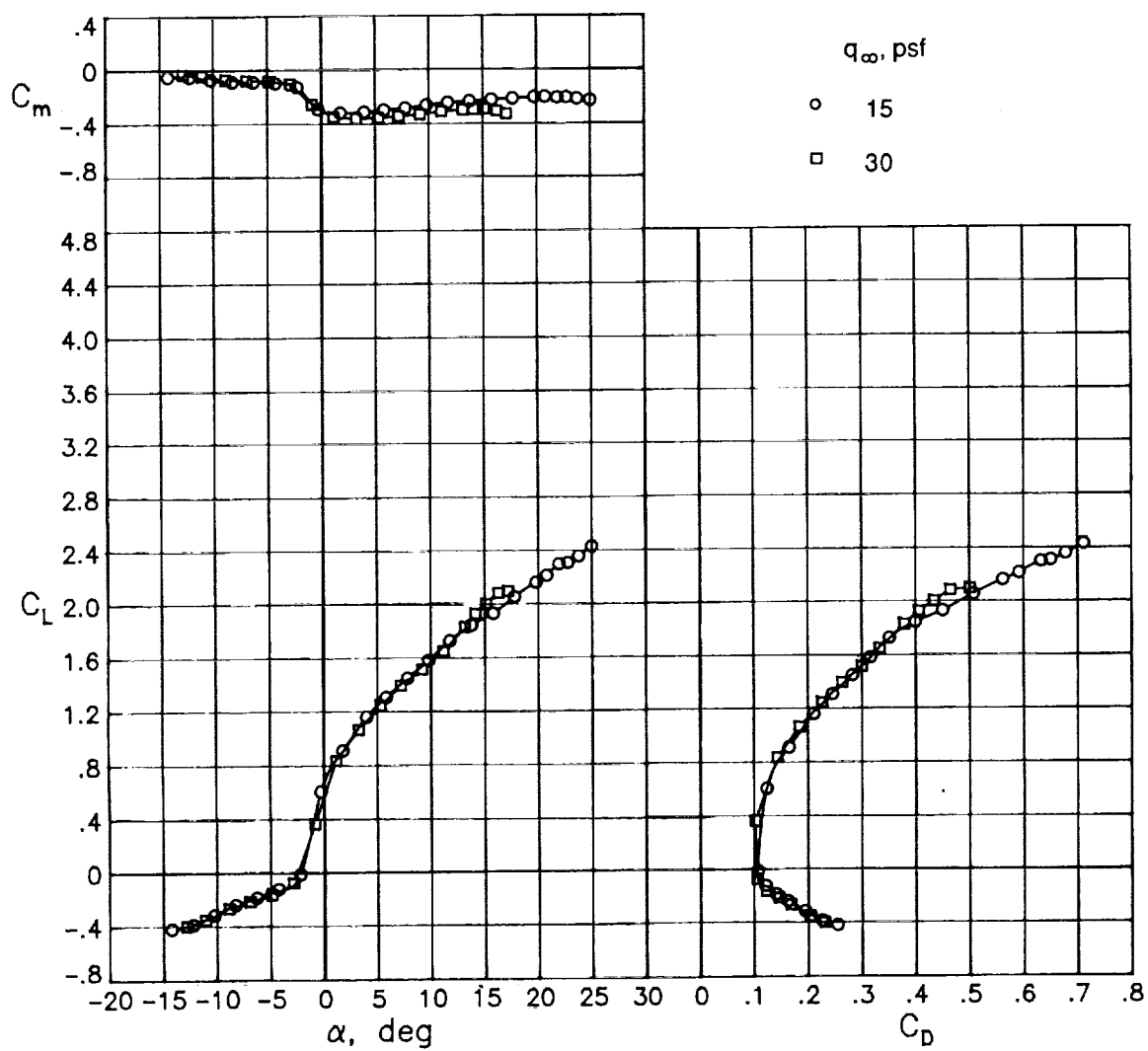
(d) $\delta_{LE} = -55°$; $\delta_{TE} = 30°$.

Figure 6. Concluded.
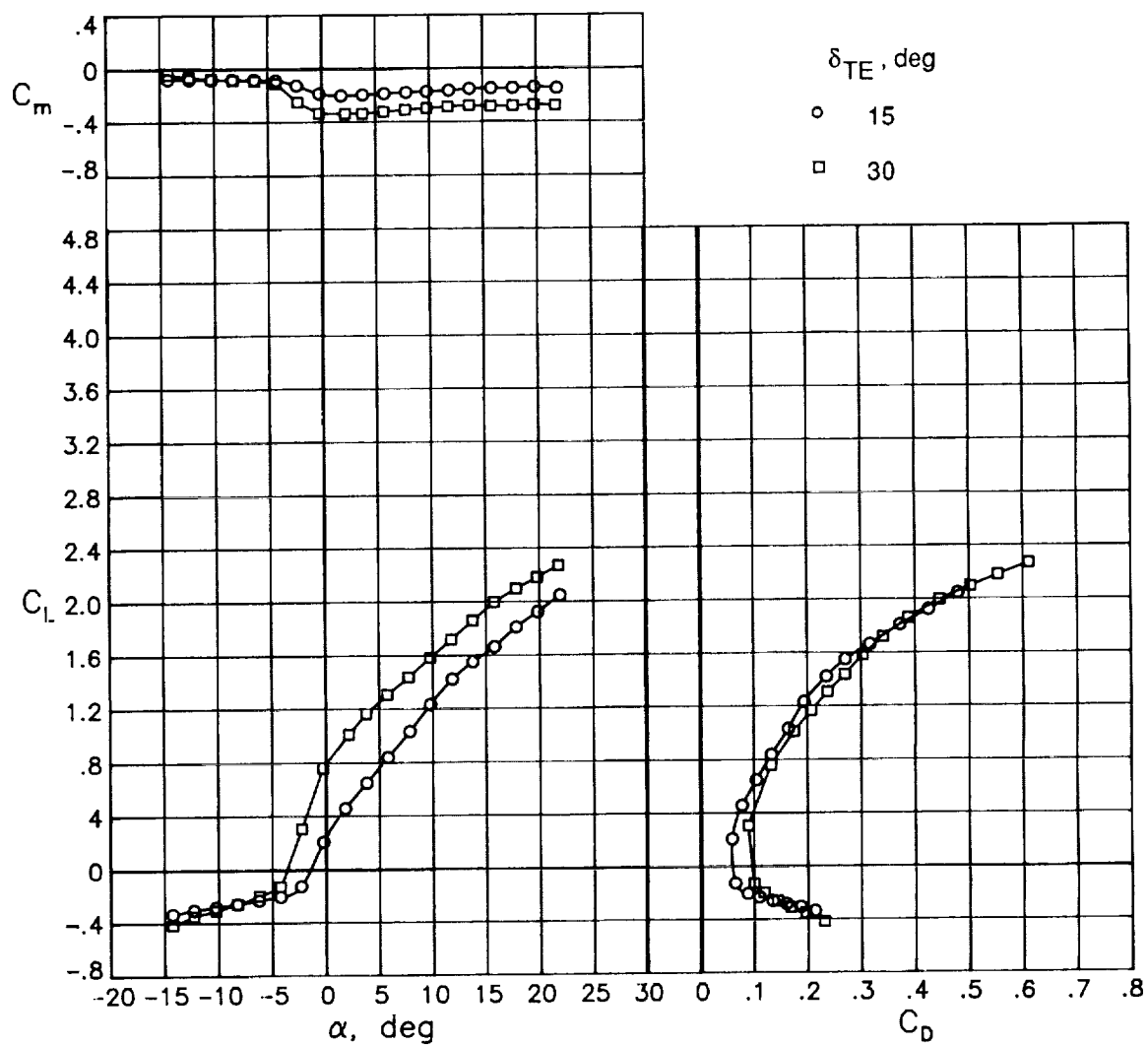
(a) $\delta_{LE} = -50°$; $q_\infty = 15$ psf.

Figure 7. Effect of trailing-edge flap deflection for 10-percent leading-edge flap configuration.
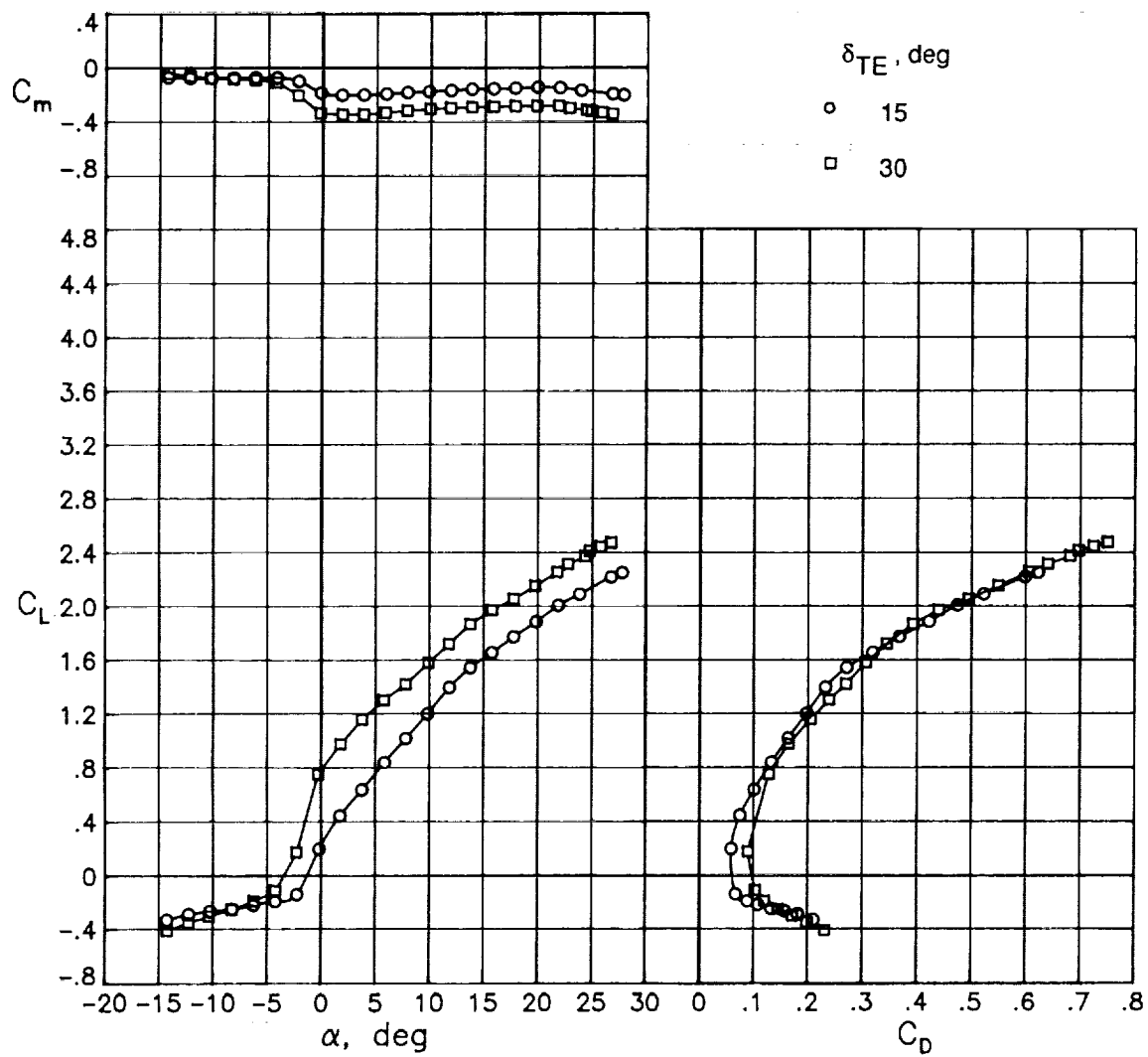
(b) $\delta_{LE} = -55°$; $q_\infty = 15$ psf.

Figure 7. Continued.
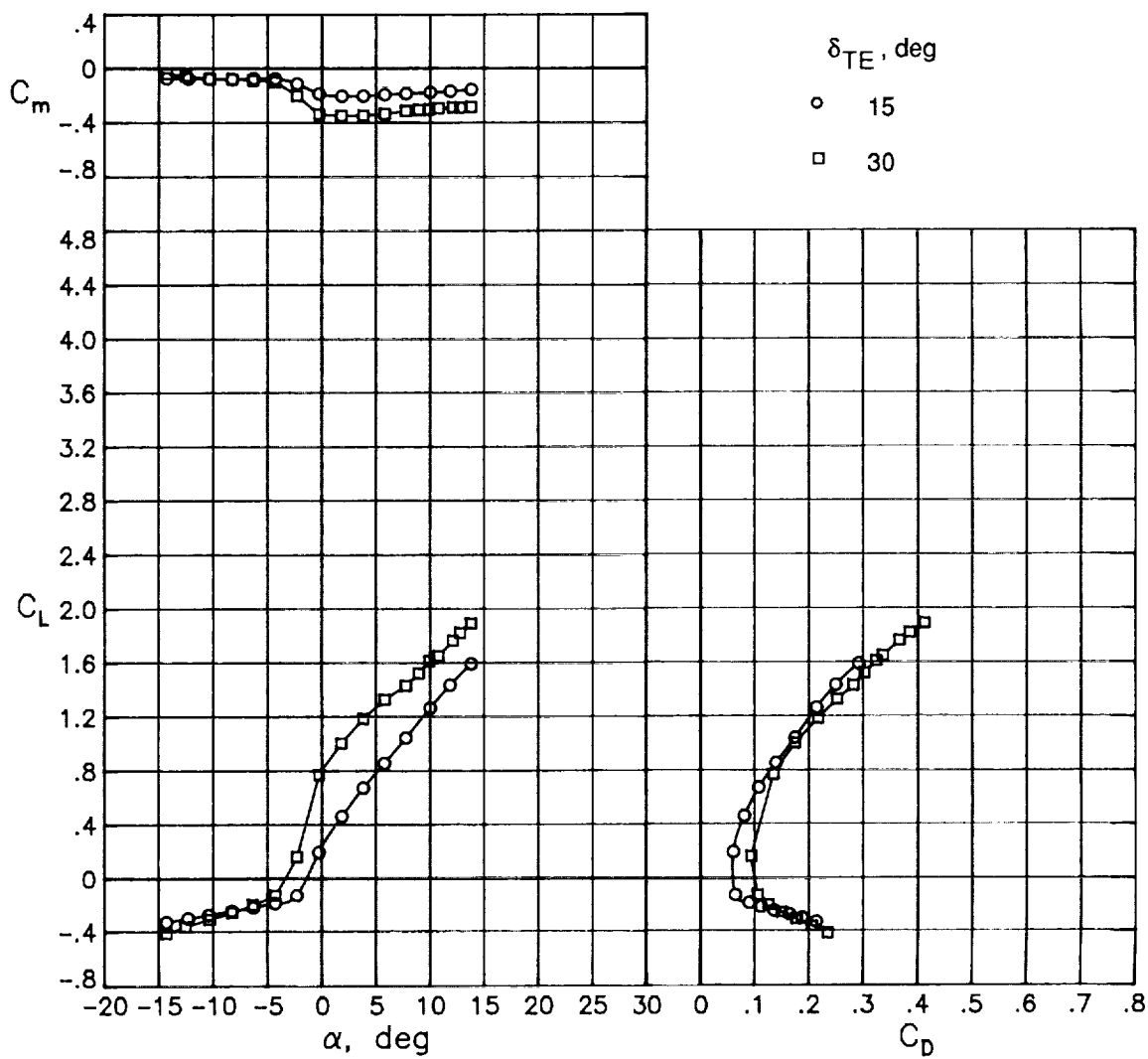
(c) $\delta_{LE} = -55°$; $q_\infty = 30$ psf.

Figure 7. Continued.
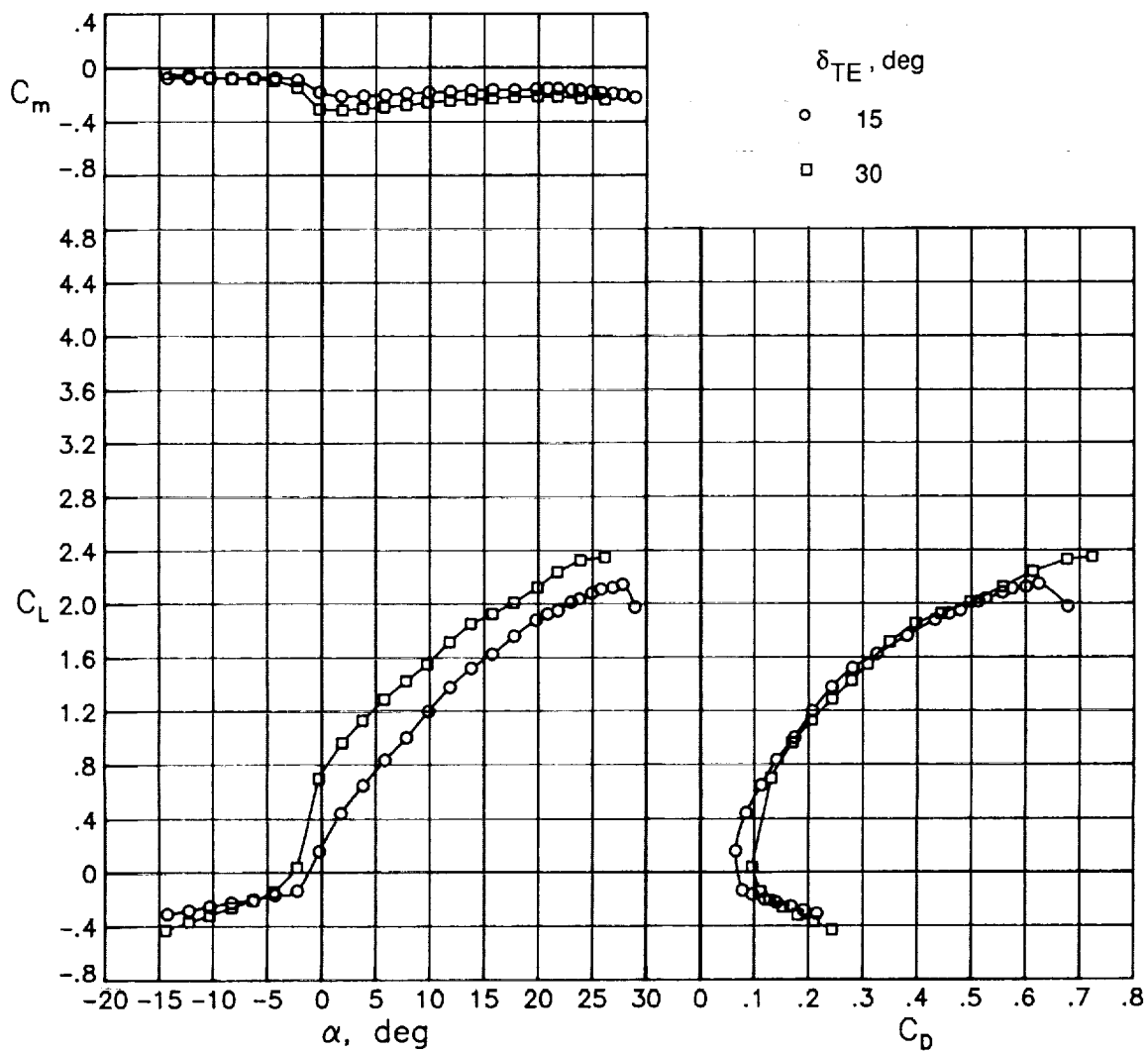
(d) $\delta_{LE} = -60°$; $q_\infty = 15$ psf.

Figure 7. Continued.
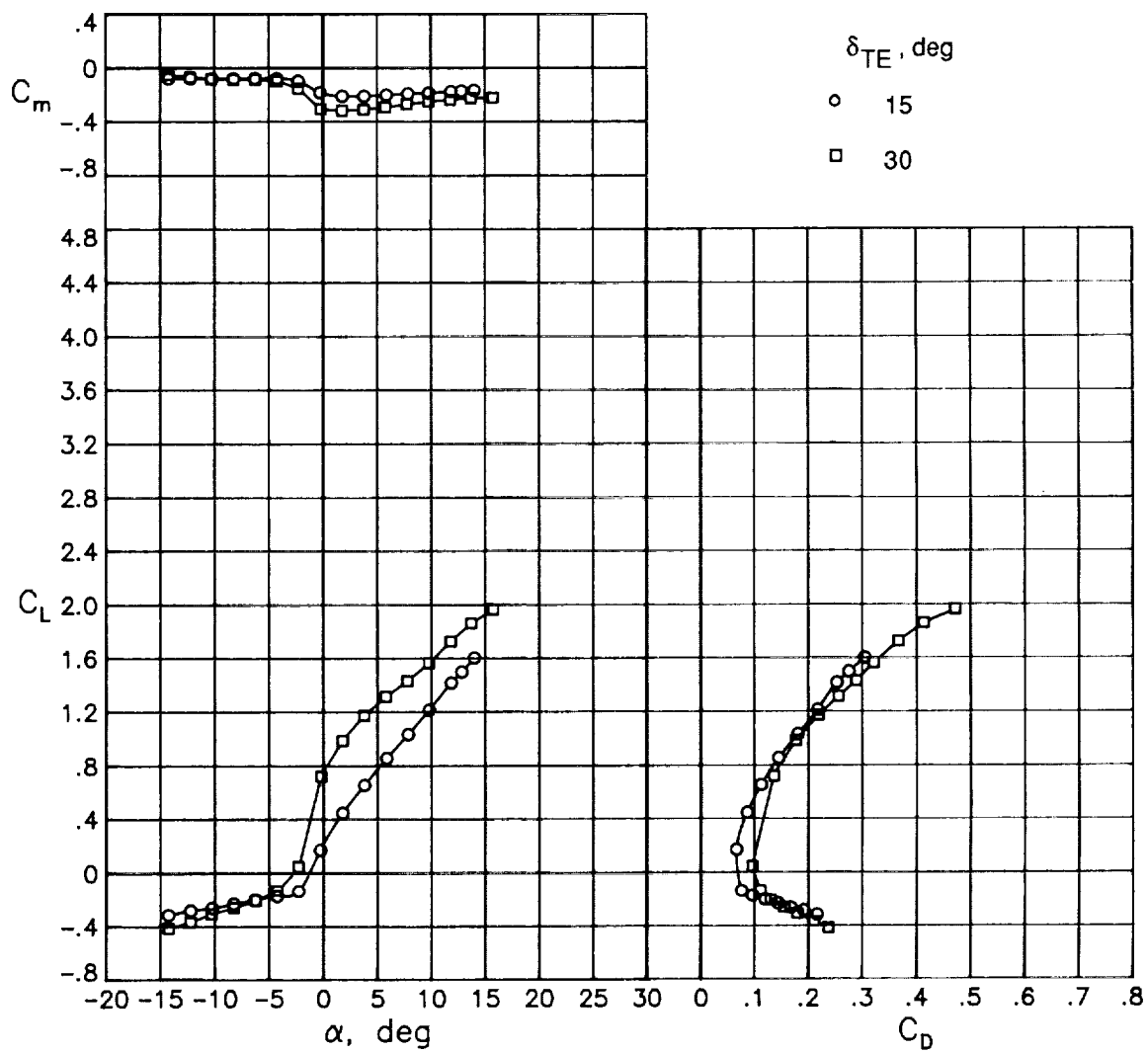
(e) $\delta_{LE} = -60°$; $q_\infty = 30$ psf.

Figure 7. Concluded.
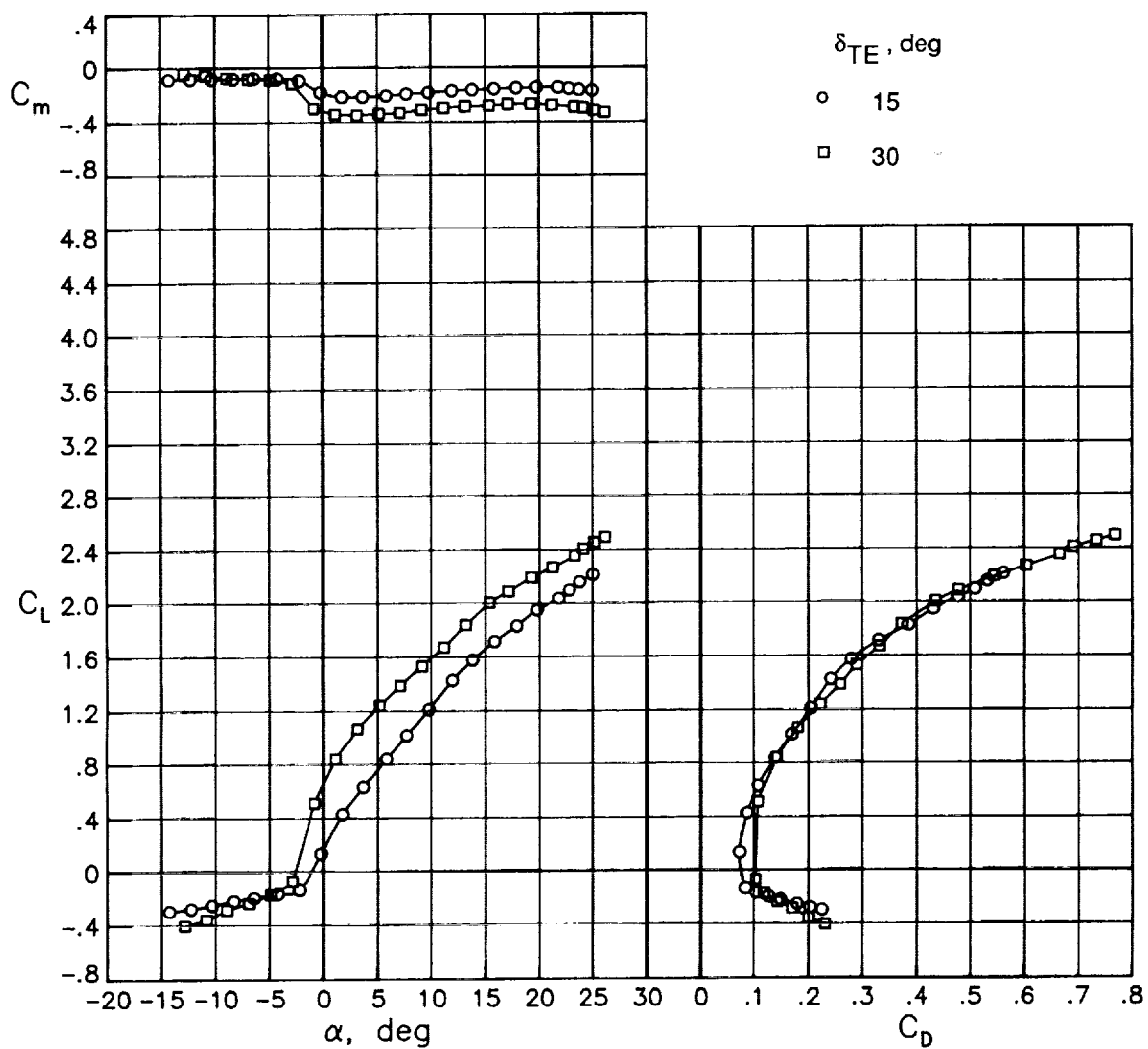
(a) $\delta_{LE} = -50°$; $q_\infty = 15$ psf.

Figure 8. Effect of trailing-edge flap deflection for 12-percent leading-edge flap configuration.
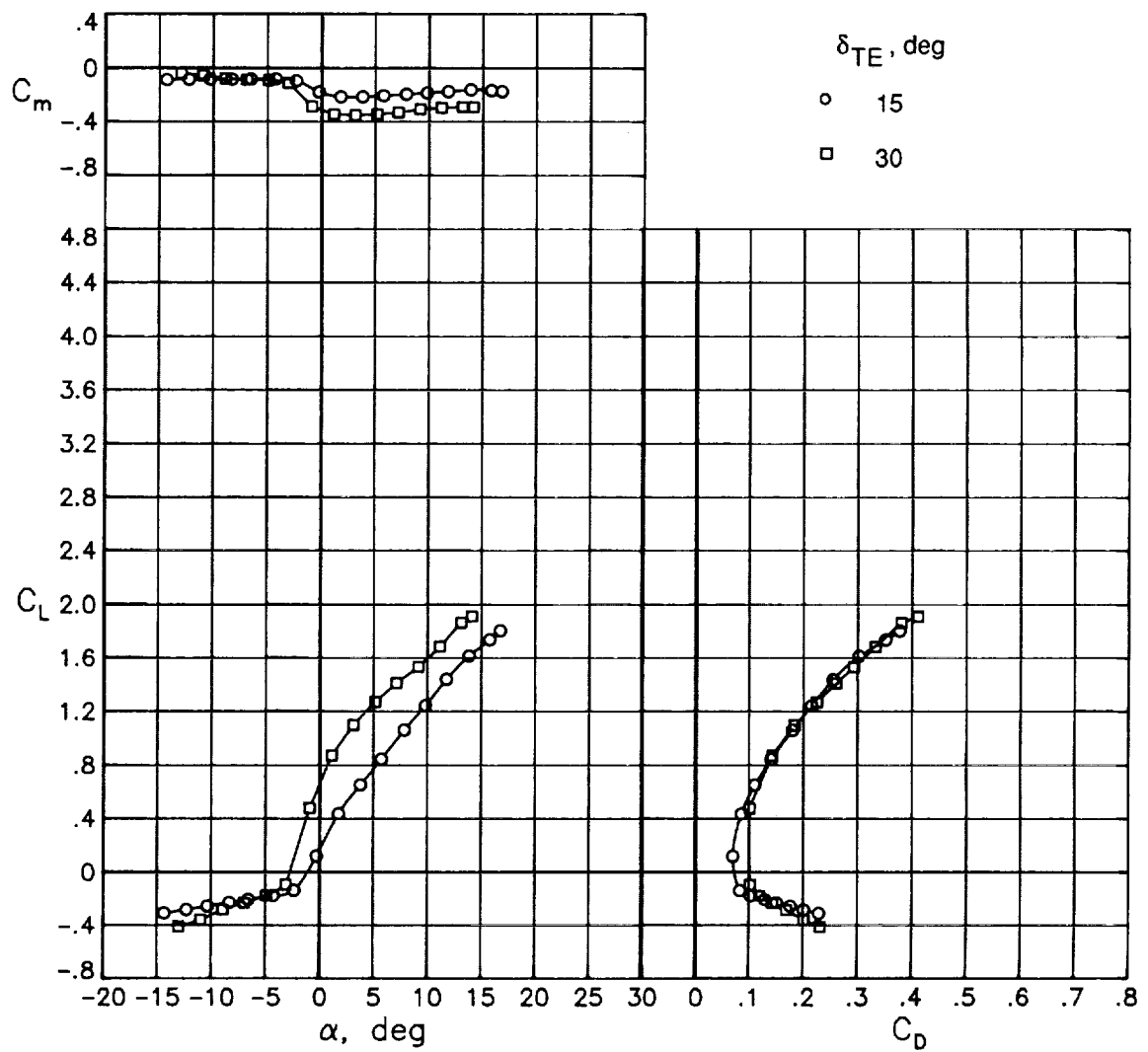
(b) $\delta_{LE} = -50°$; $q_\infty = 30$ psf.

Figure 8. Continued.
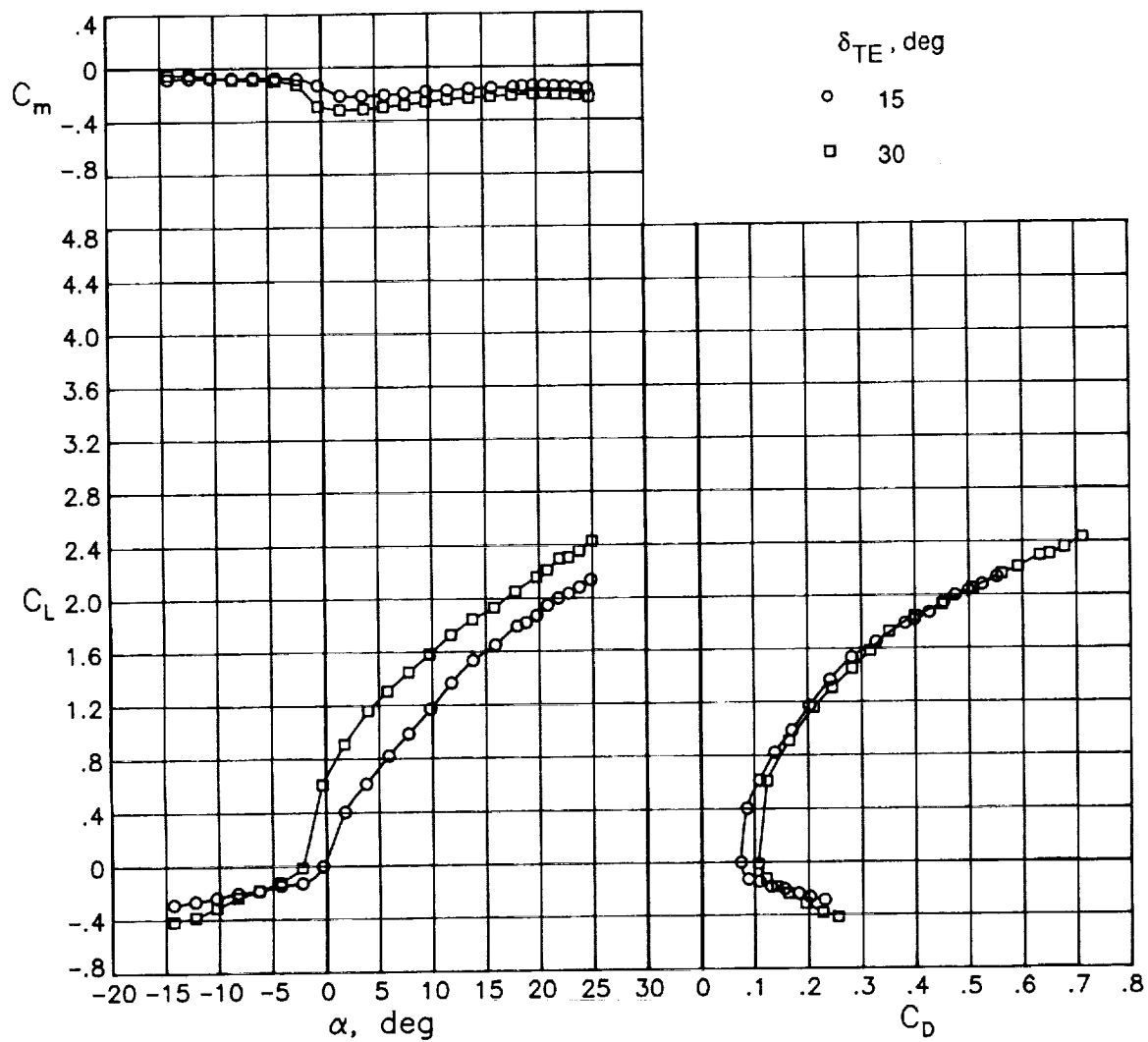
(c) $\delta_{LE} = -55°$; $q_\infty = 15$ psf.

Figure 8. Continued.
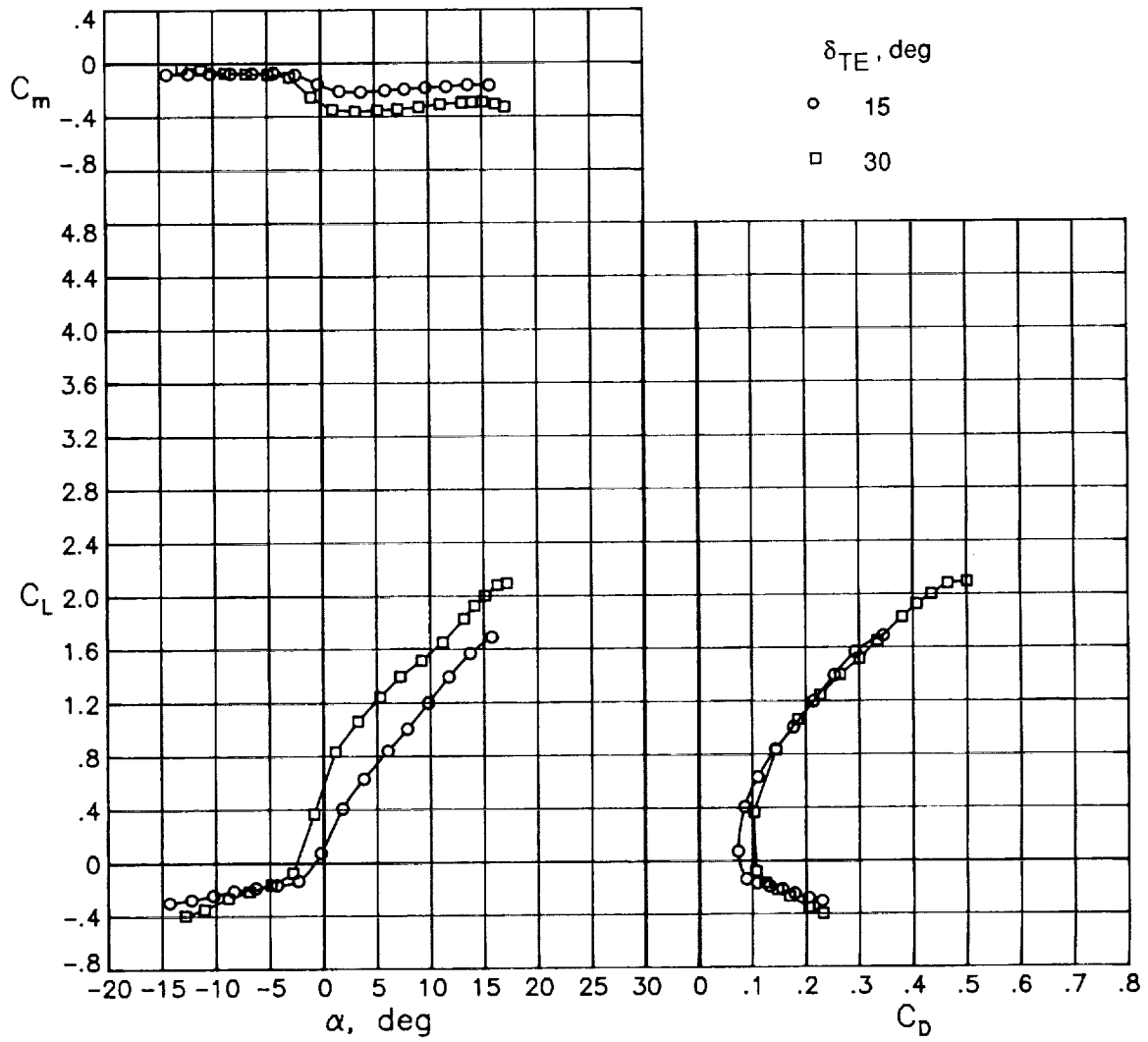
(d) $\delta_{LE} = -55°$; $q_\infty = 30$ psf.

Figure 8. Concluded.
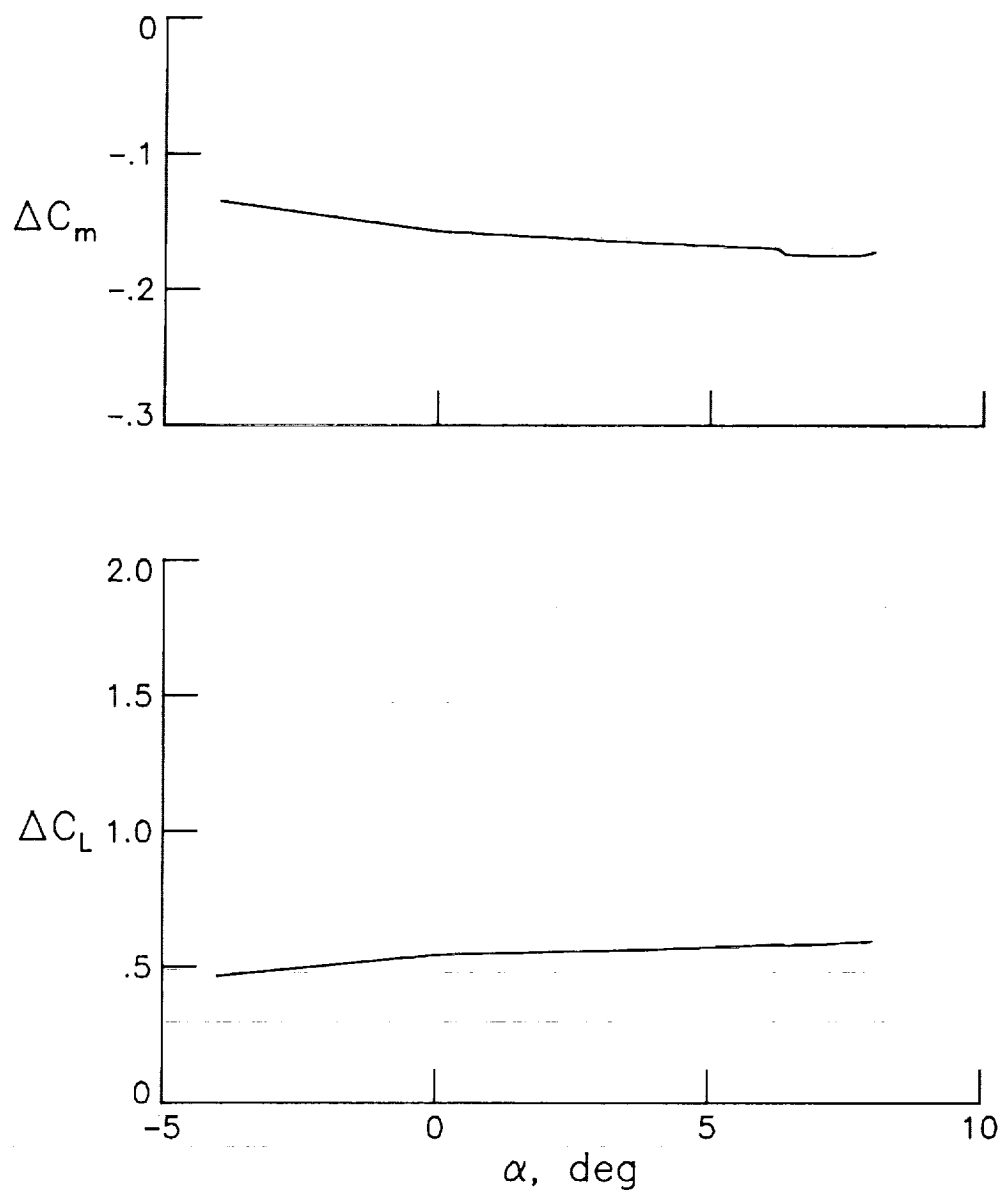
(a) Trailing-edge flap configuration; Δ for $\delta_{TE} = 15° -$ Cruise.

Figure 9. Effect of trailing-edge flap deflection on lift and pitching-moment coefficients. $q_\infty = 30$ psf.
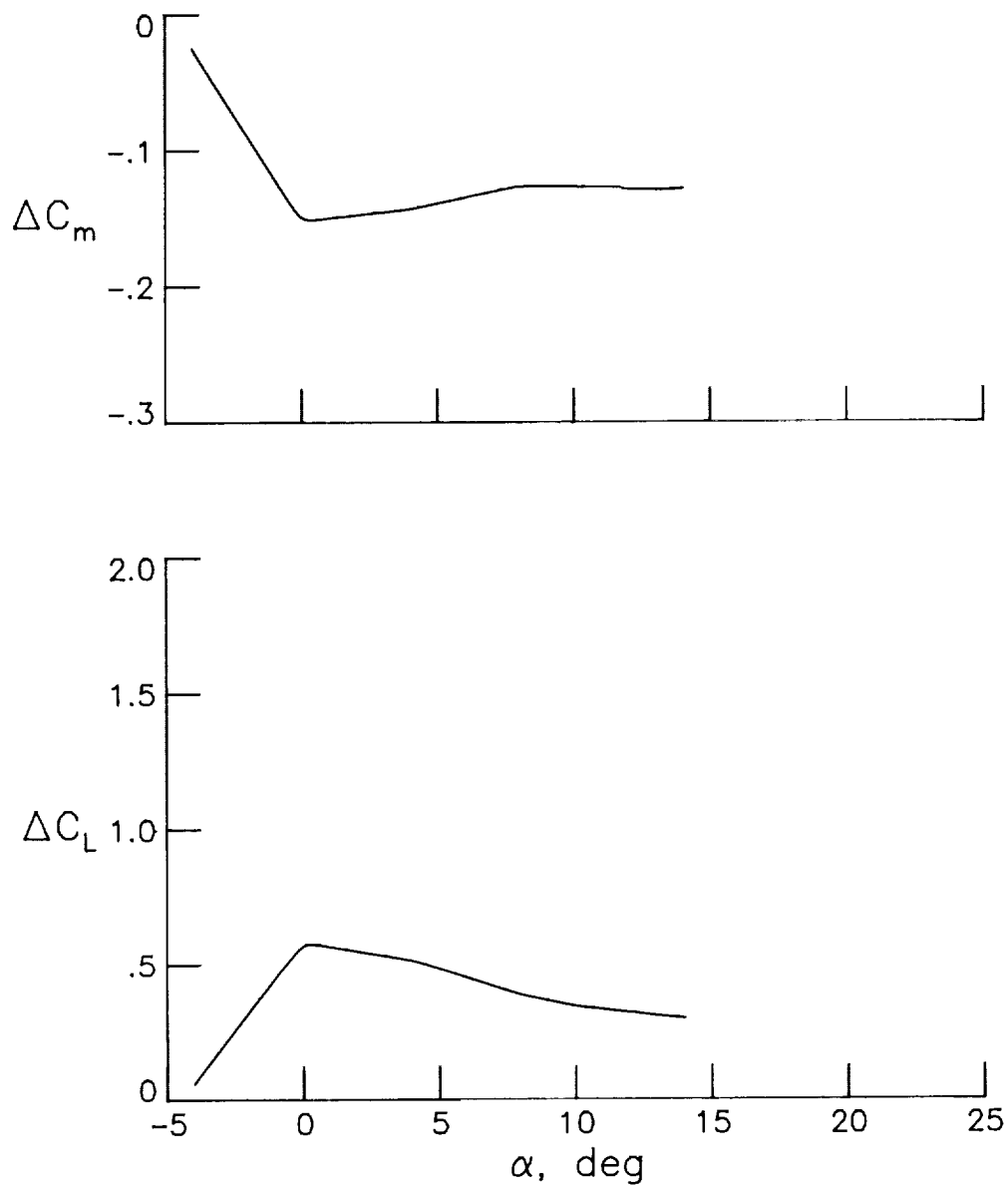
(b) 10-percent leading-edge flap configuration; $\delta_{LE} = -55°$; Δ for $\delta_{TE} = 30° - \delta_{TE} = 15°$.

Figure 9. Continued.
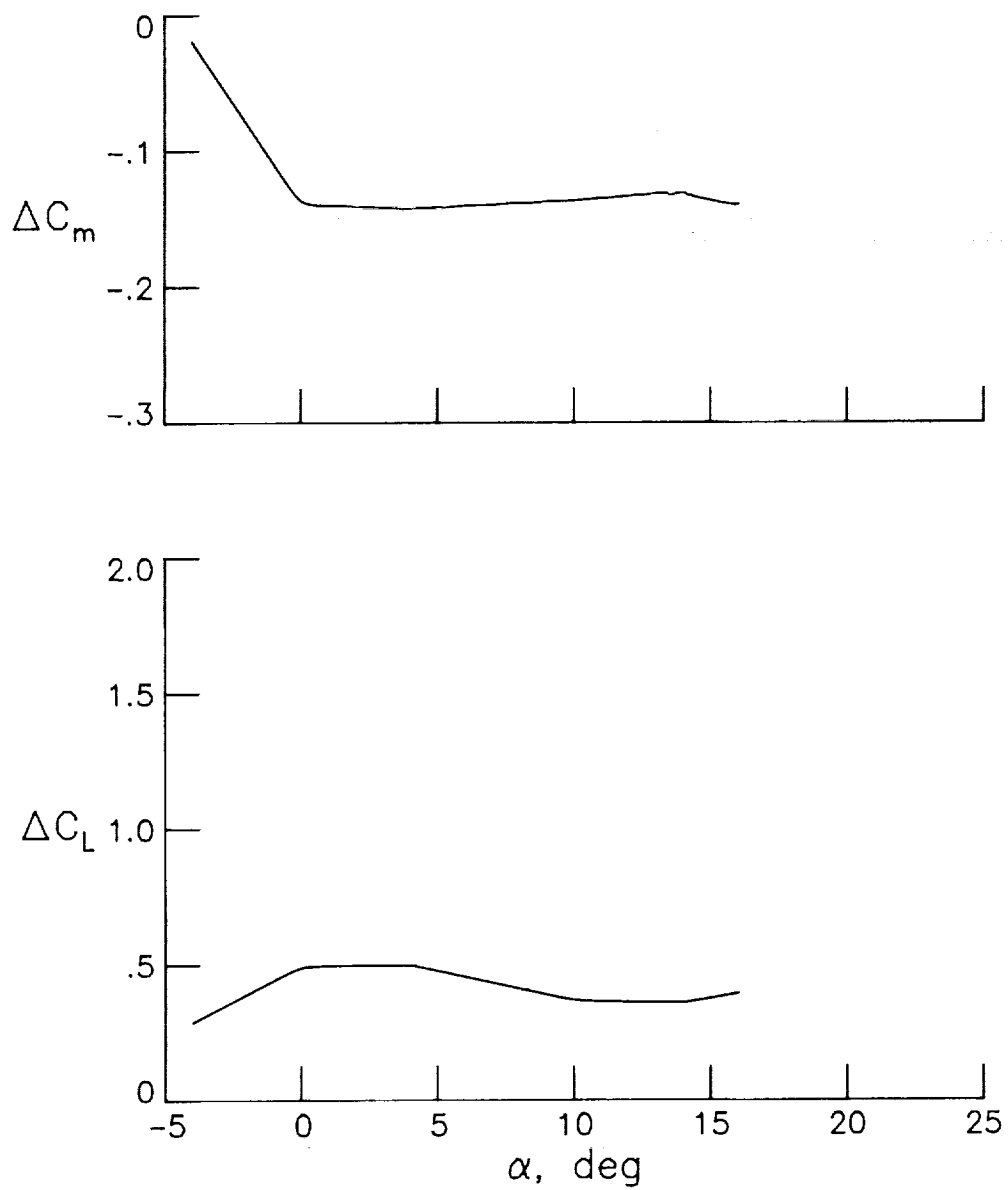
(c) 12-percent leading-edge flap configuration; $\delta_{LE} = -55°$; Δ for $\delta_{TE} = 30° - \delta_{TE} = 15°$.

Figure 9. Concluded.
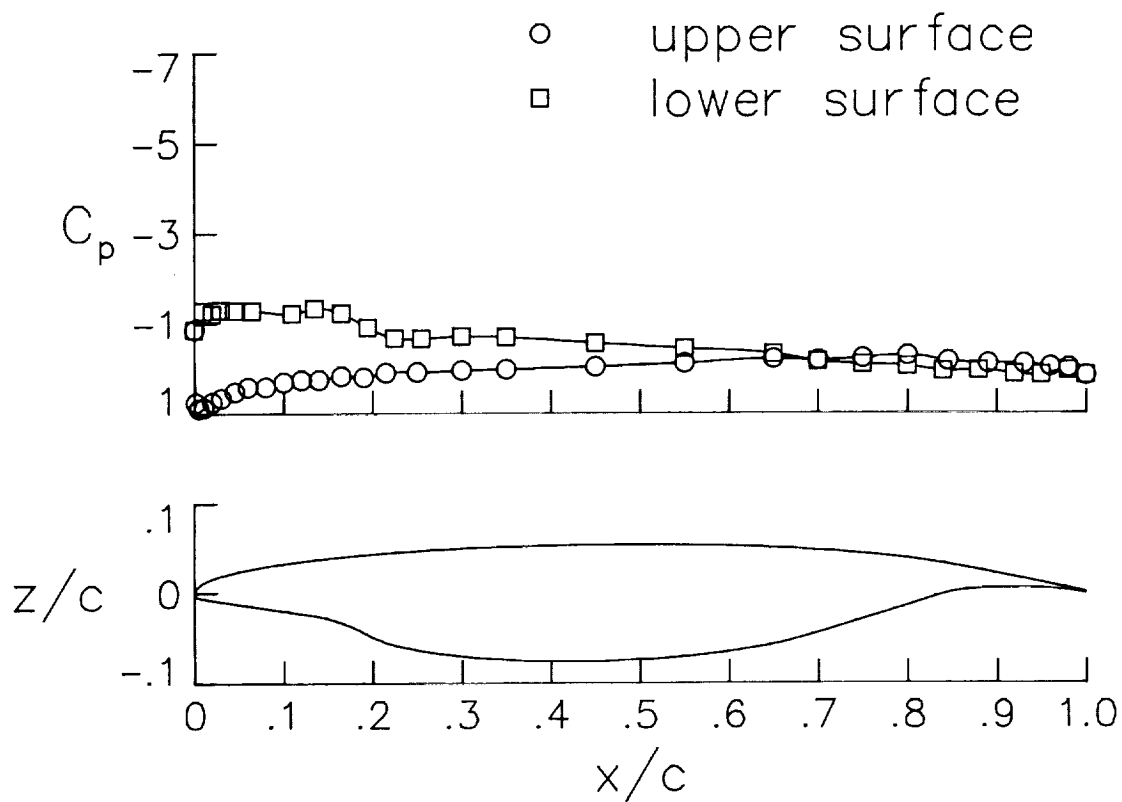
(a) $\alpha = -8.2°$.
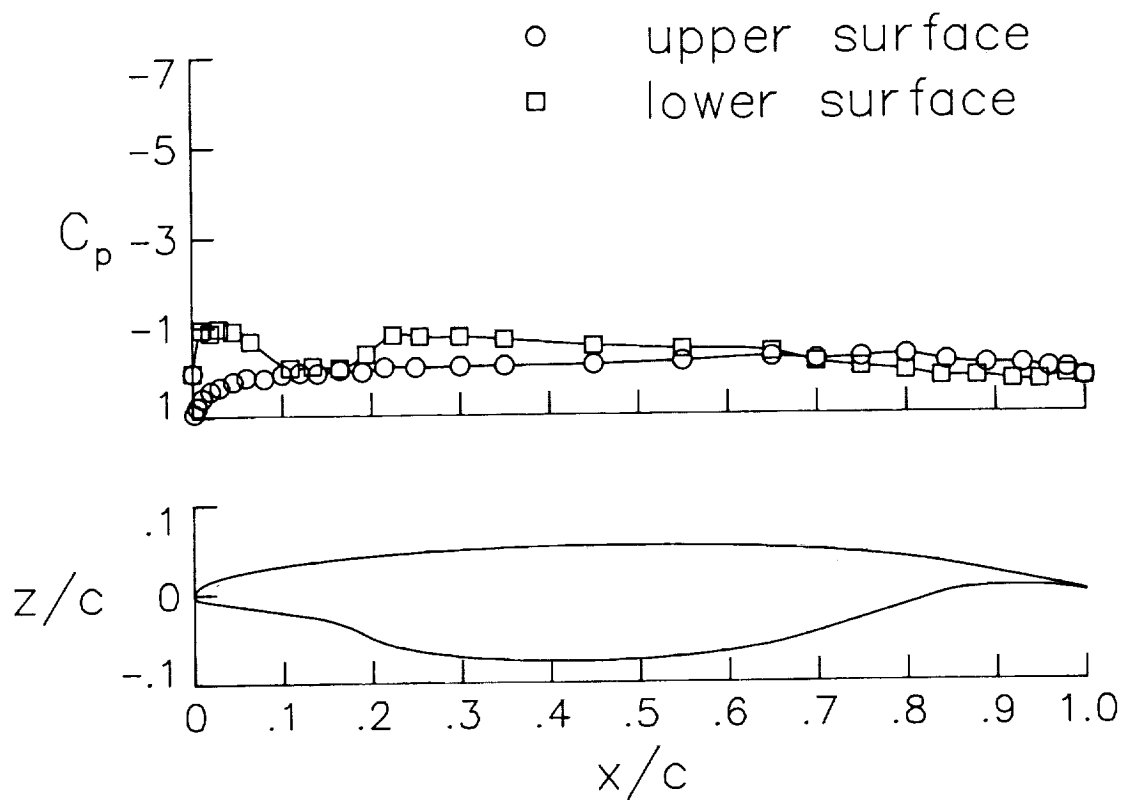
(b) $\alpha = -4.2°$.

Figure 10. Pressure distributions for cruise configuration. $q_\infty = 30$ psf.
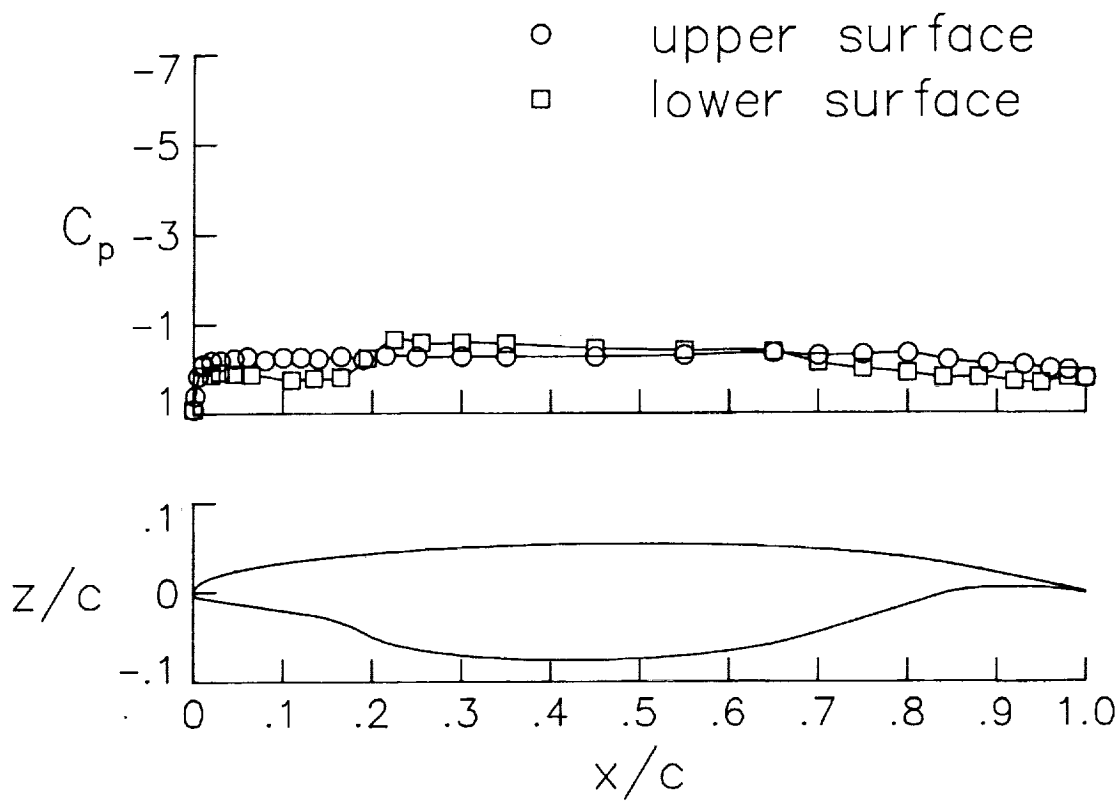
(c) $\alpha = -0.2°$.
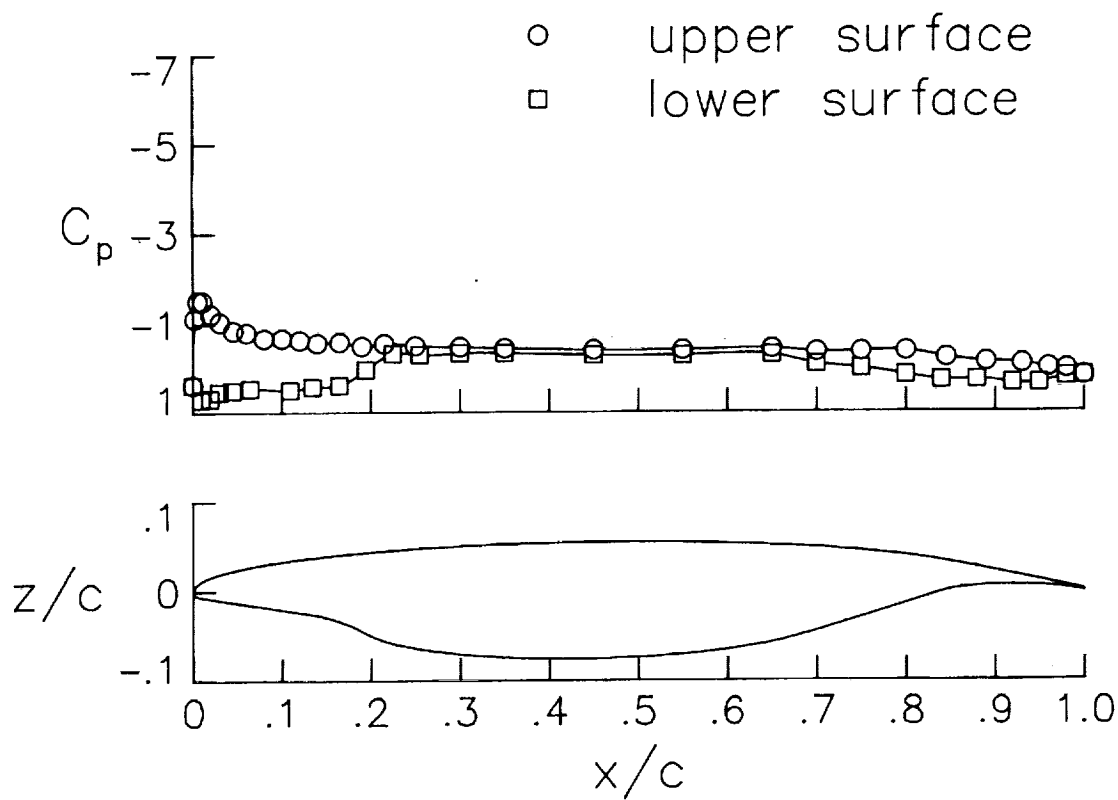
(d) $\alpha = 3.8°$.

Figure 10. Continued.
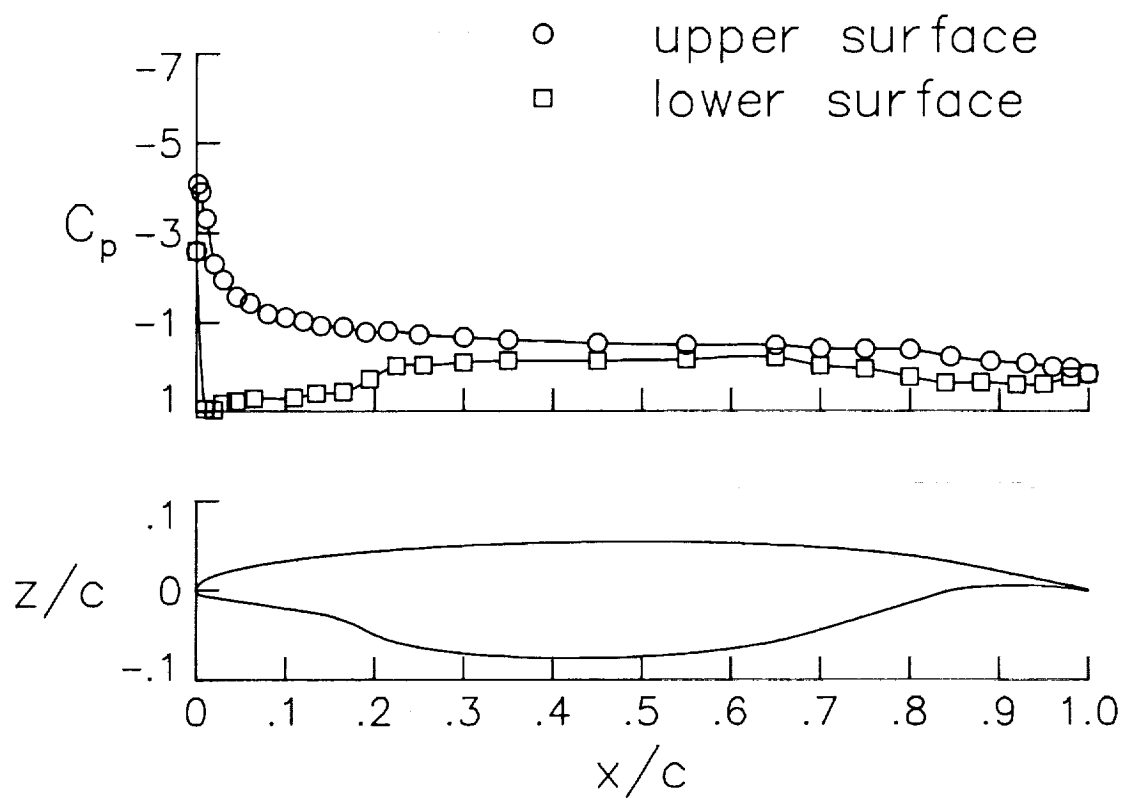
(e) $\alpha = 7.8°$.

Figure 10. Concluded.
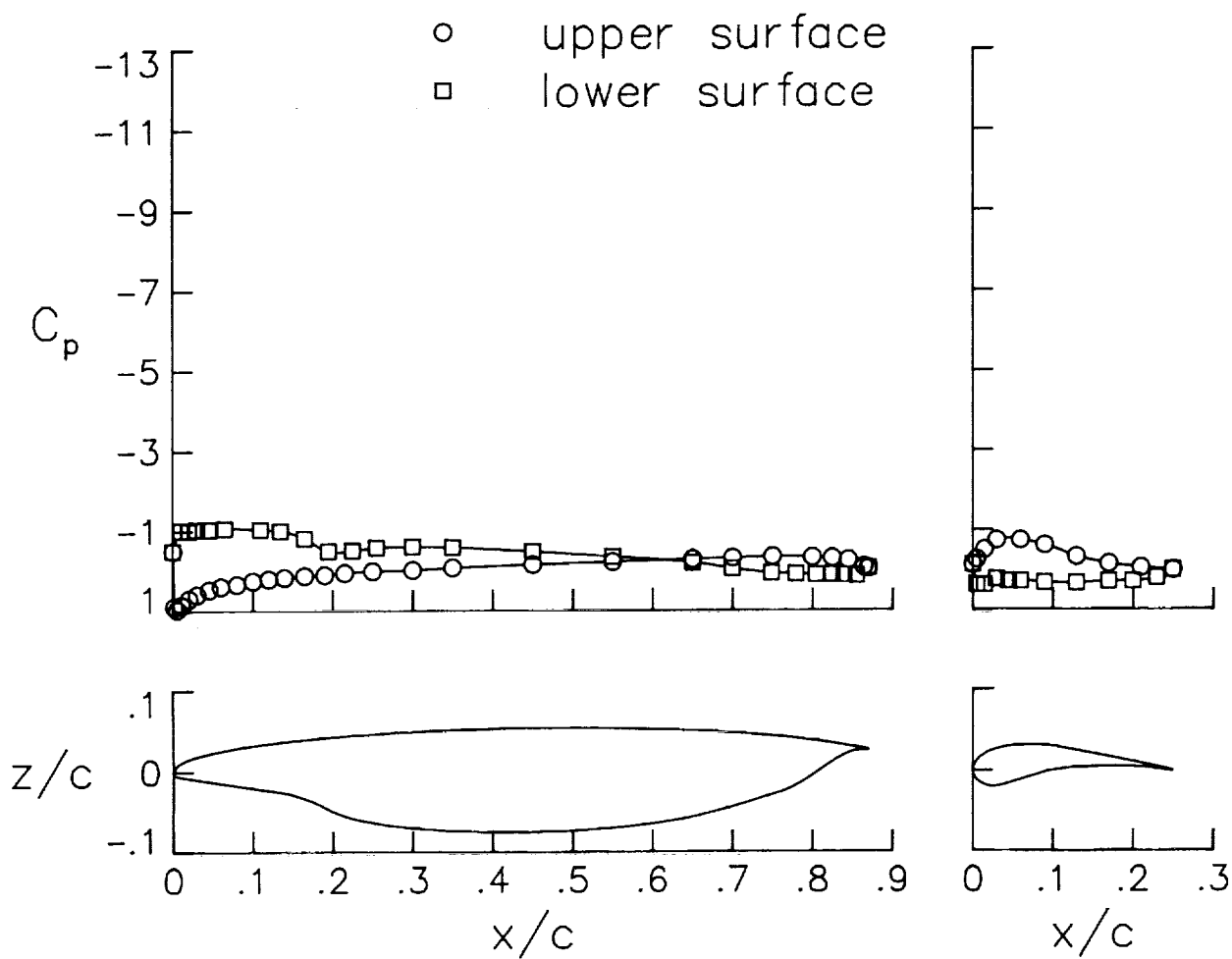
(a) $\alpha = -8.3°$.

Figure 11. Pressure distributions for trailing-edge flap configuration. $\delta_{TE} = 15°$; $q_\infty = 30$ psf.
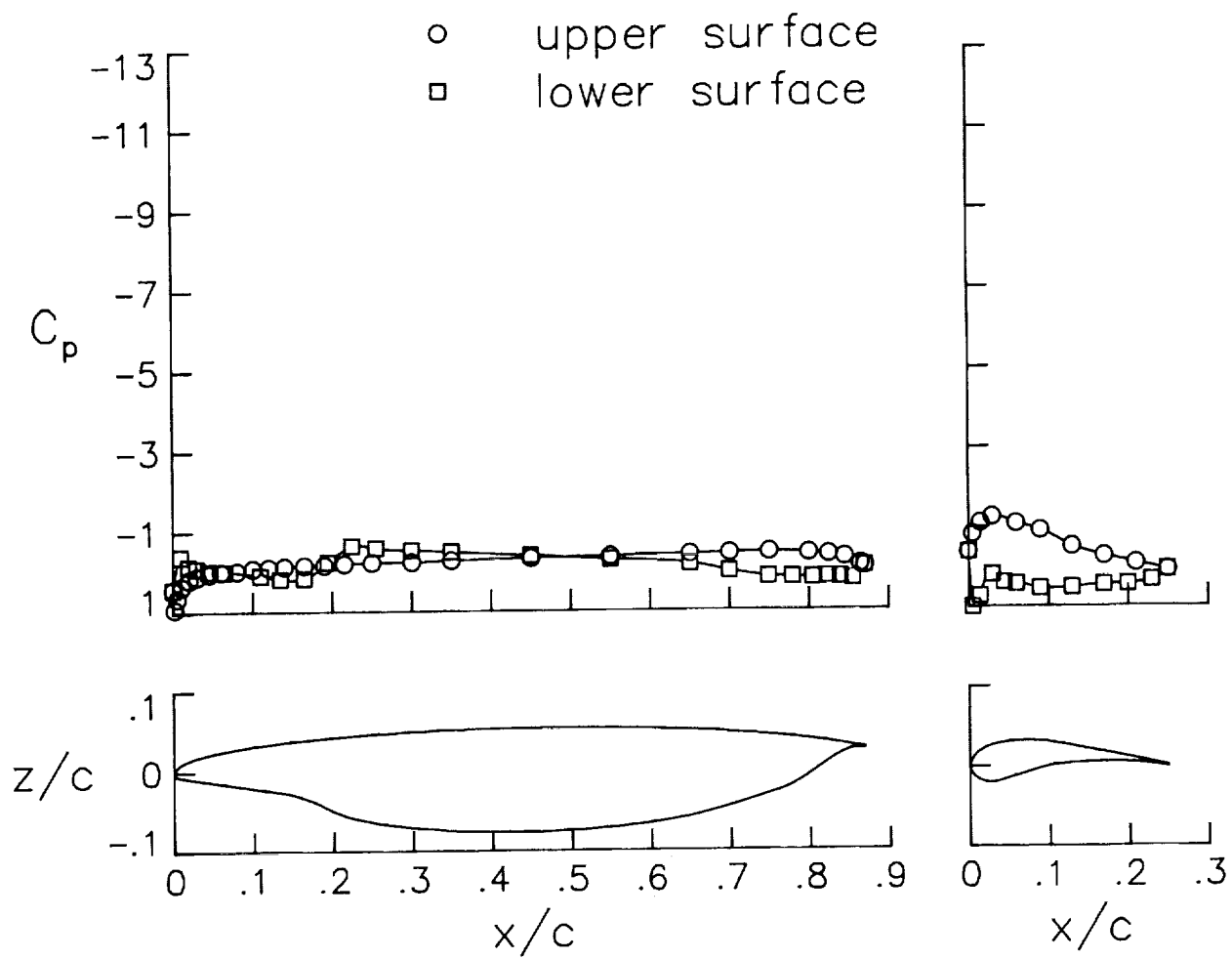
(b) $\alpha = -4.2°$.

Figure 11. Continued.
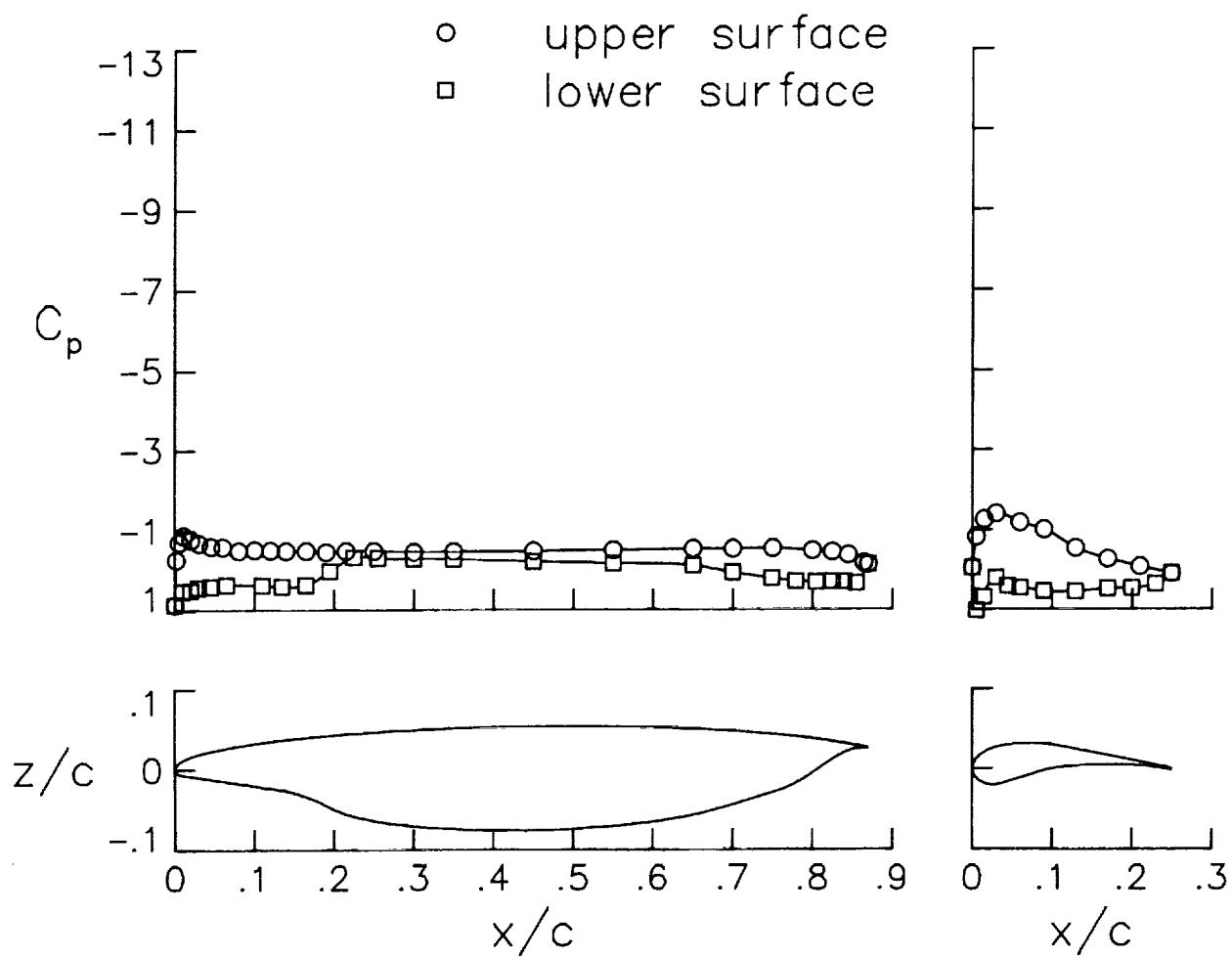
(c) $\alpha = -0.1°$.

Figure 11. Continued.
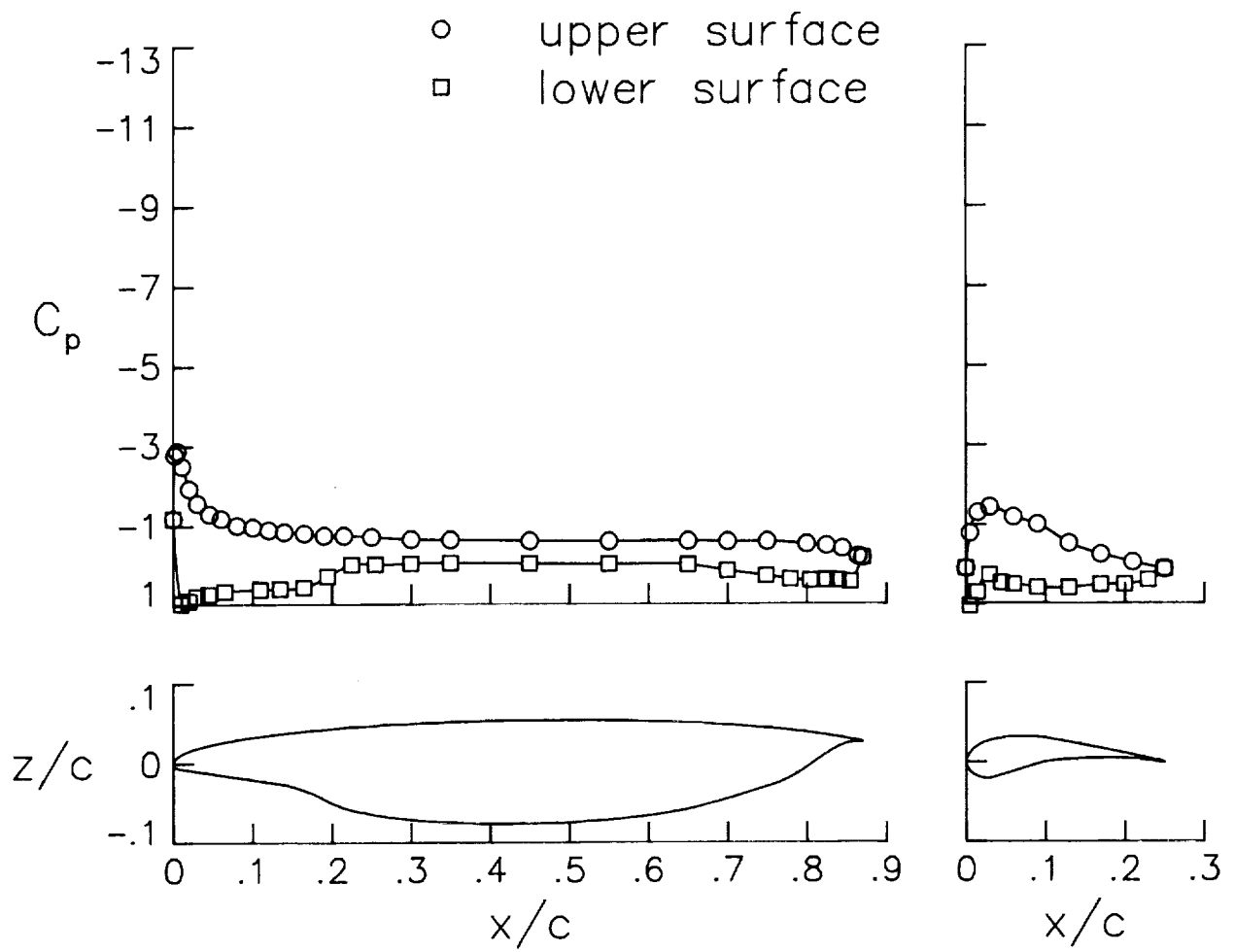
(d) $\alpha = 3.8°$.

Figure 11. Continued.
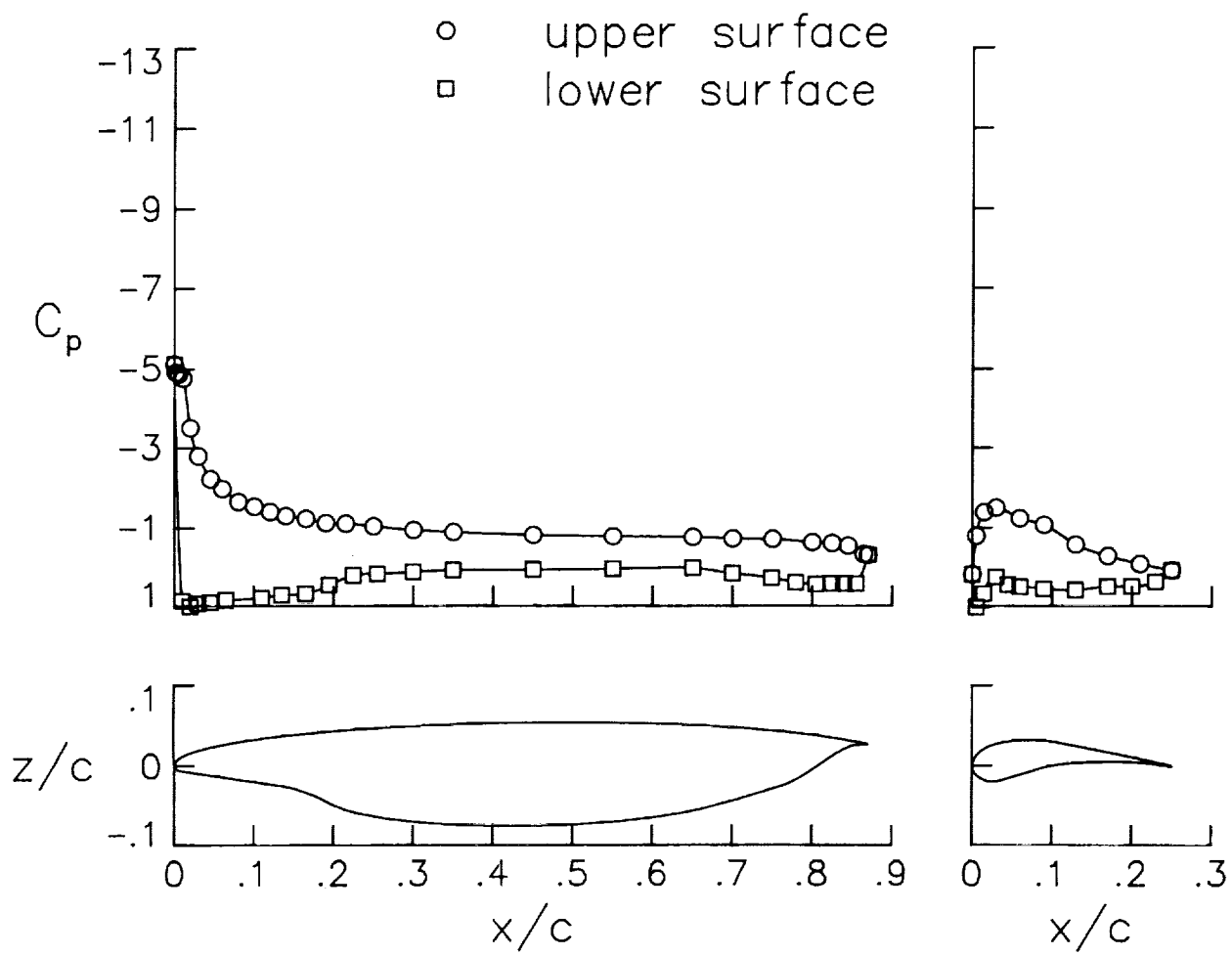
(e) $\alpha = 7.8°$.

Figure 11. Concluded.
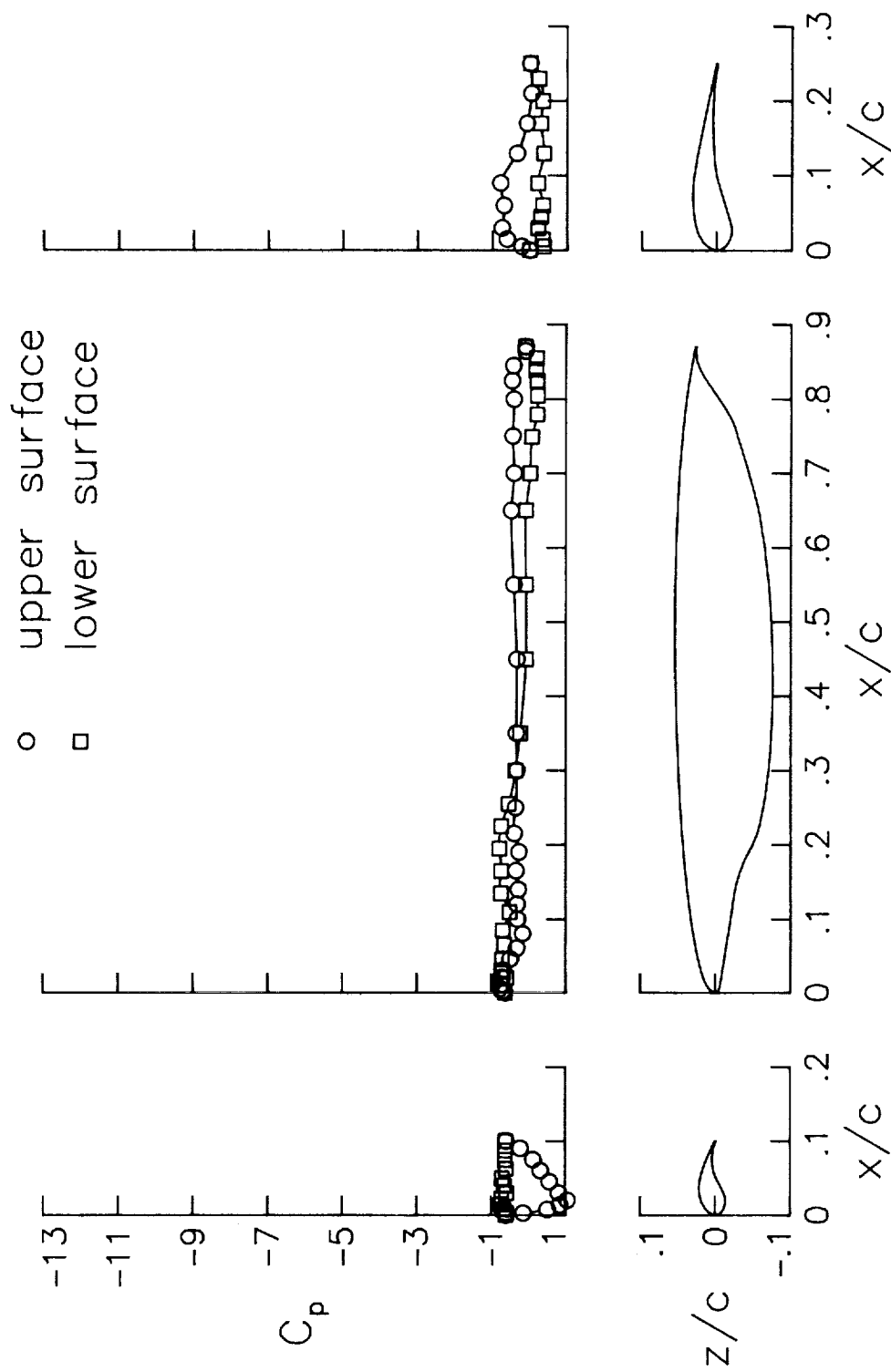
Figure 12. Pressure distributions for 10-percent leading-edge flap configuration. $\delta_{LE} = -55°$; $\delta_{TE} = 15°$; $q_\infty = 30$ psf.

(a) $\alpha = -0.2°$.
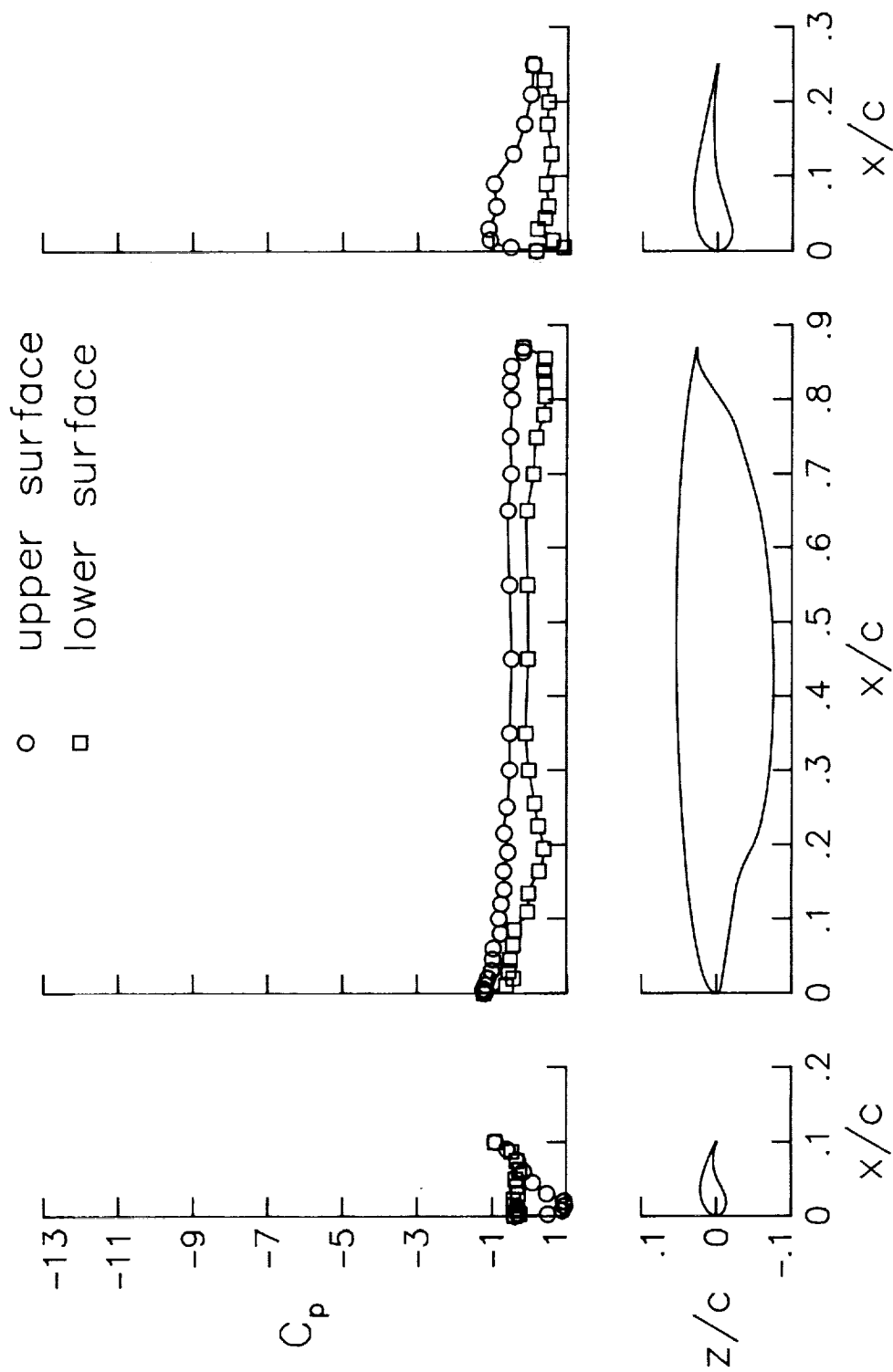
(b) $\alpha = 3.9°$.

Figure 12. Continued.
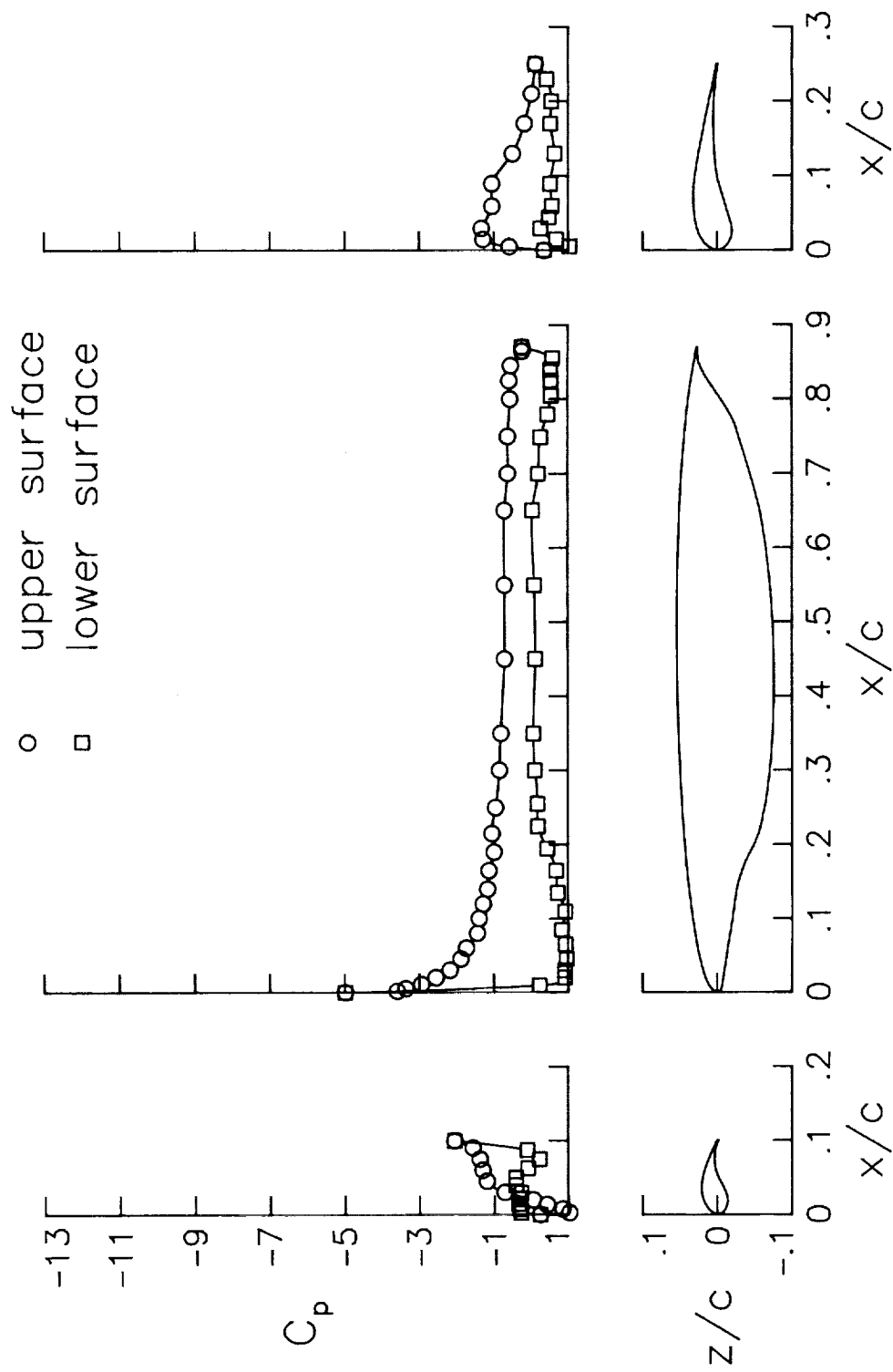
(c) $\alpha = 10.0°$.

Figure 12. Continued.
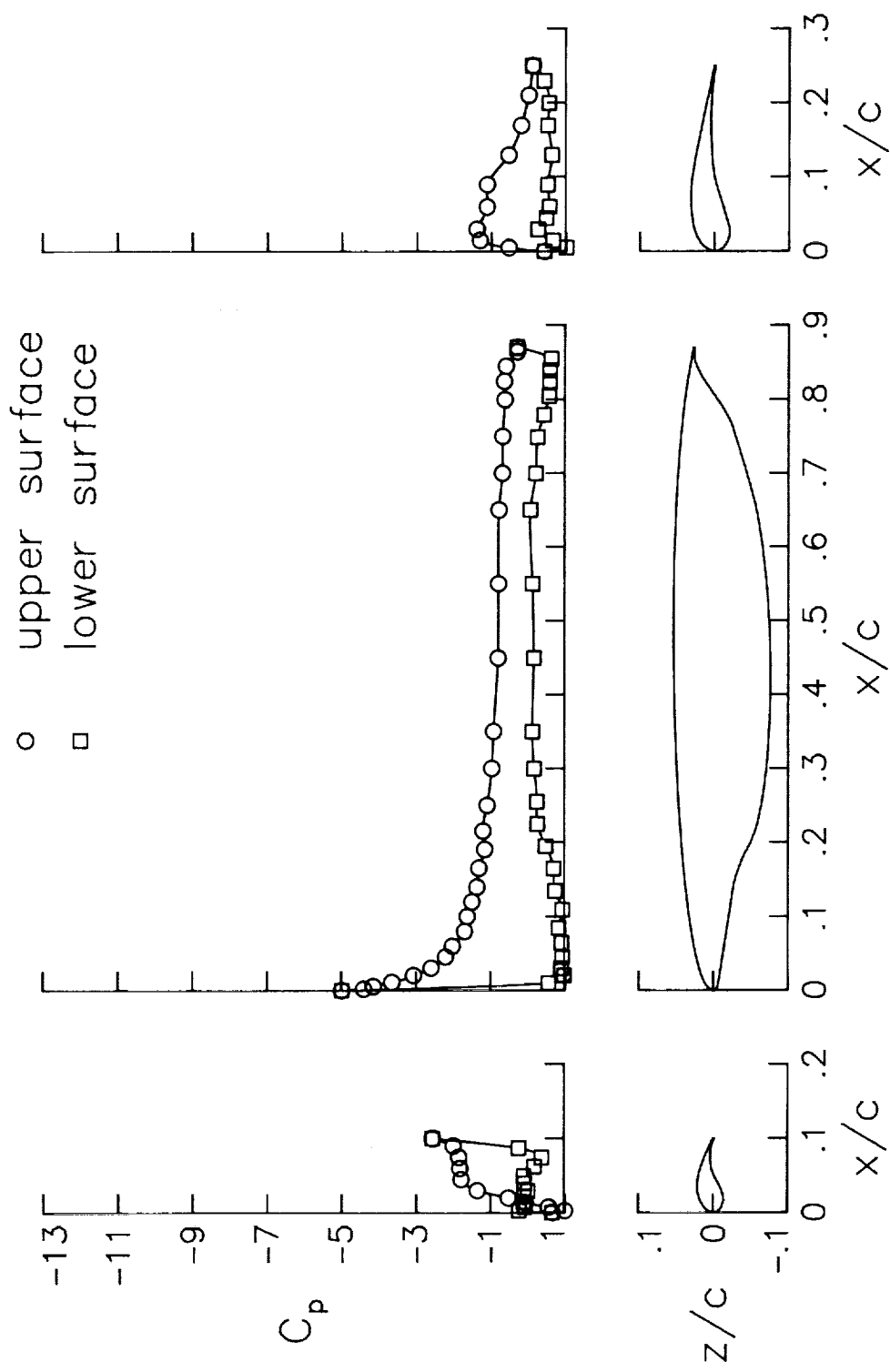
(d) $\alpha = 11.9°$.

Figure 12. Continued.
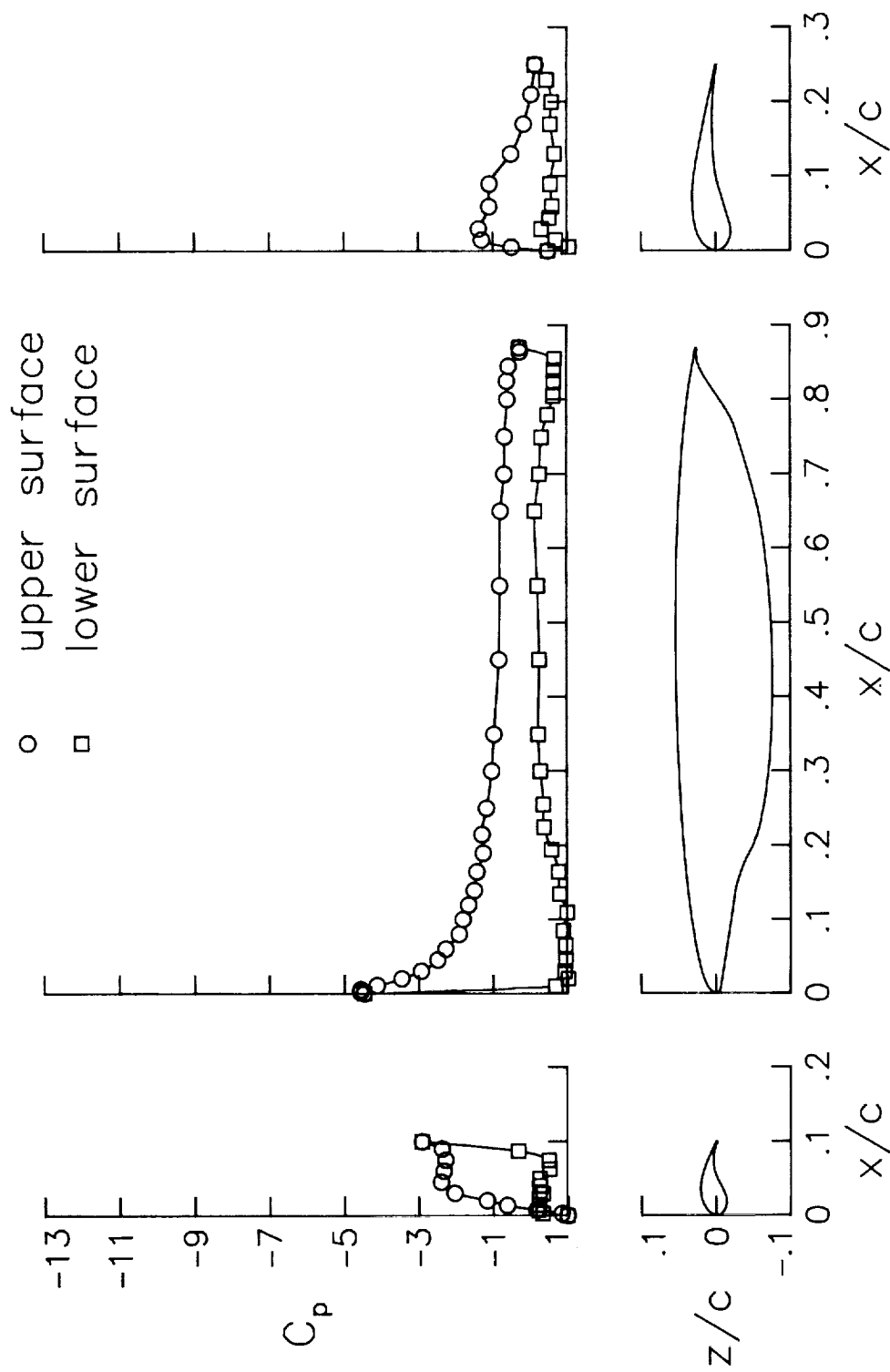
(e) $\alpha = 13.8°$.

Figure 12. Concluded.
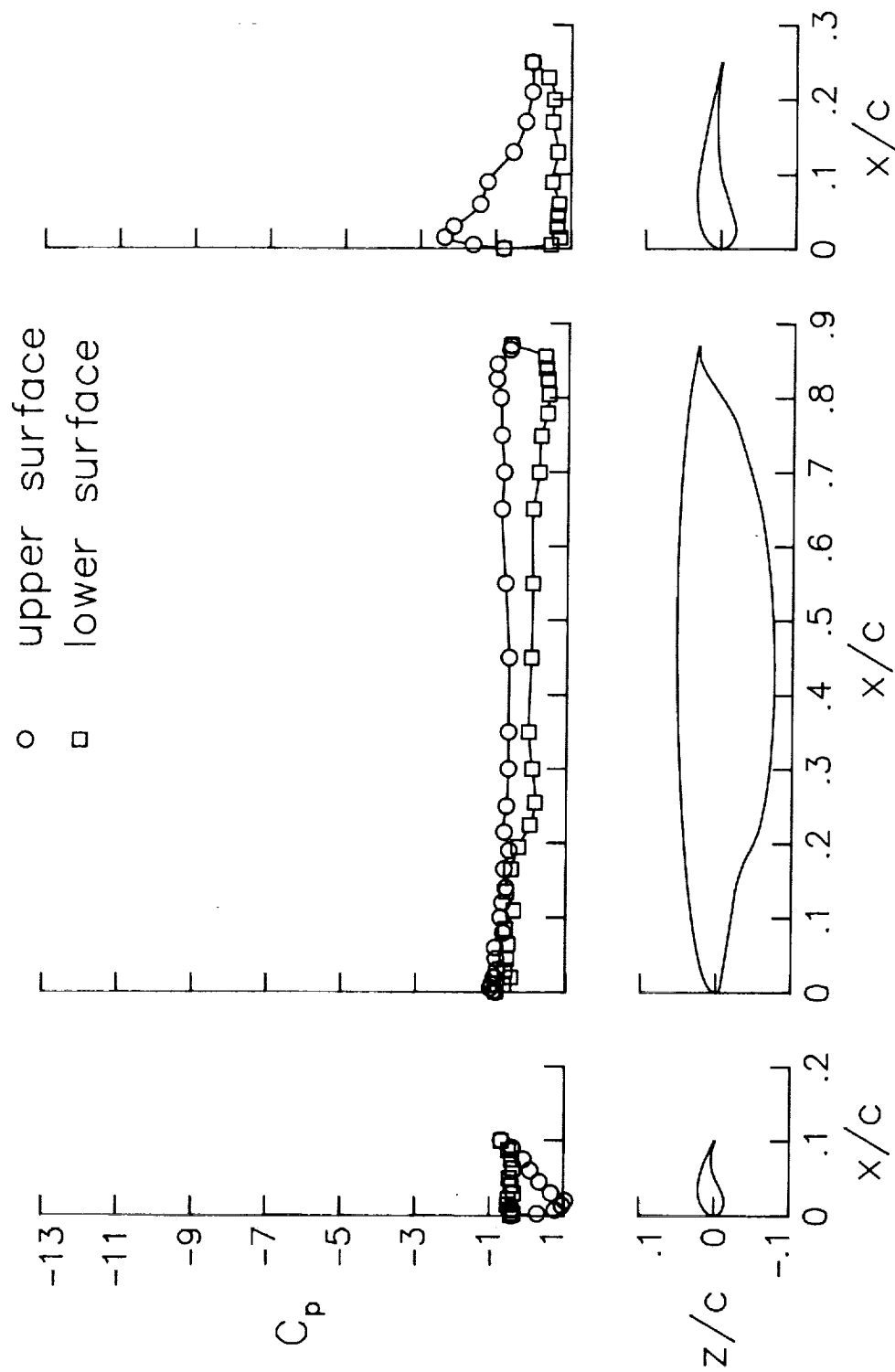
Figure 13. Pressure distributions for 10-percent leading-edge flap configuration. $\delta_{LE} = -55°$; $\delta_{TE} = 30°$; $q_\infty = 30$ psf.

(a) $\alpha = -0.2°$.

upper surface

lower surface

C_p

z/c

x/c
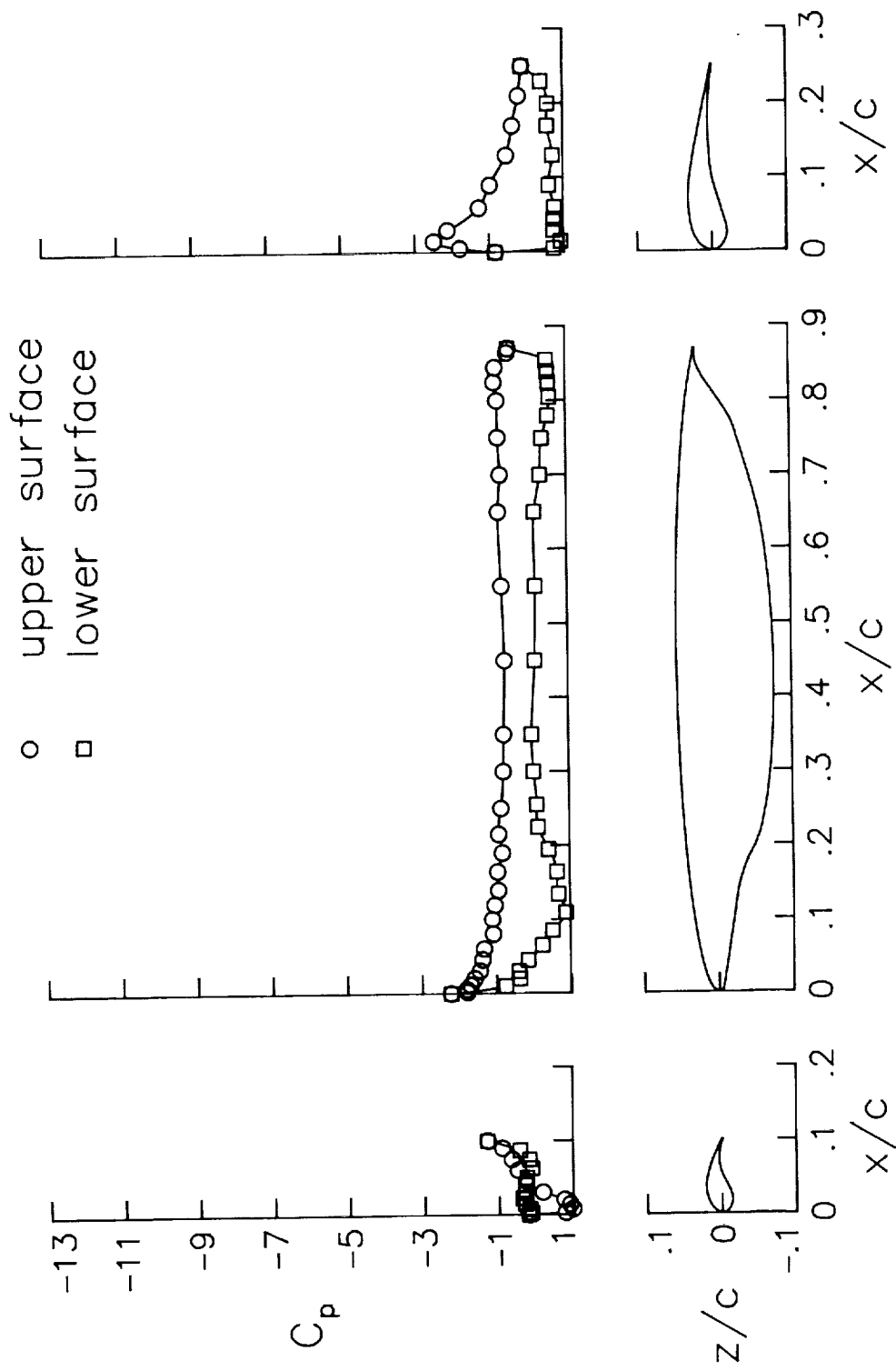
(b) $\alpha = 3.9°$.

Figure 13. Continued.
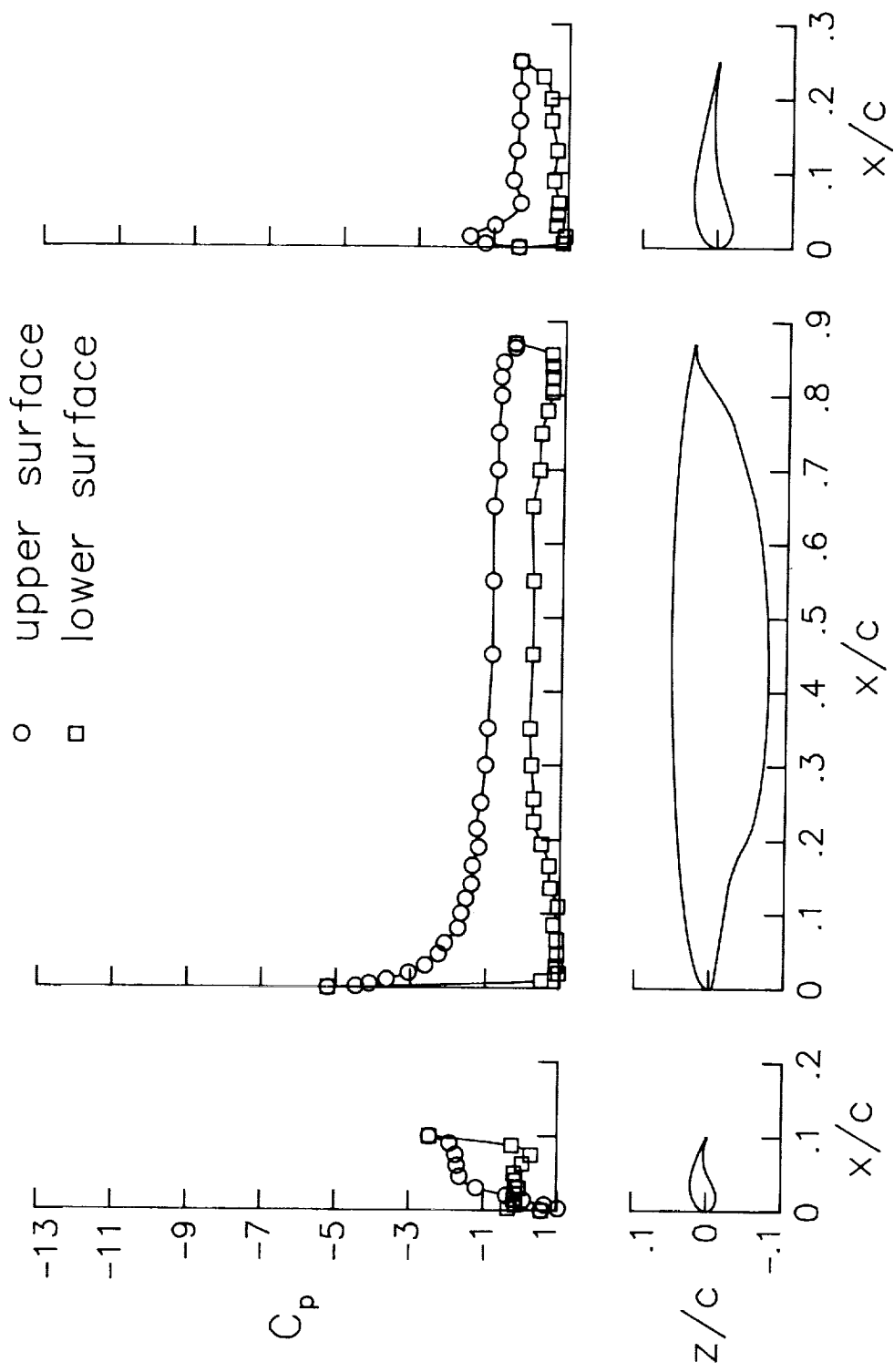
(c) $\alpha = 10.0°$.

Figure 13. Continued.
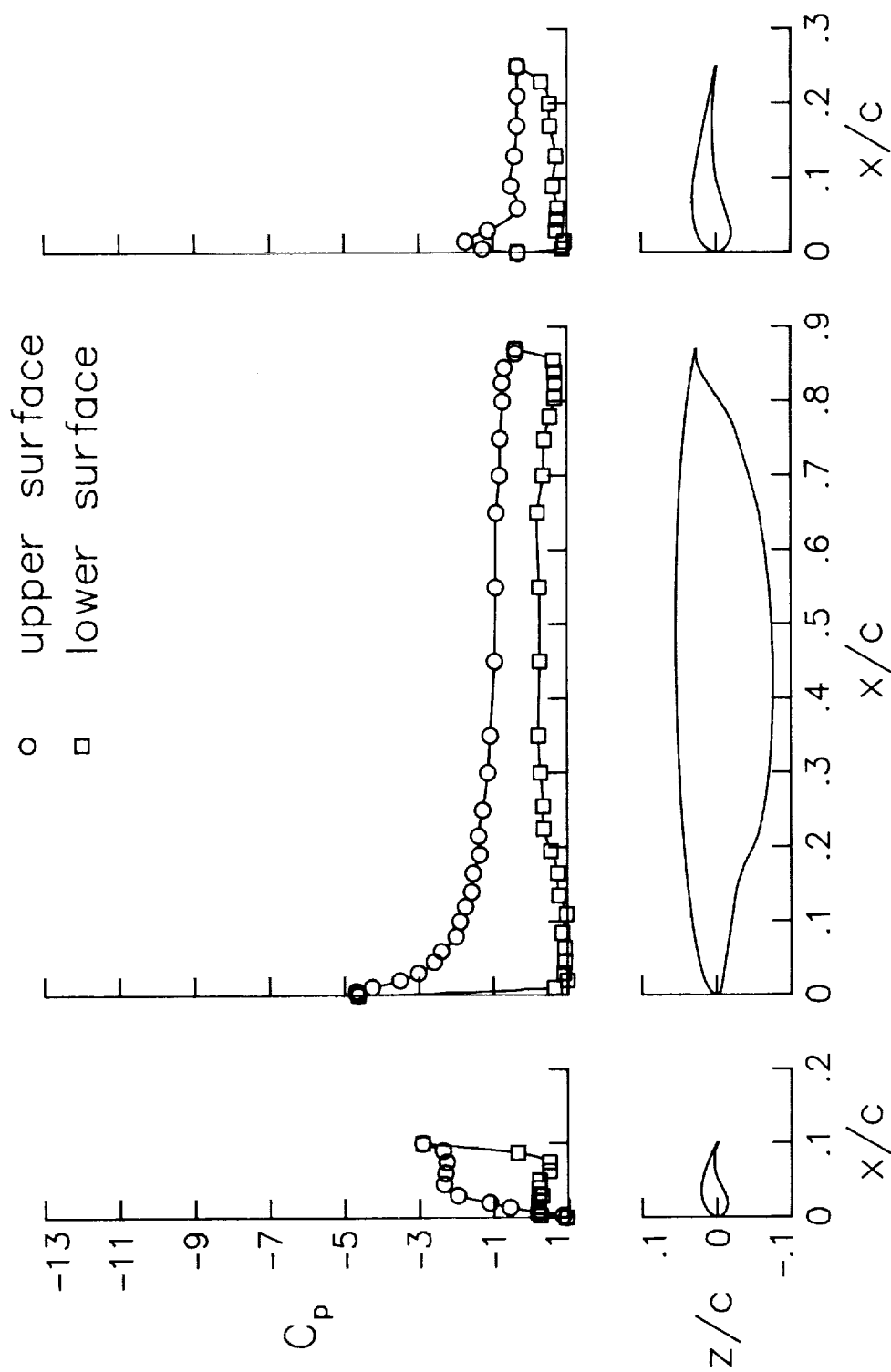
(d) $\alpha = 12.1°$.

Figure 13. Continued.
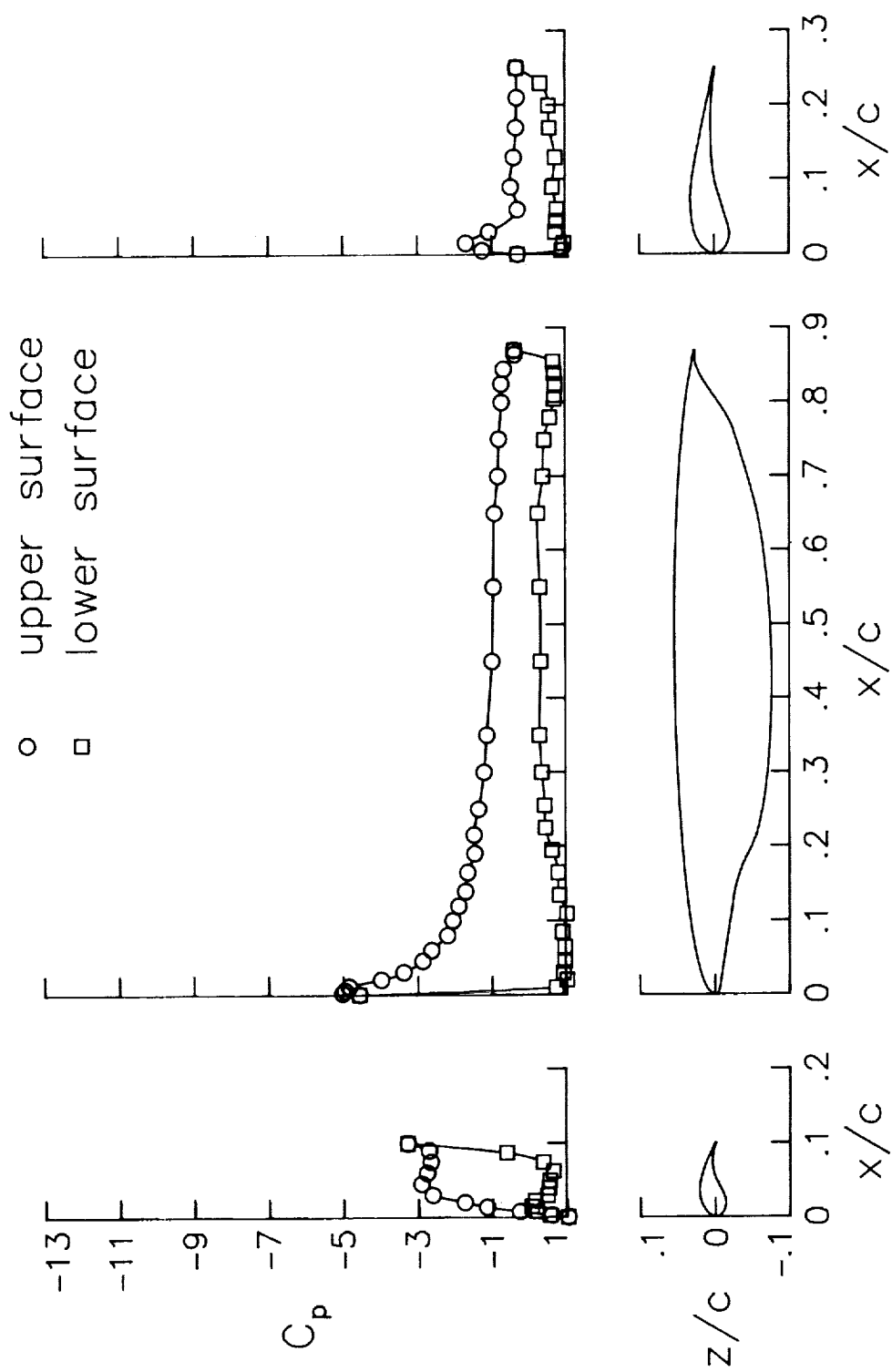
(e) $\alpha = 13.8°$.

Figure 13. Concluded.
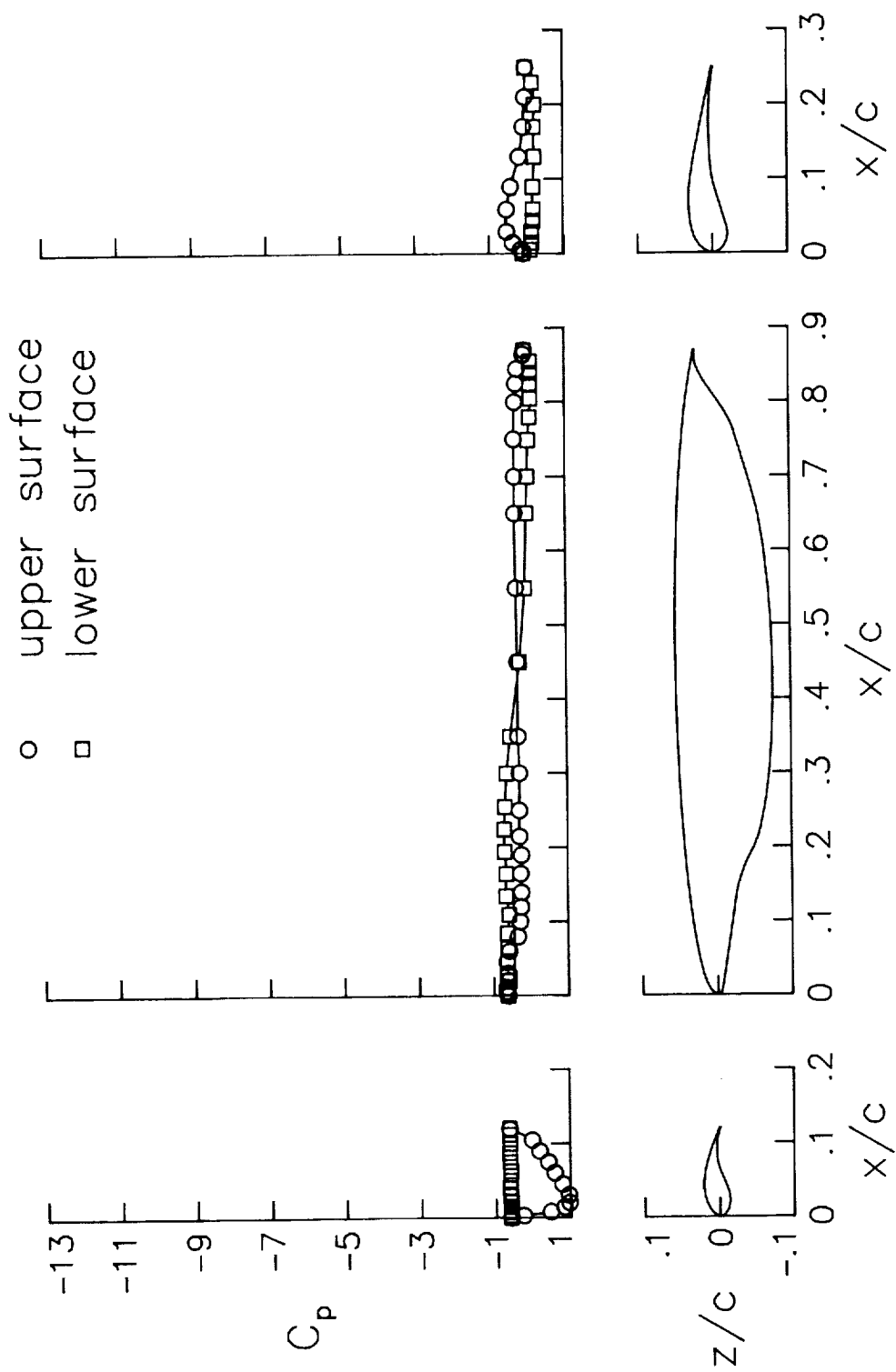
Figure 14. Pressure distributions for 12-percent leading-edge flap configuration. $\delta_{LE} = -55°$; $\delta_{TE} = 15°$; $q_\infty = 30$ psf.

(a) $\alpha = -0.2°$.
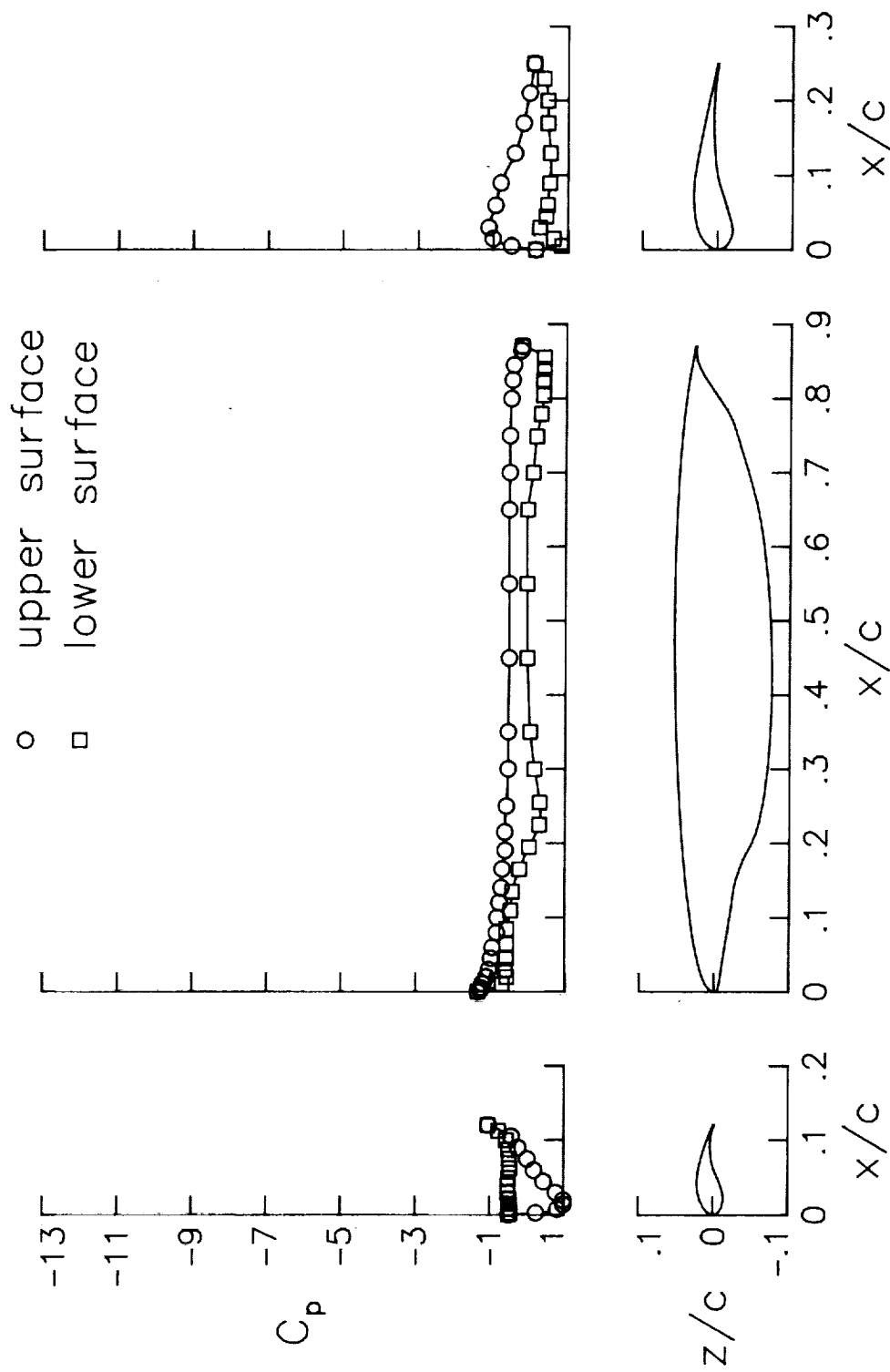
(b) $\alpha = 3.8°$.

Figure 14. Continued.
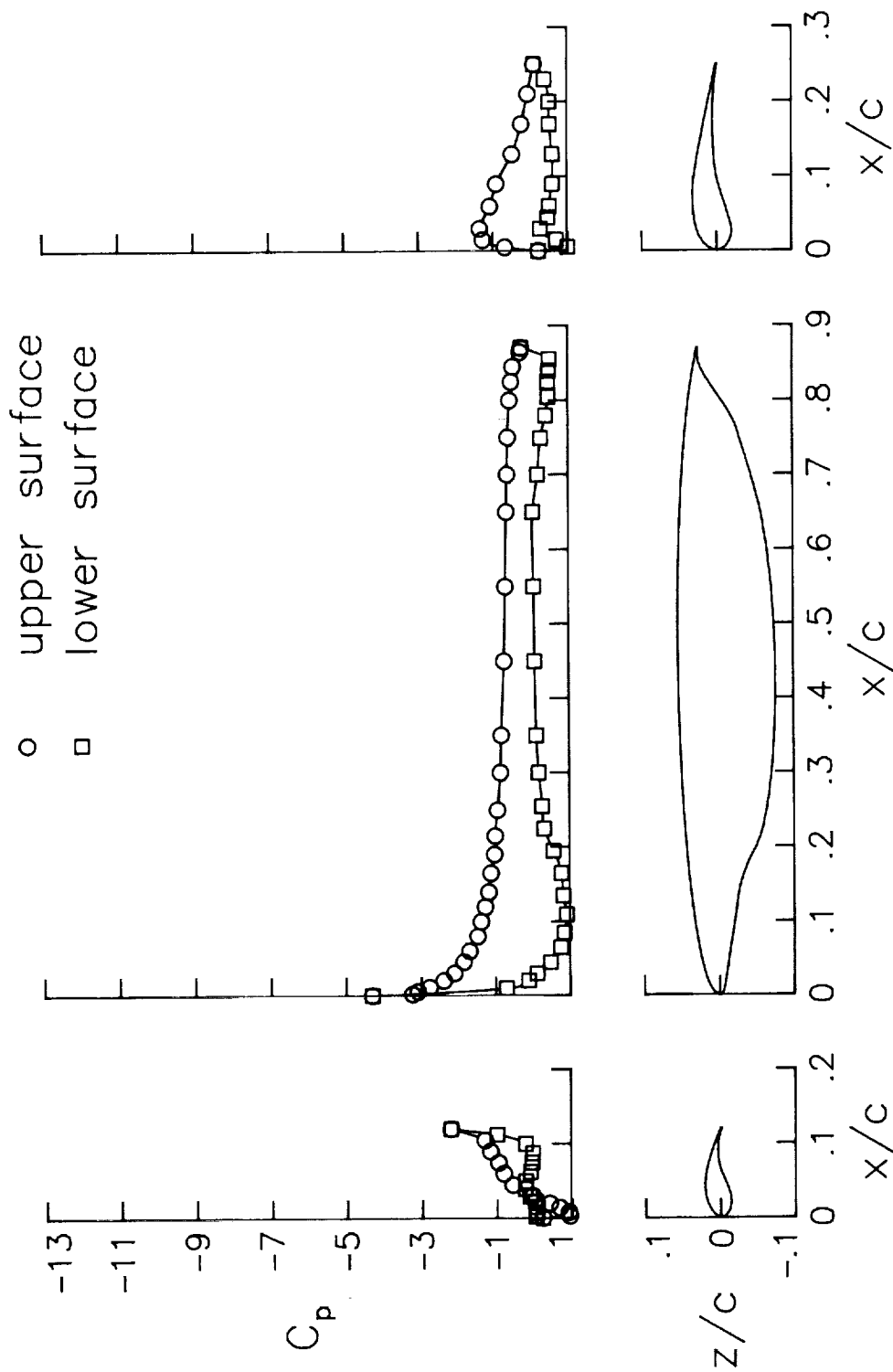
(c) $\alpha = 9.8°$.

Figure 14. Continued.
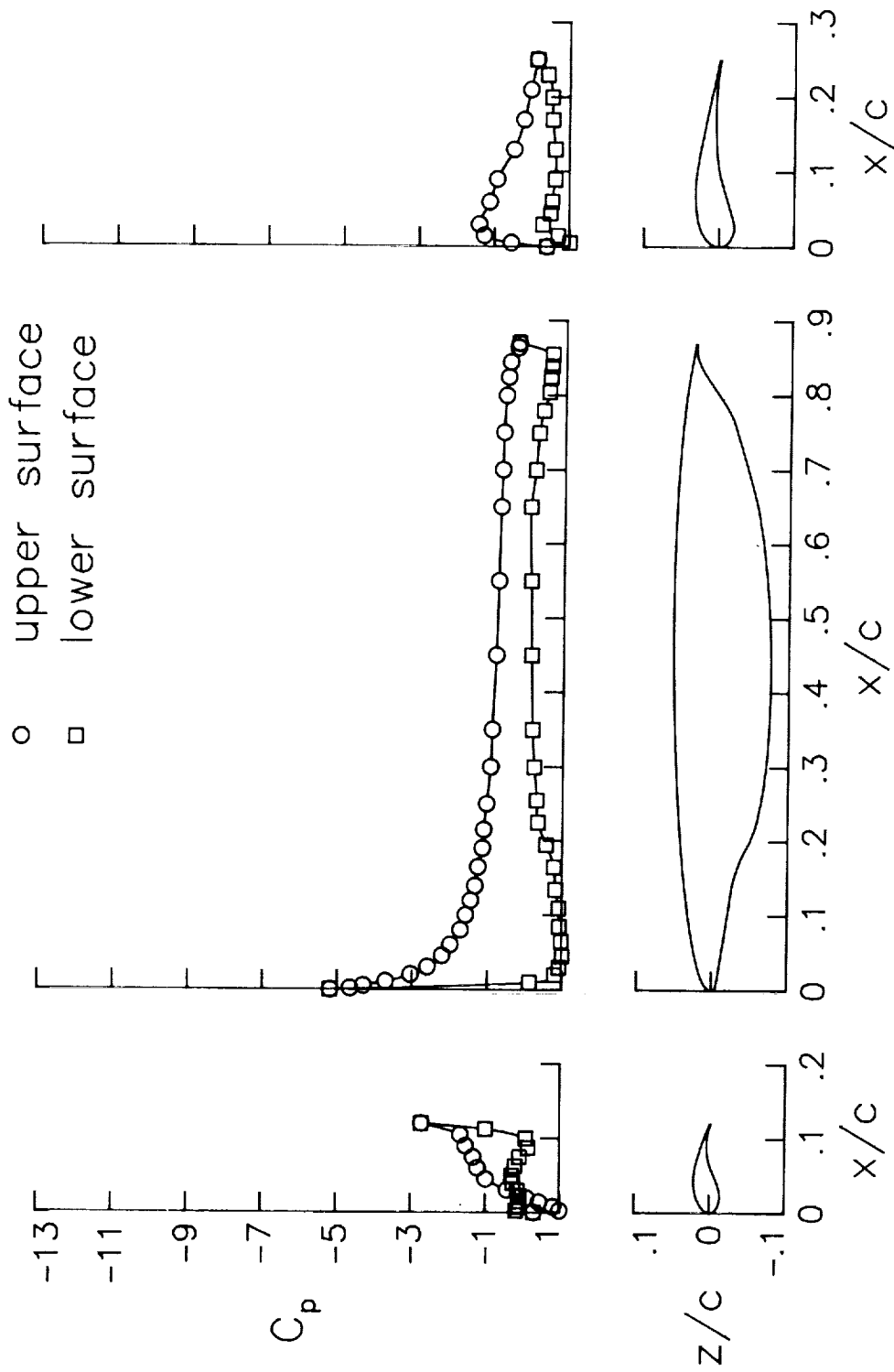
(d) $\alpha = 11.7°$.

Figure 14. Continued.
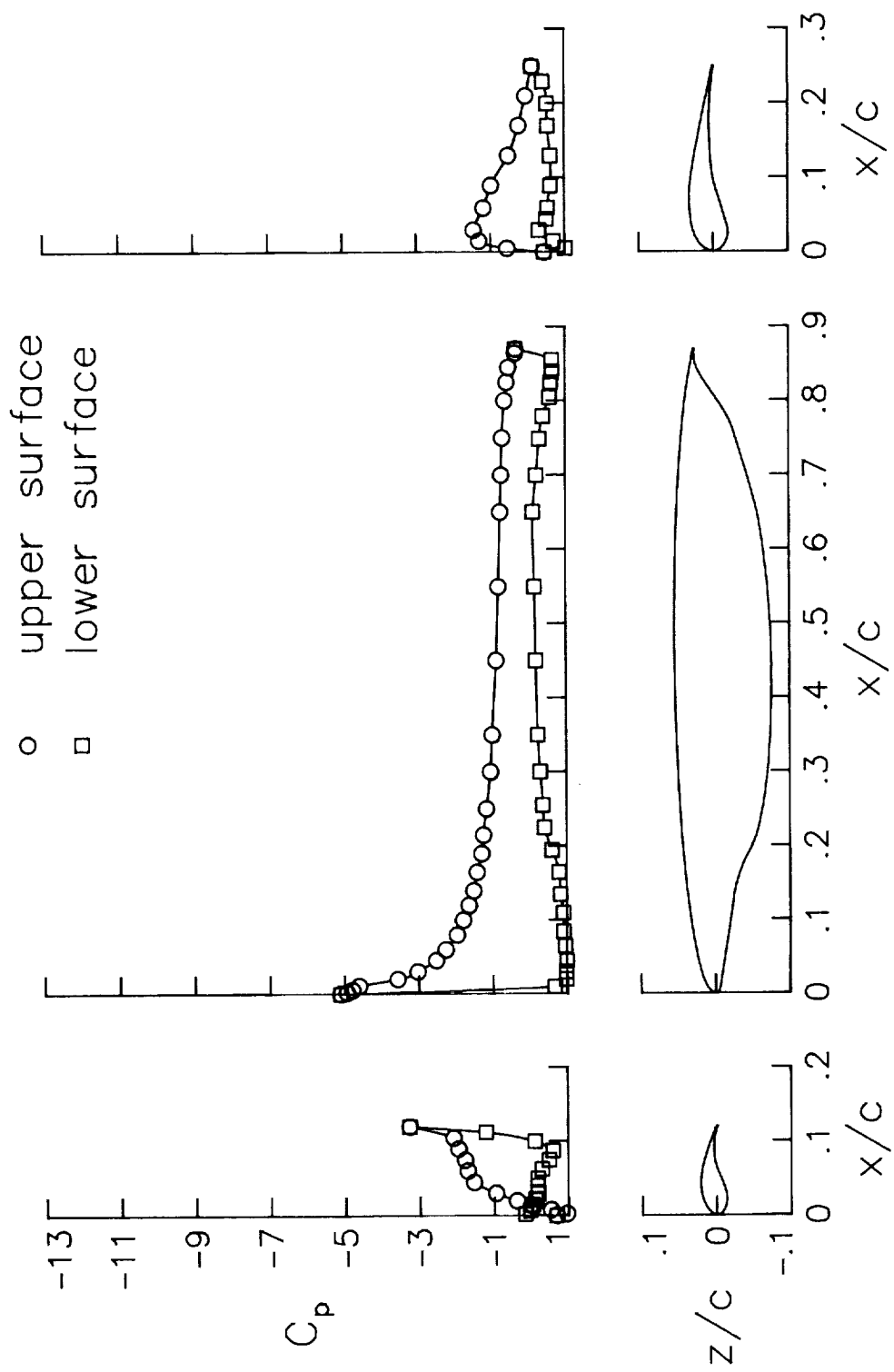
(e) $\alpha = 13.8°$.

Figure 14. Continued.
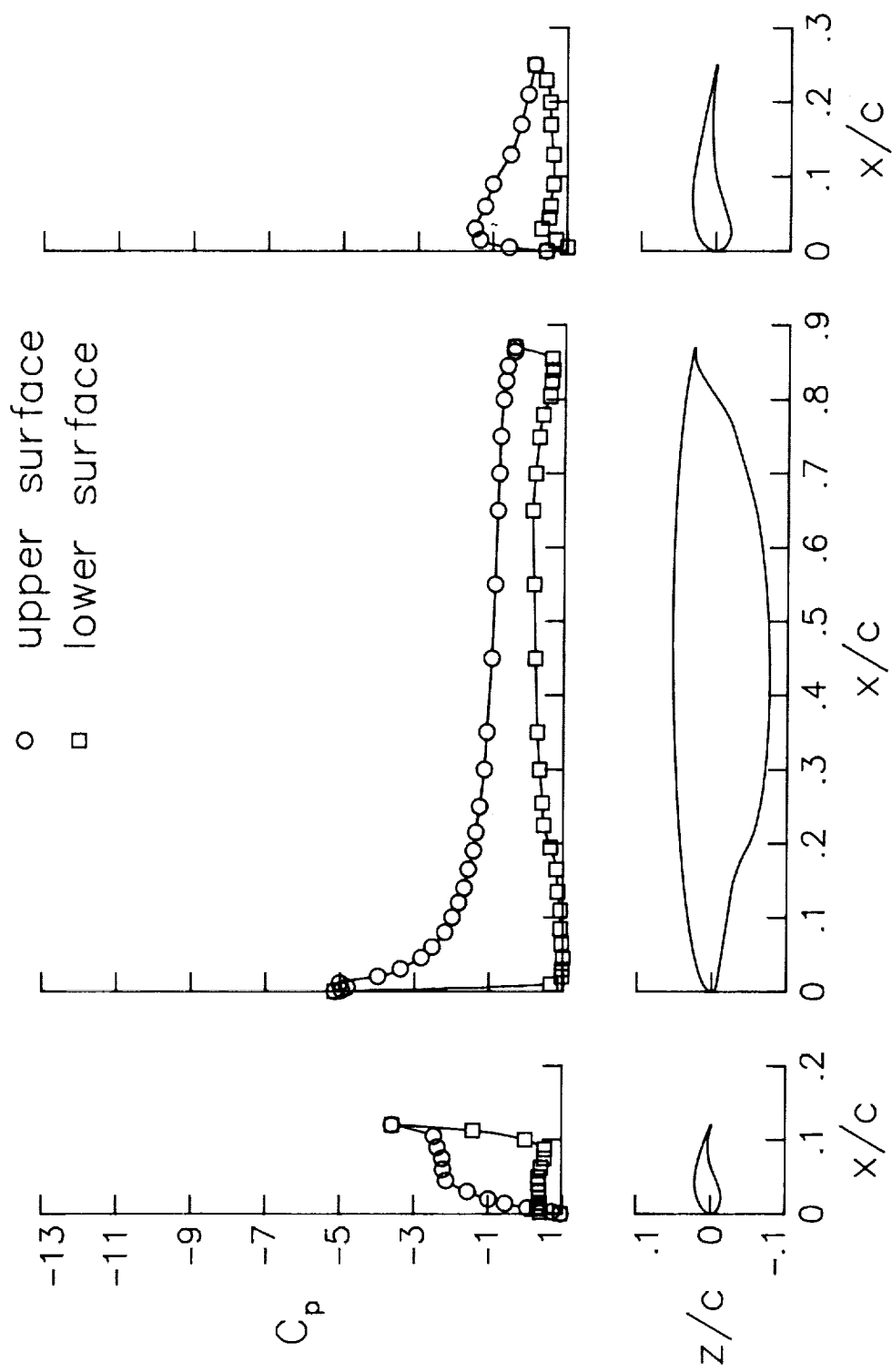
(f) $\alpha = 15.8°$.

Figure 14. Concluded.
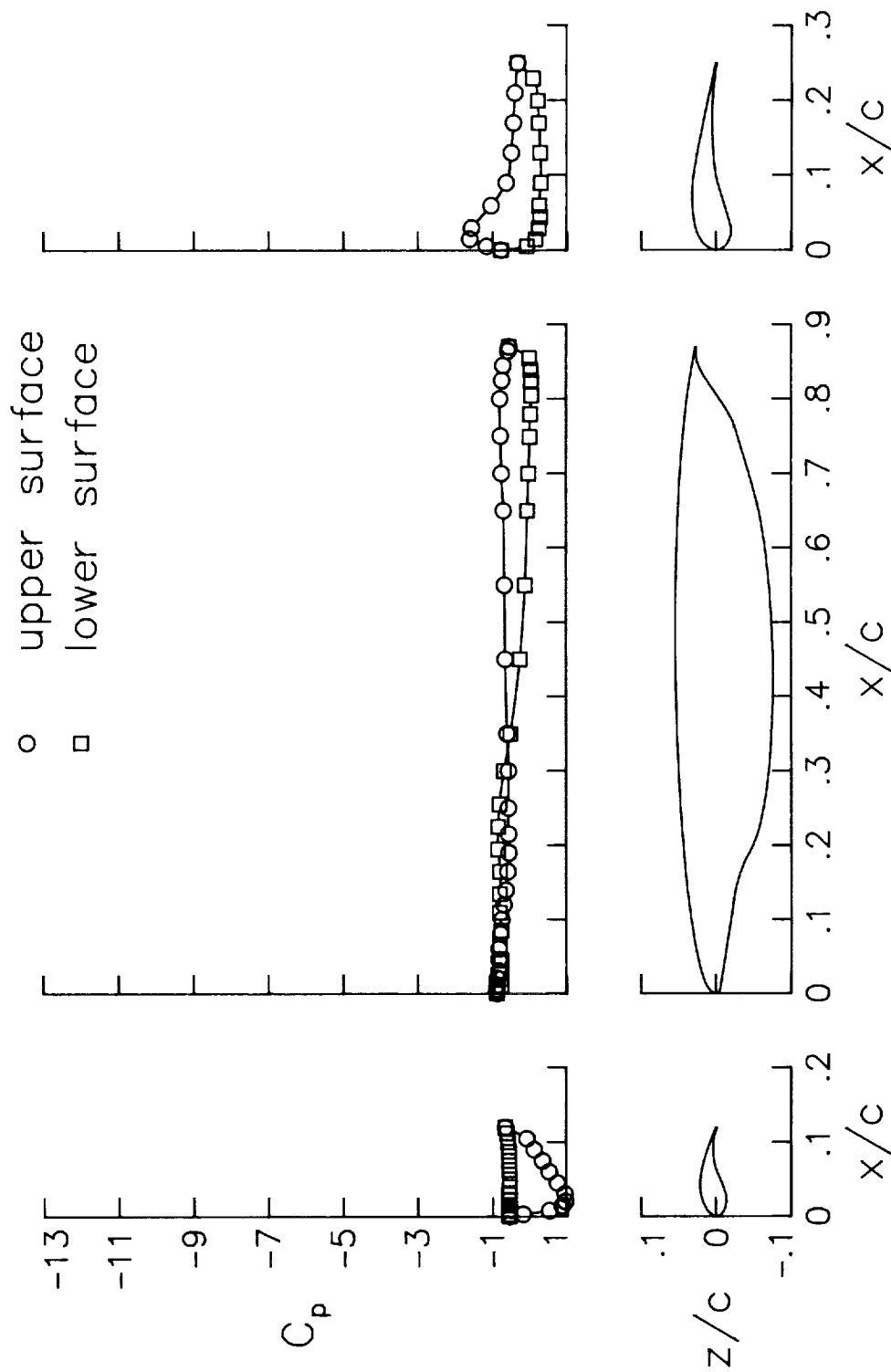
Figure 15. Pressure distributions for 12-percent leading-edge flap configuration. $\delta_{LE} = -55°$; $\delta_{TE} = 30°$; $q_\infty = 30$ psf.

(a) $\alpha = -0.9°$.
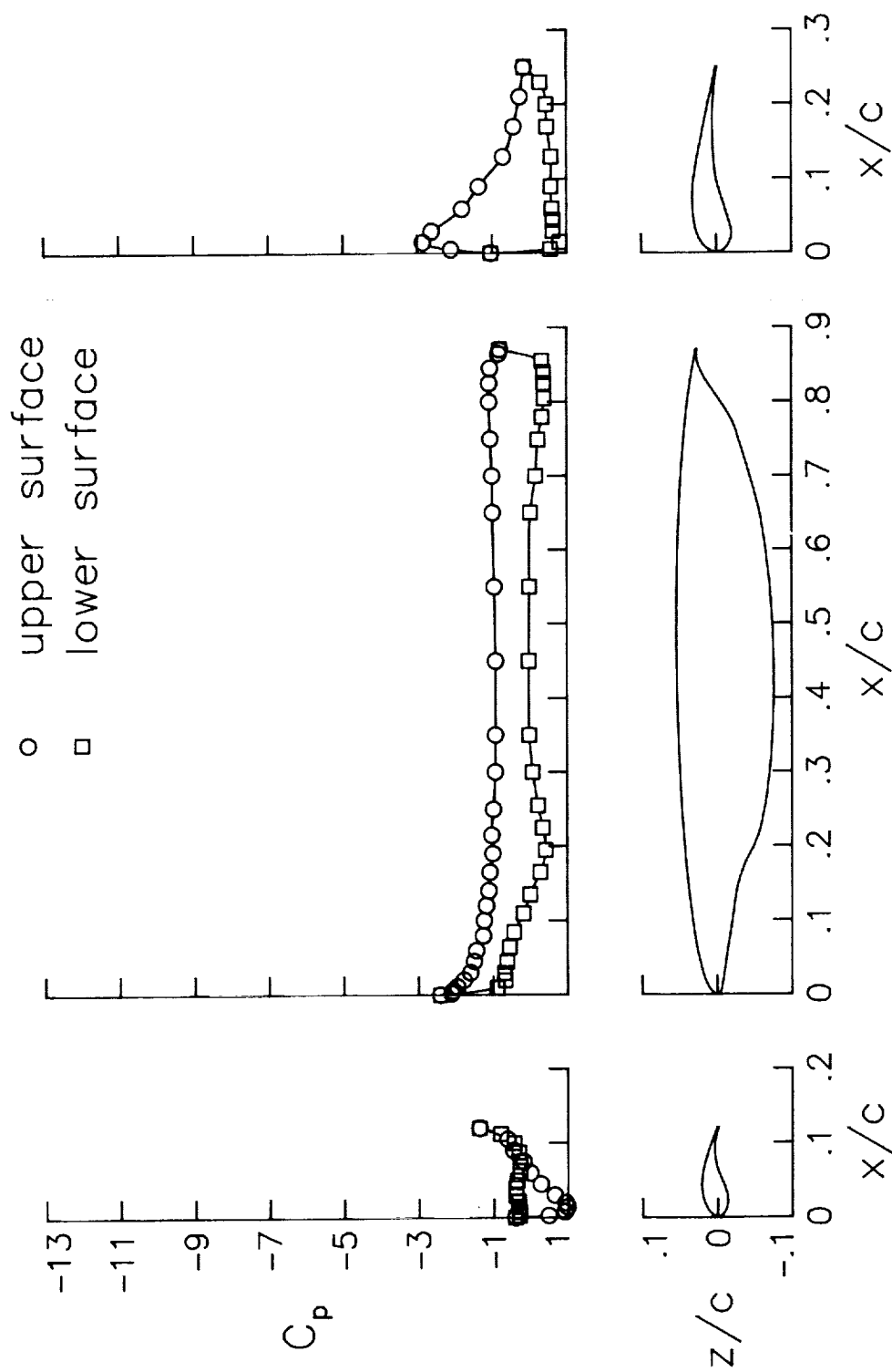
(b) α = 3.3°.

Figure 15. Continued.
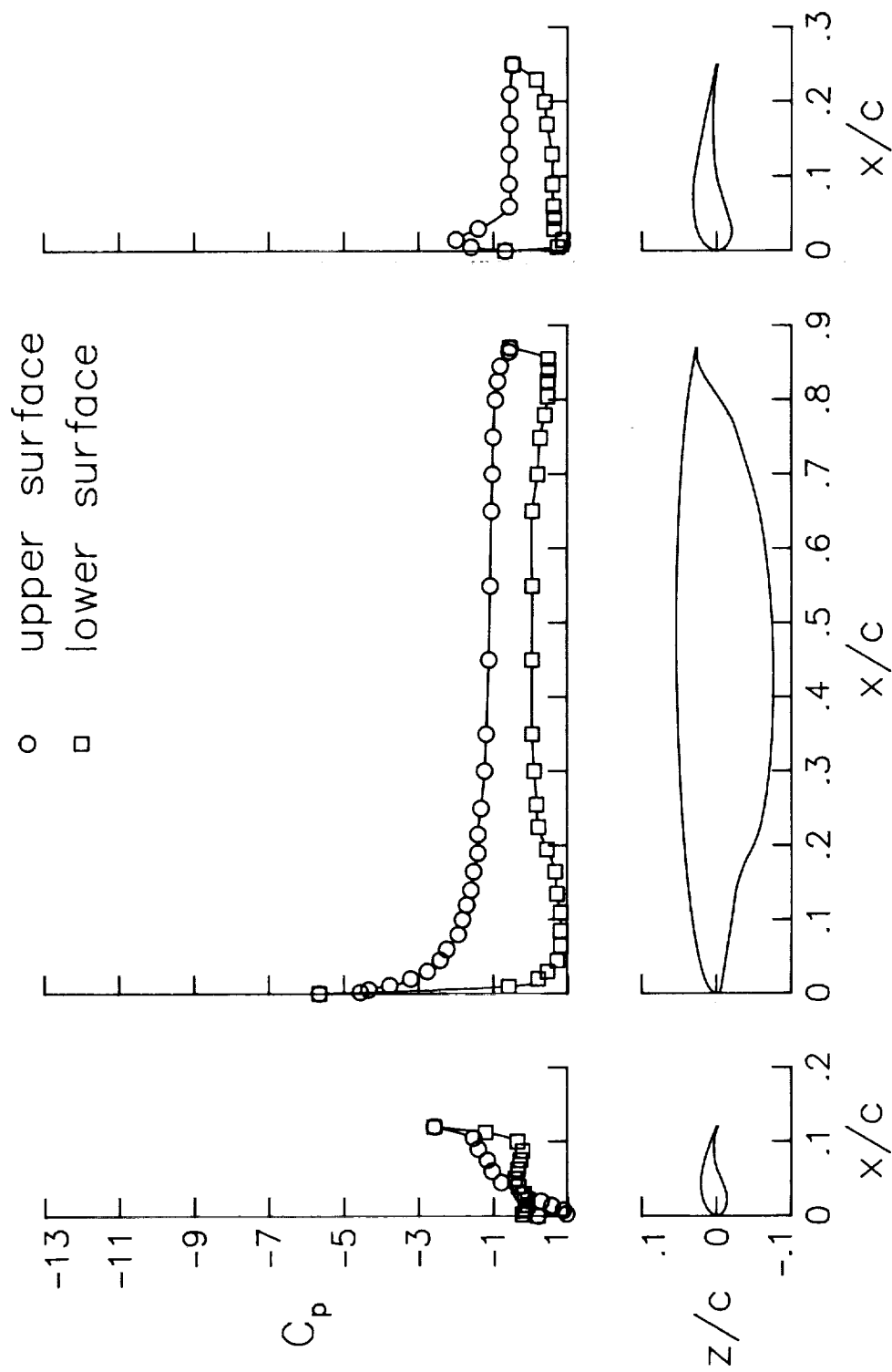
(c) $\alpha = 9.2°$.

Figure 15. Continued.
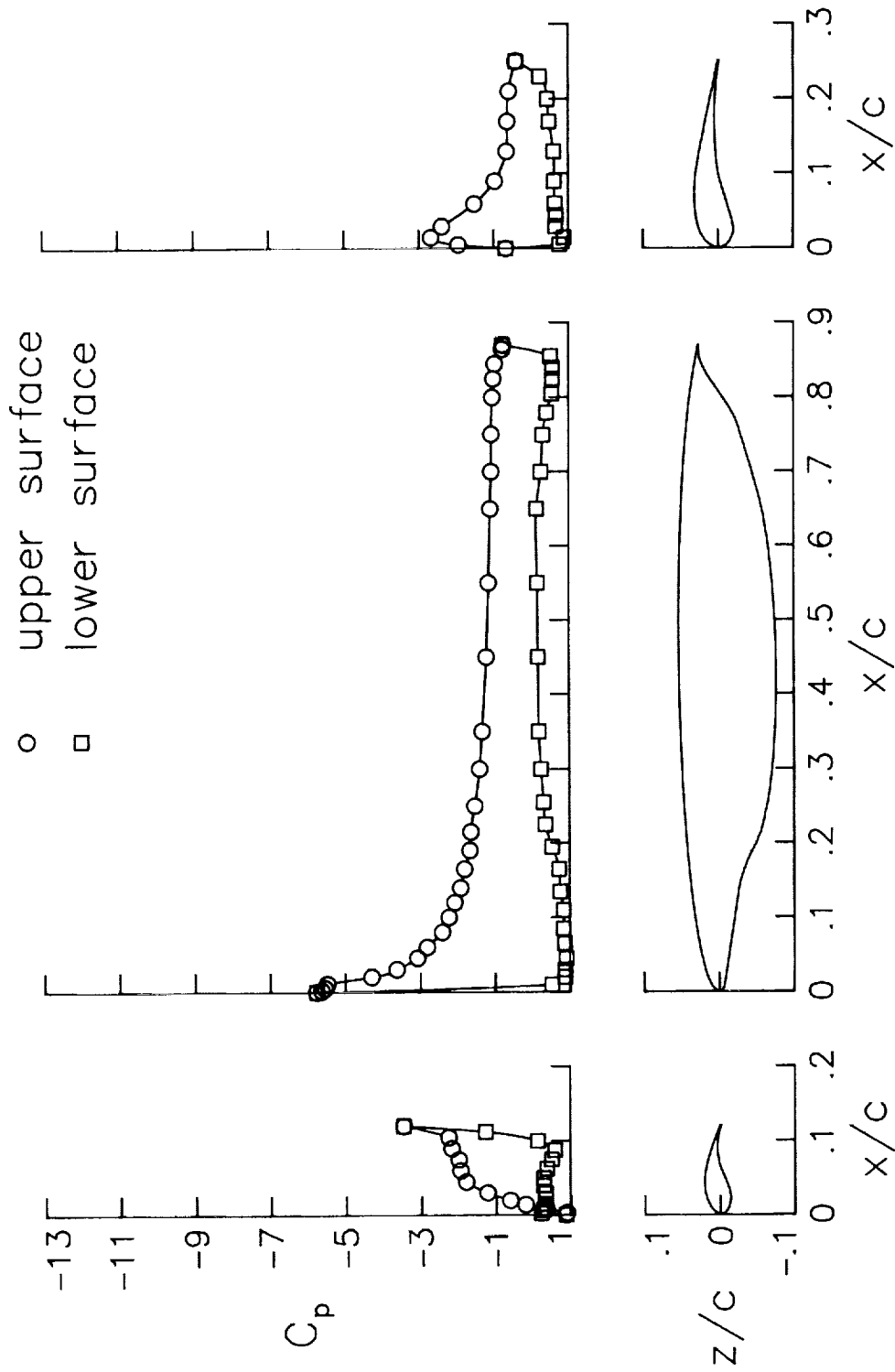
(d) $\alpha = 13.2°$.

Figure 15. Continued.
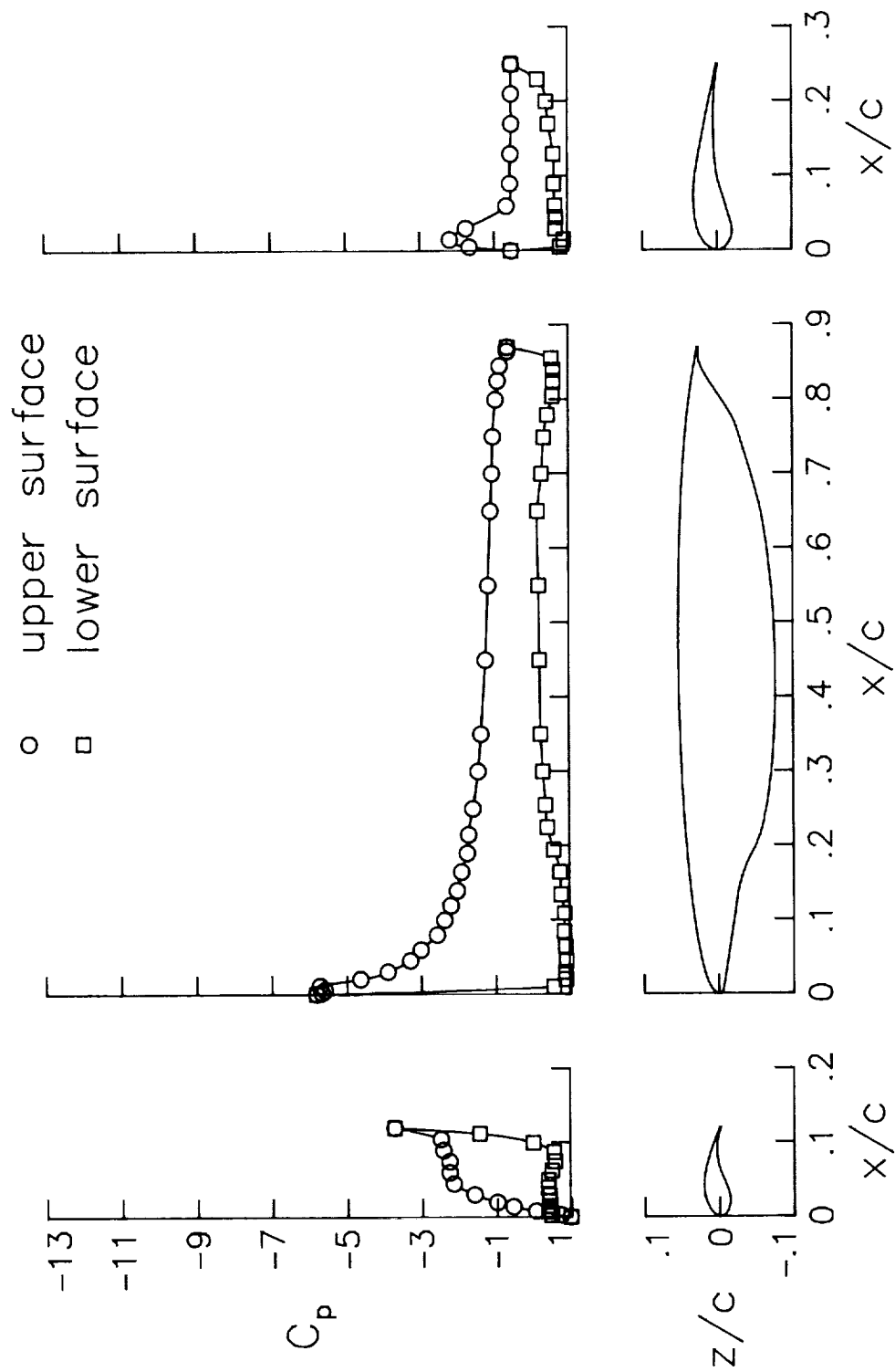
(e) $\alpha = 14.2°$.

Figure 15. Continued.
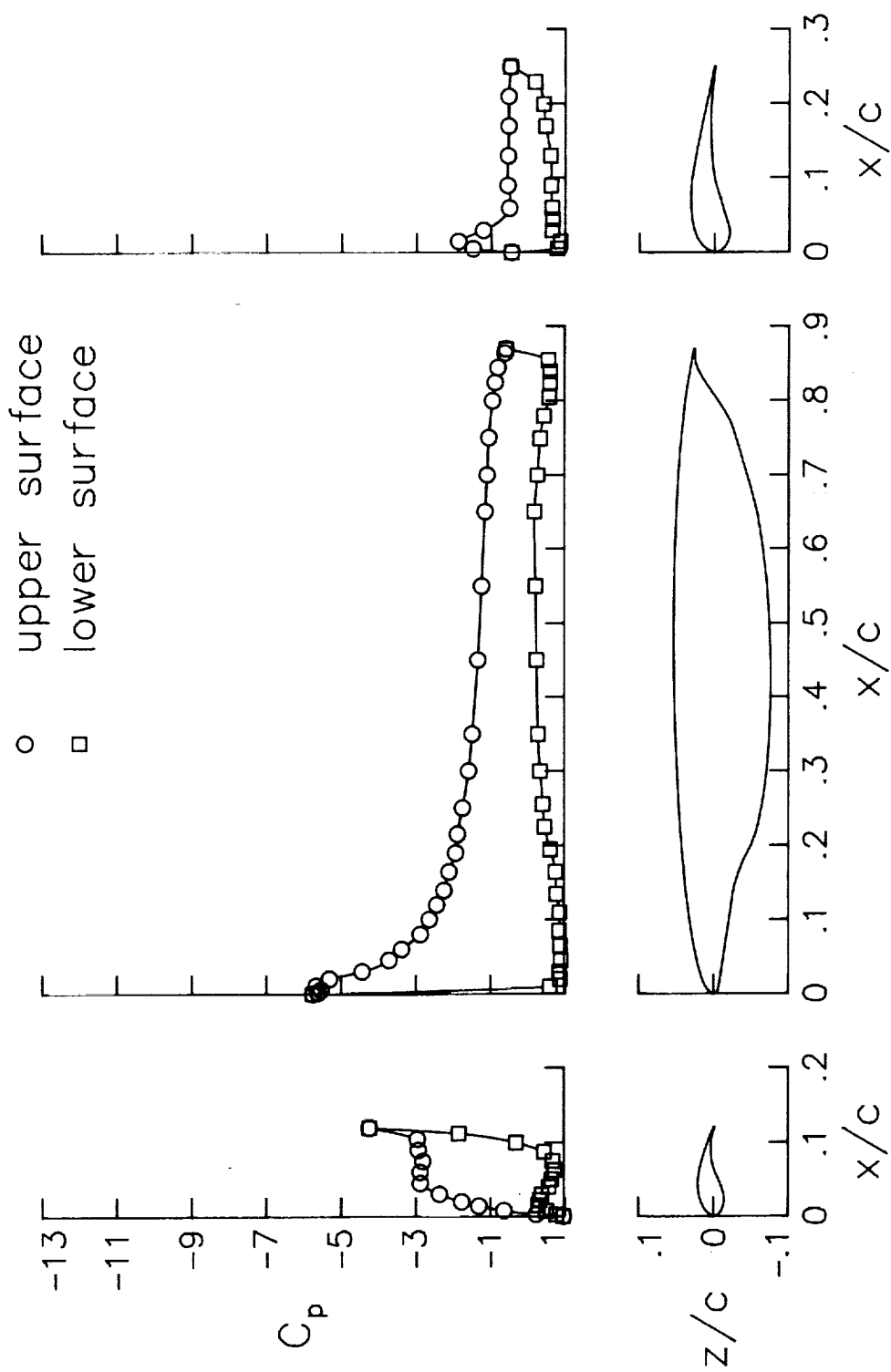
(f) $\alpha = 16.3°$.

Figure 15. Concluded.
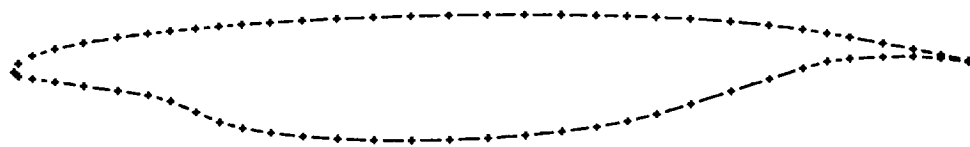
(a) MCARF segment model.

(b) End view of VSAERO panel model.
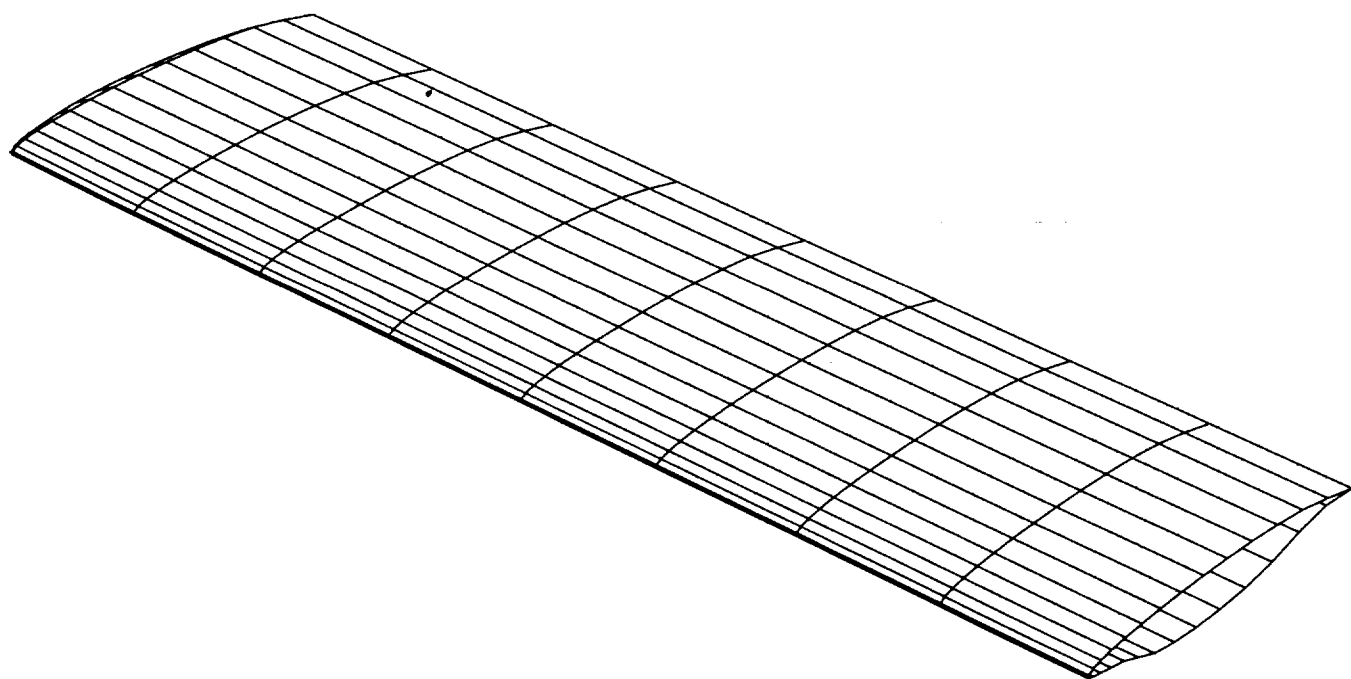
(c) Perspective view of VSAERO panel model.

Figure 16. Sketch of computational models used to predict aerodynamic characteristics.
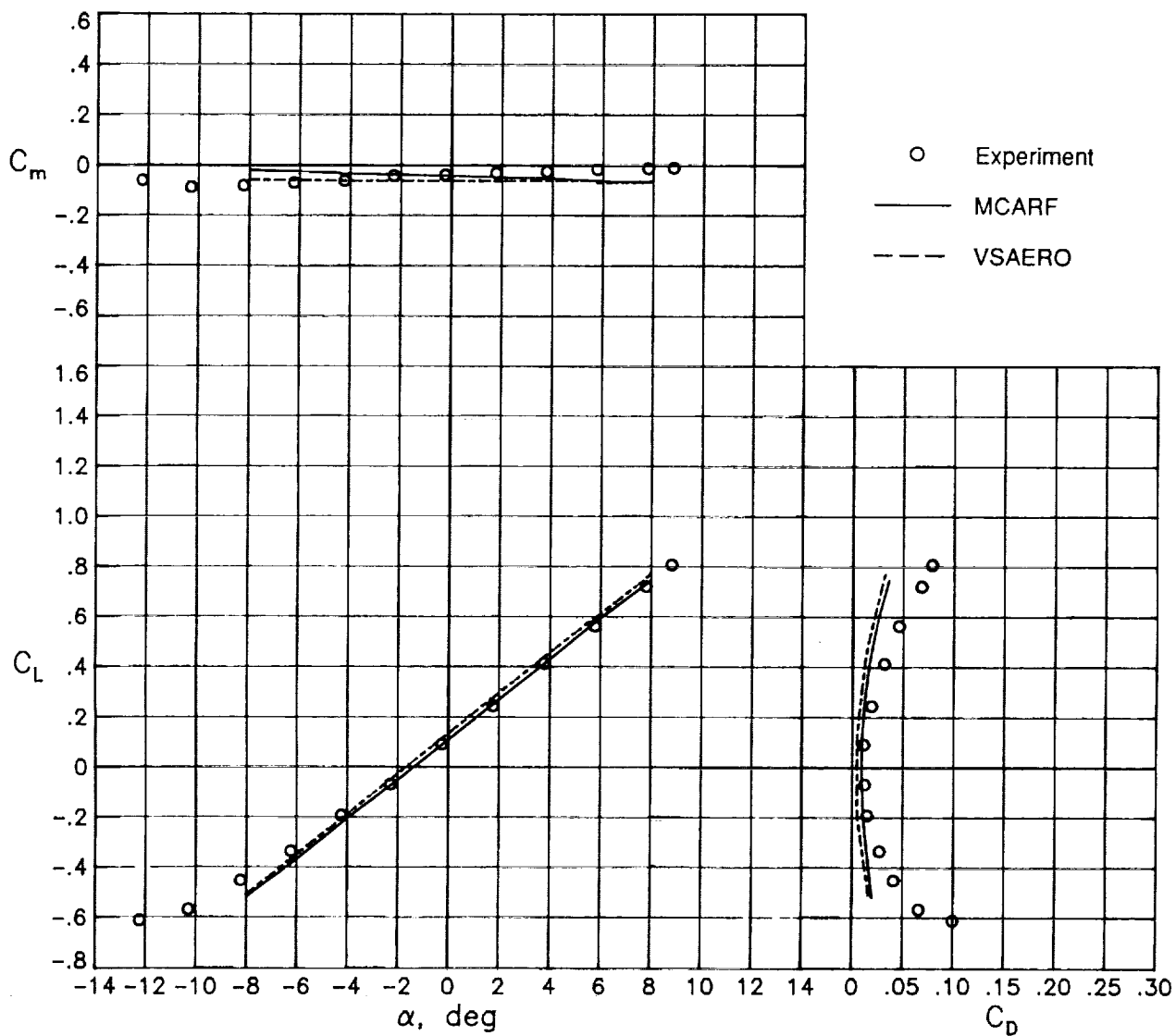
Figure 17. Predicted and measured longitudinal aerodynamic characteristics for cruise configuration. $q_\infty = 30$ psf.
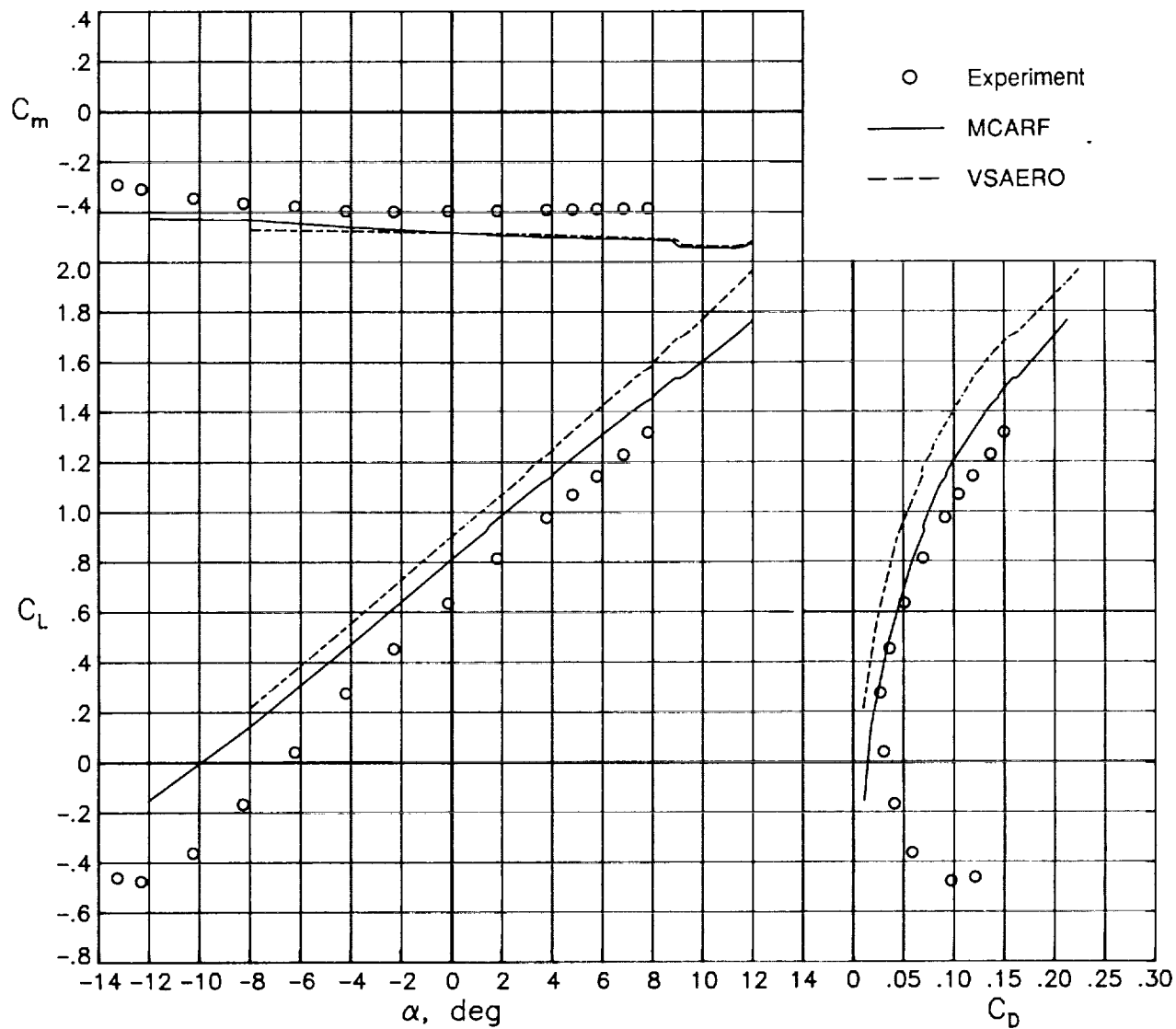
Figure 18. Predicted and measured longitudinal aerodynamic characteristics for trailing-edge flap configuration. $\delta_{TE} = 15°$; $q_\infty = 30$ psf.
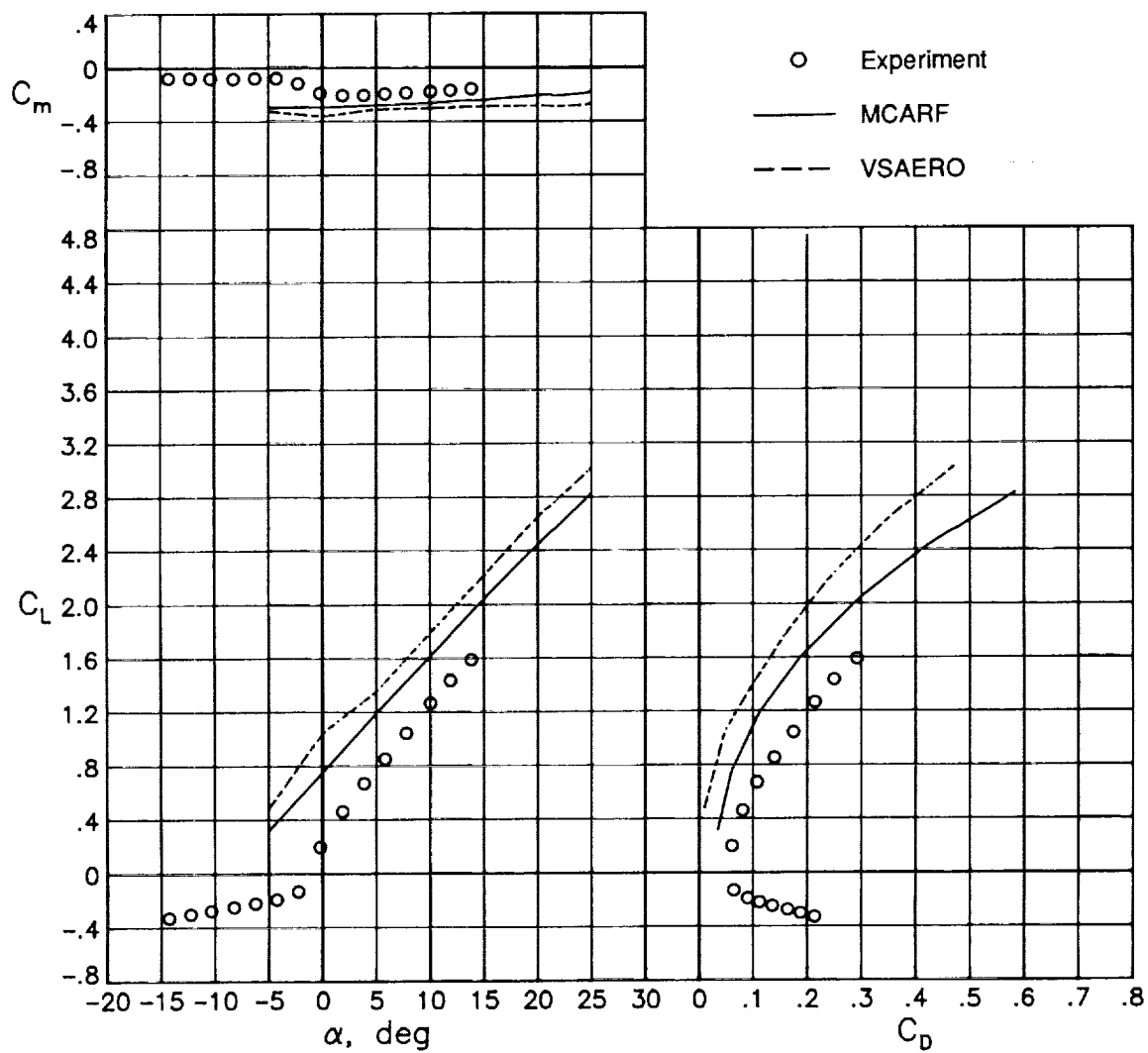
(a) $\delta_{TE} = 15°$.

Figure 19. Predicted and measured longitudinal aerodynamic characteristics for 10-percent leading-edge flap configuration. $\delta_{LE} = -55°$; $q_\infty = 30$ psf.
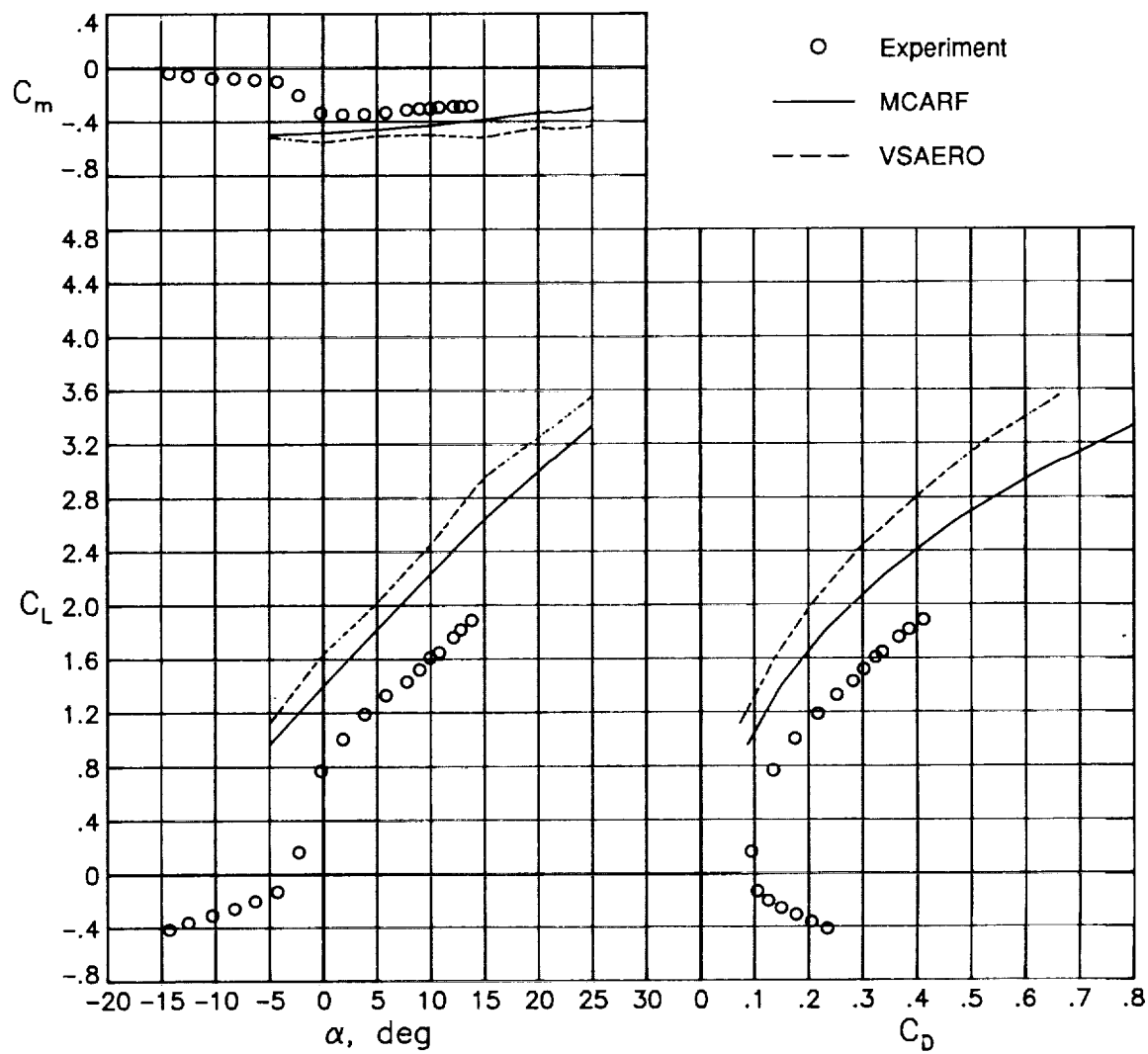
(b) $\delta_{TE} = 30°$.

Figure 19. Concluded.
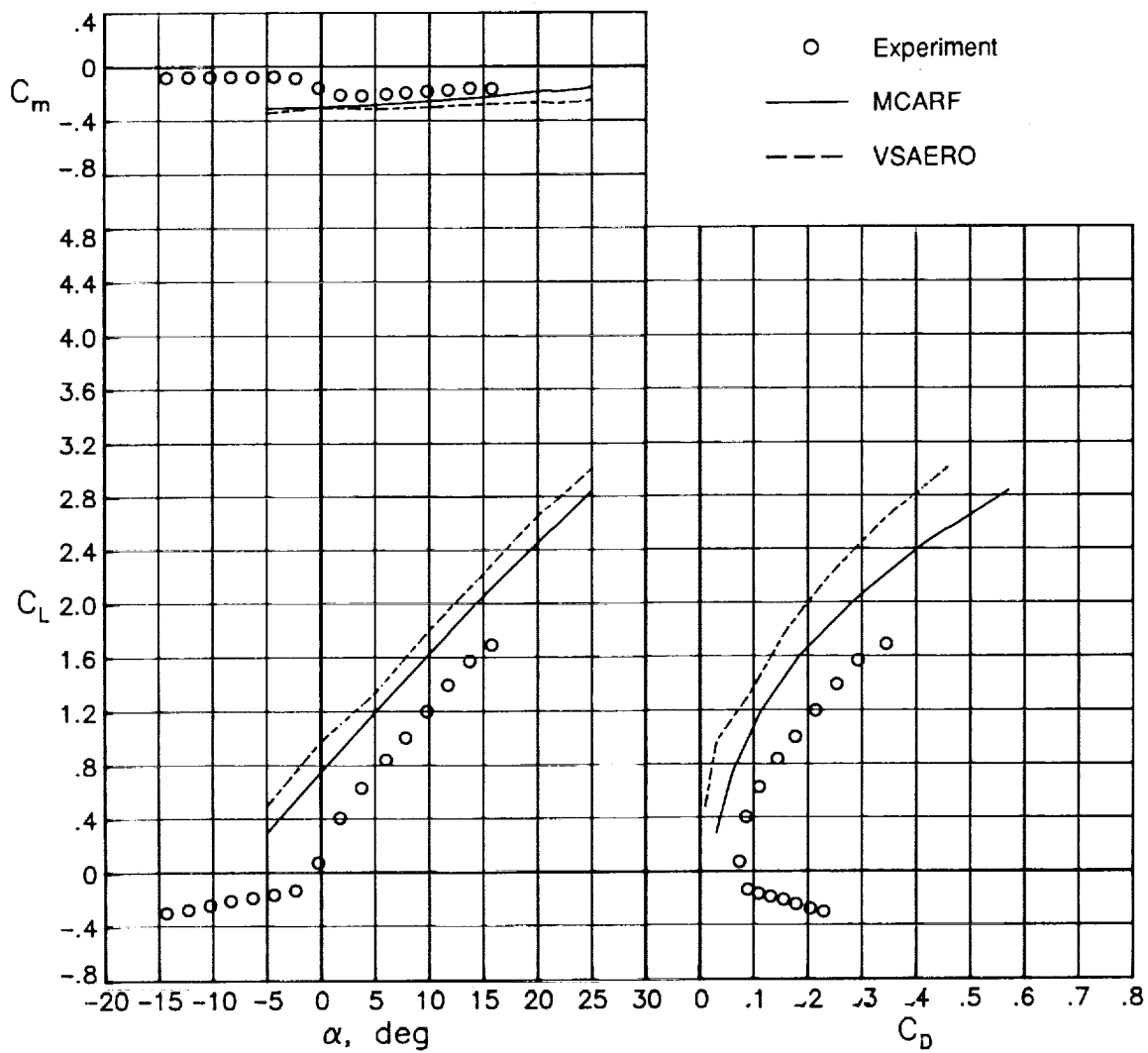
(a) $\delta_{TE} = 15°$.

Figure 20. Predicted and measured longitudinal aerodynamic characteristics for 12-percent leading-edge flap configuration. $\delta_{LE} = -55°$; $q_\infty = 30$ psf.
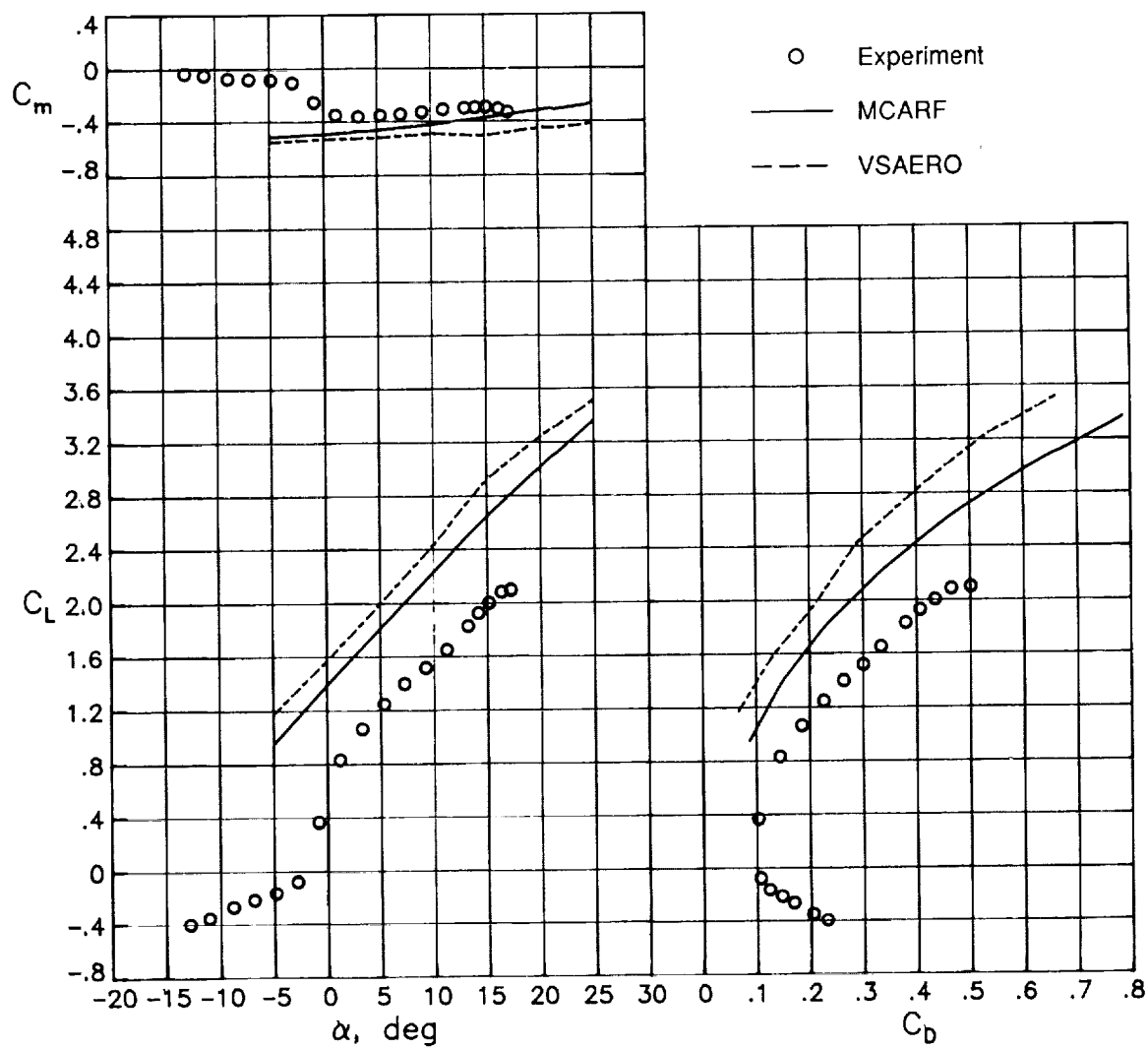
(b) $\delta_{TE} = 30°$.
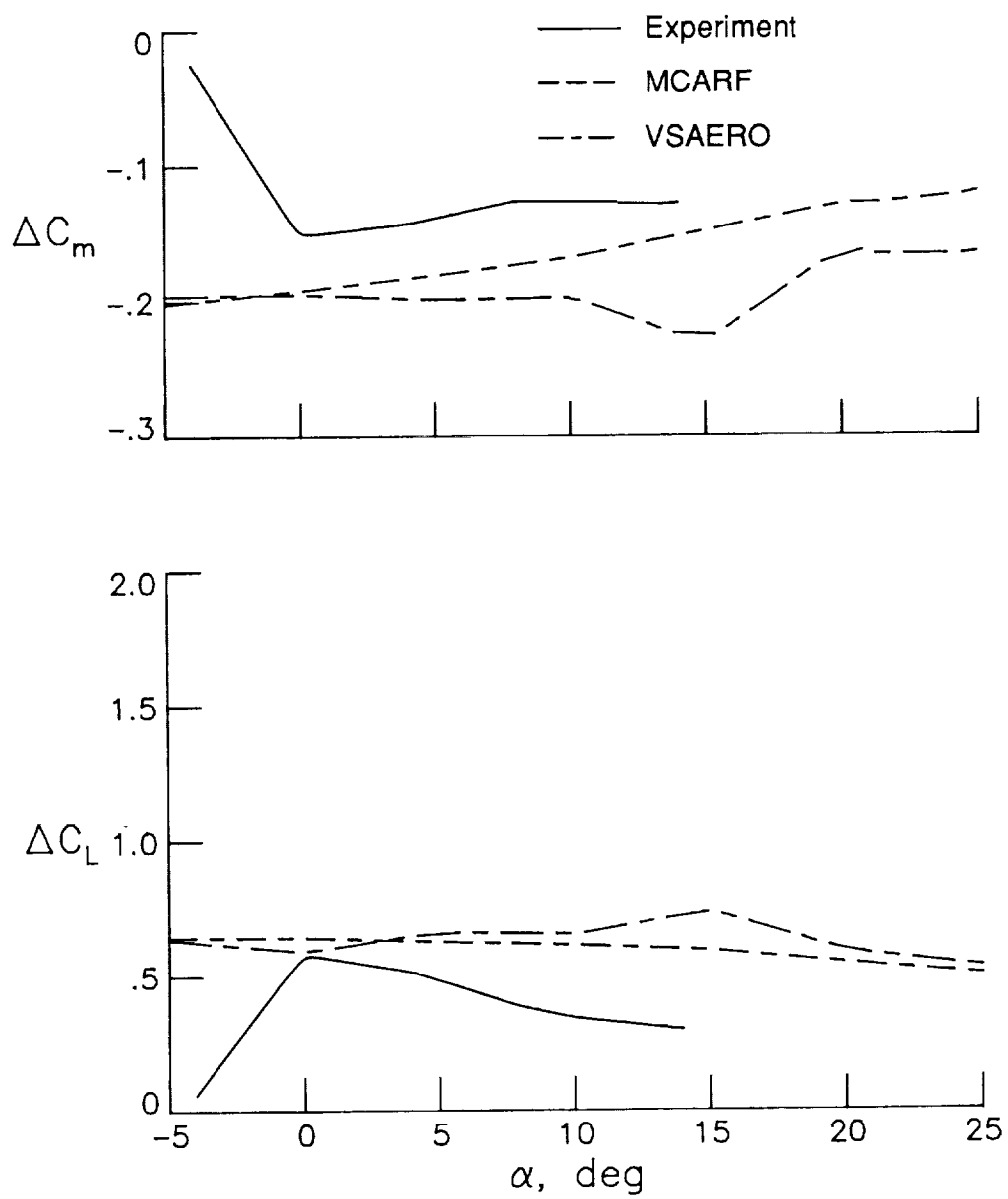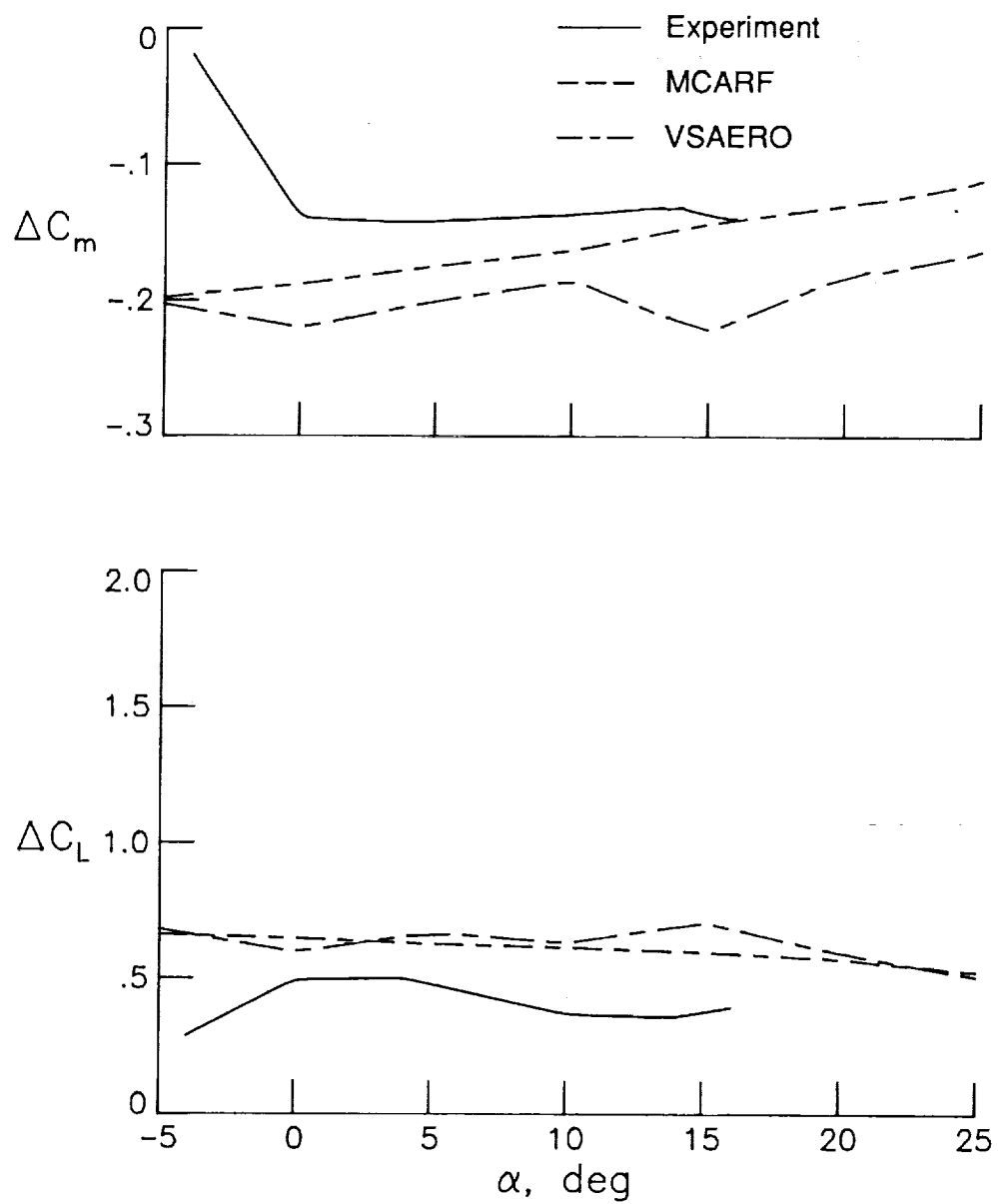
Figure 20. Concluded.

.13

.12

.11

.10

.09

C_{L_α} .07

.06

.05

.04

.03

.02

.01

0

Experiment   MCARF   VSAERO
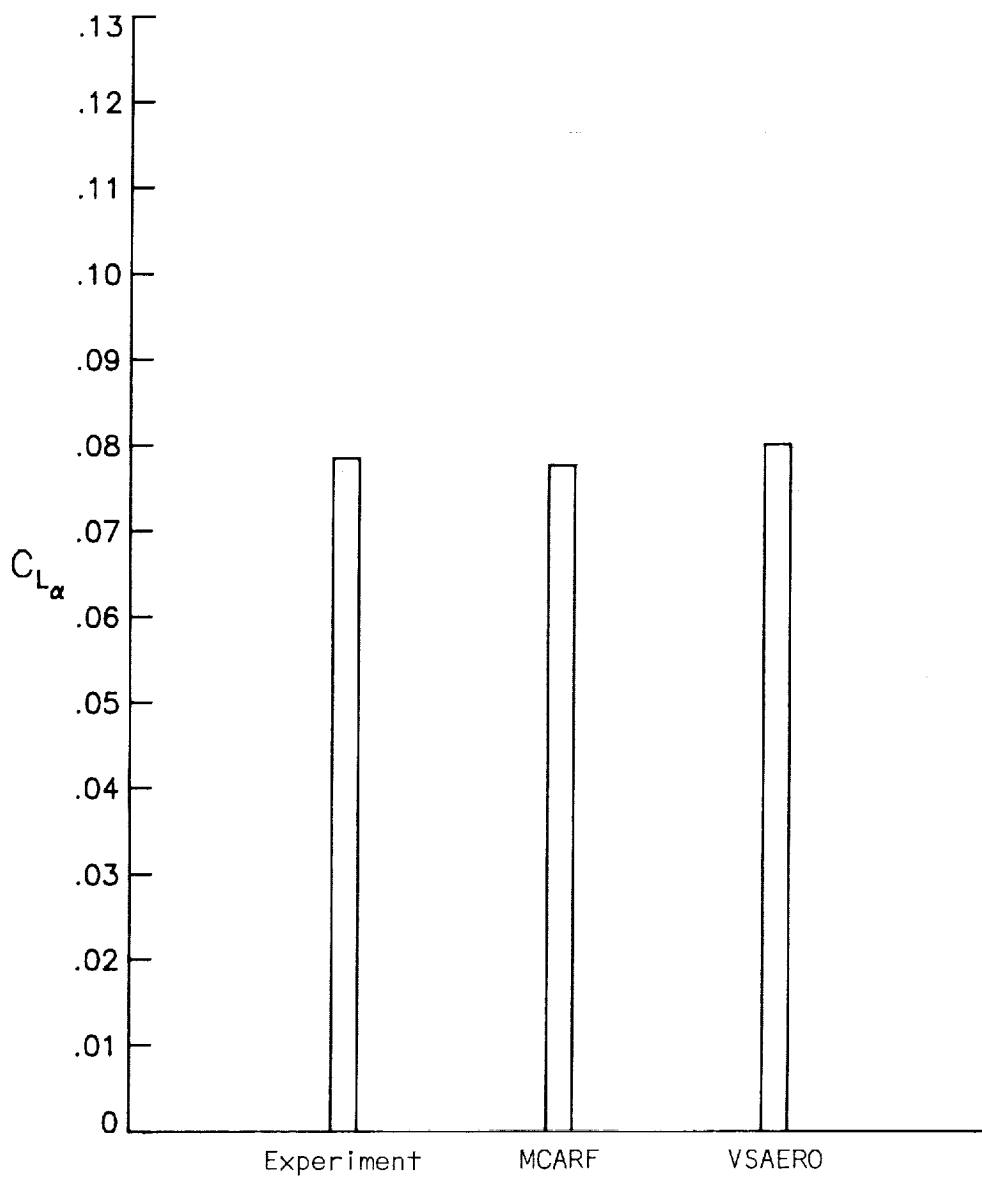
Figure 21. Predicted and measured lift-curve slopes for cruise configuration.
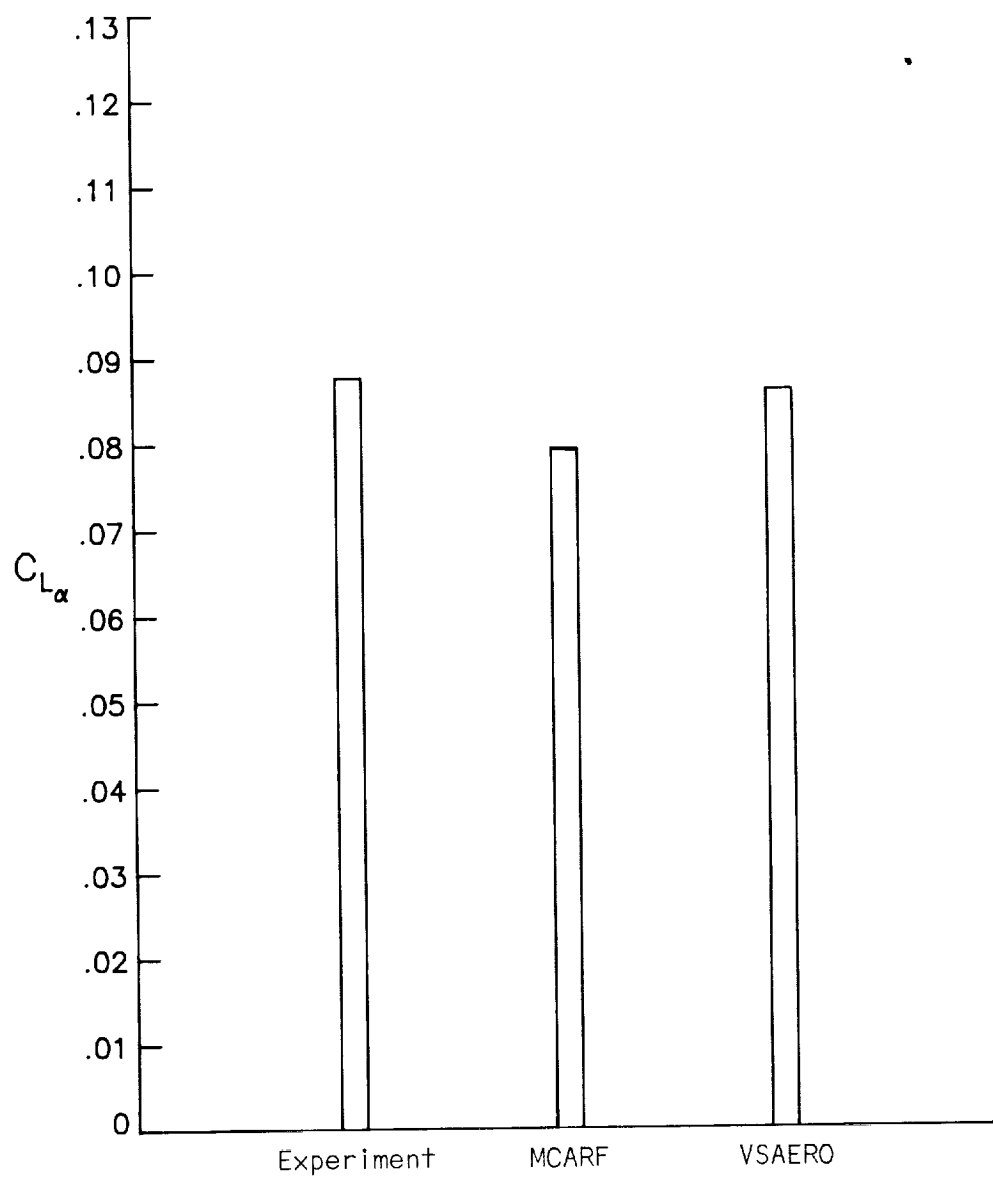
Figure 22. Predicted and measured lift-curve slopes for trailing-edge flap configuration. $\delta_{TE} = 15°$.
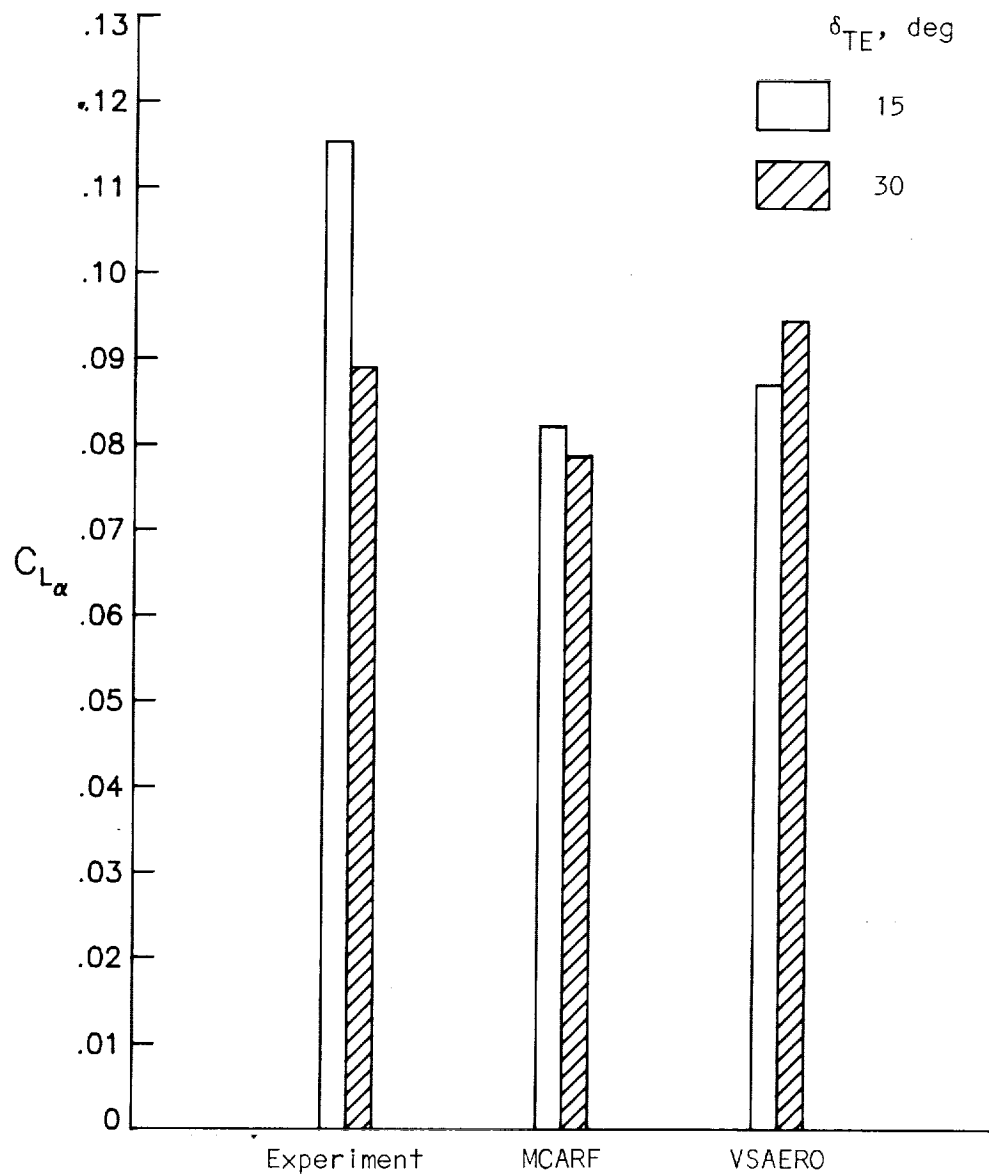
Figure 23. Predicted and measured lift-curve slopes for 10-percent leading-edge flap configuration. $\delta_{LE} = -55°$.
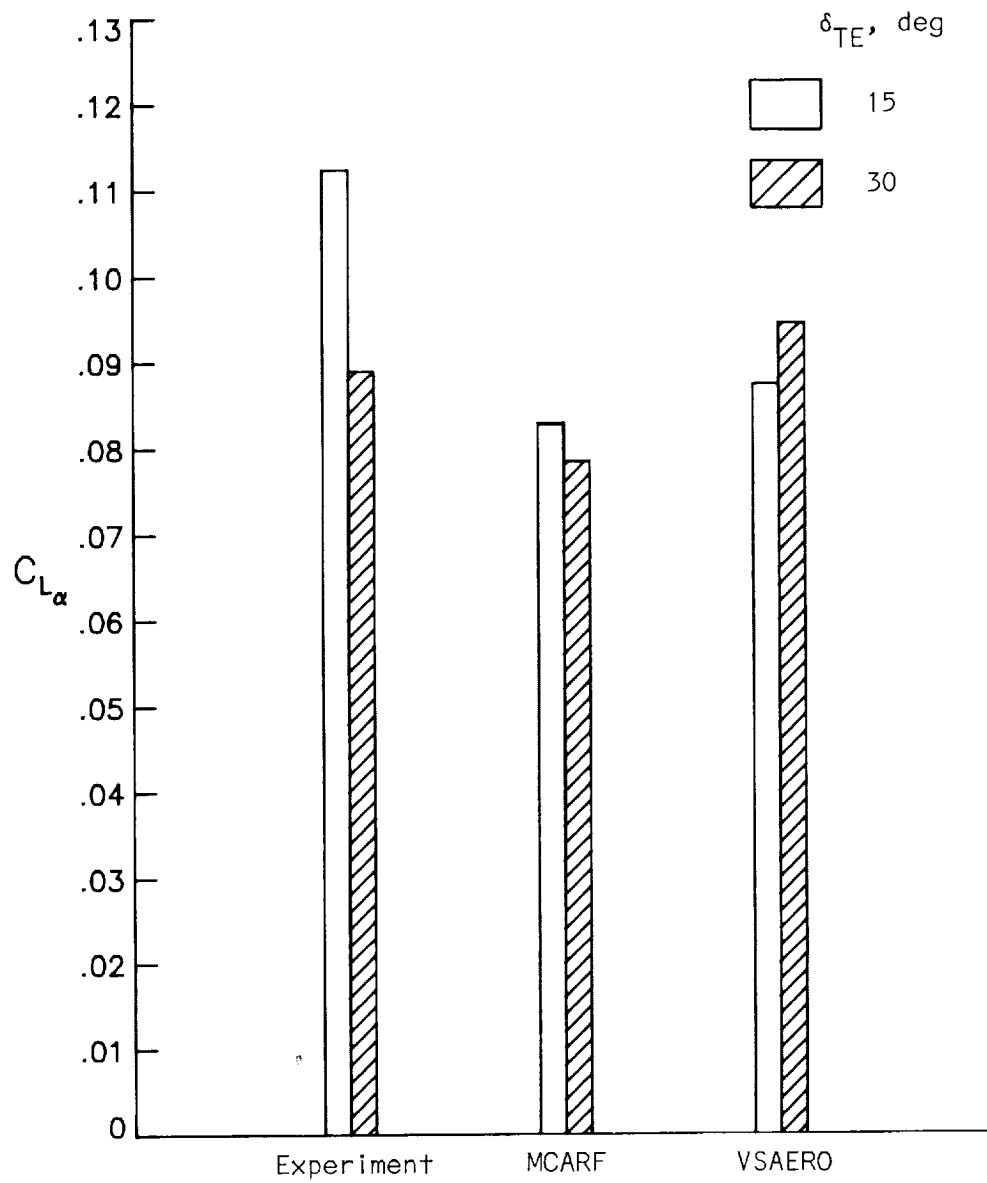
Figure 24. Predicted and measured lift-curve slopes for 12-percent leading-edge flap configuration. $\delta_{LE} = -55°$.
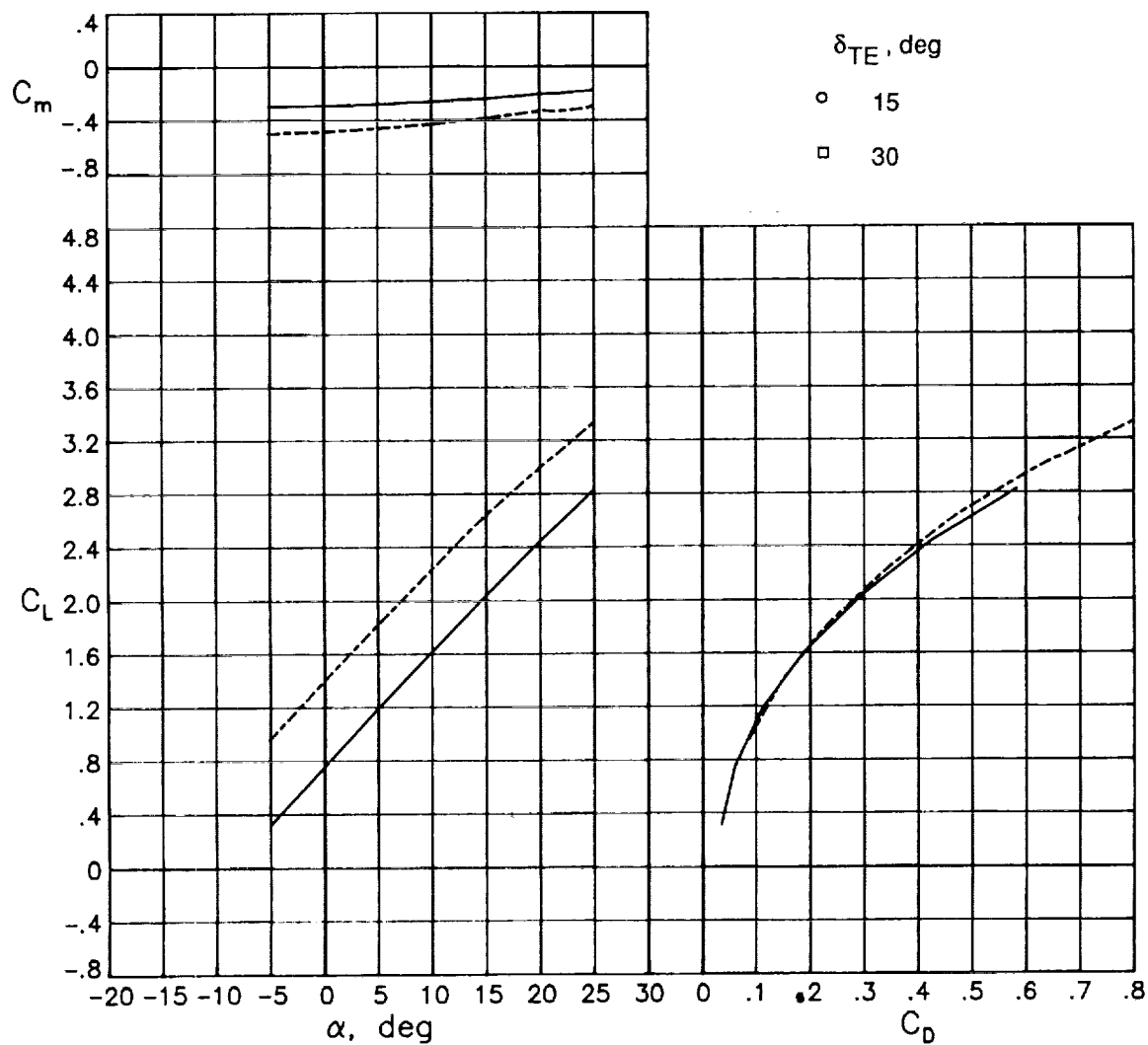
(a) MCARF prediction.

Figure 25. Prediction of effect of trailing-edge flap deflection on longitudinal aerodynamic characteristics for 10-percent leading-edge flap configuration. $\delta_{LE} = -55°$; $q_\infty = 30$ psf.

C-2
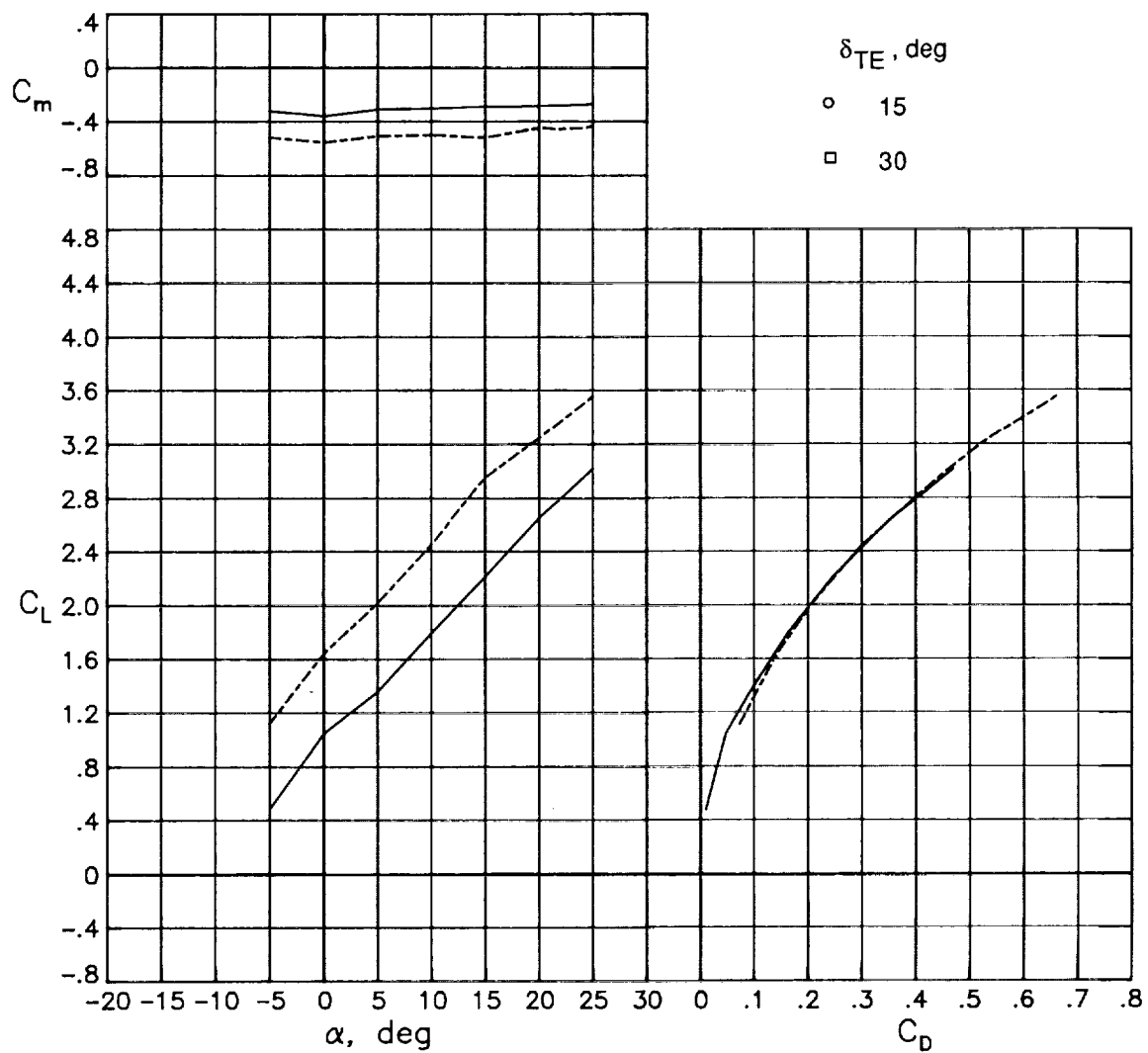
(b) VSAERO prediction.

Figure 25. Concluded.
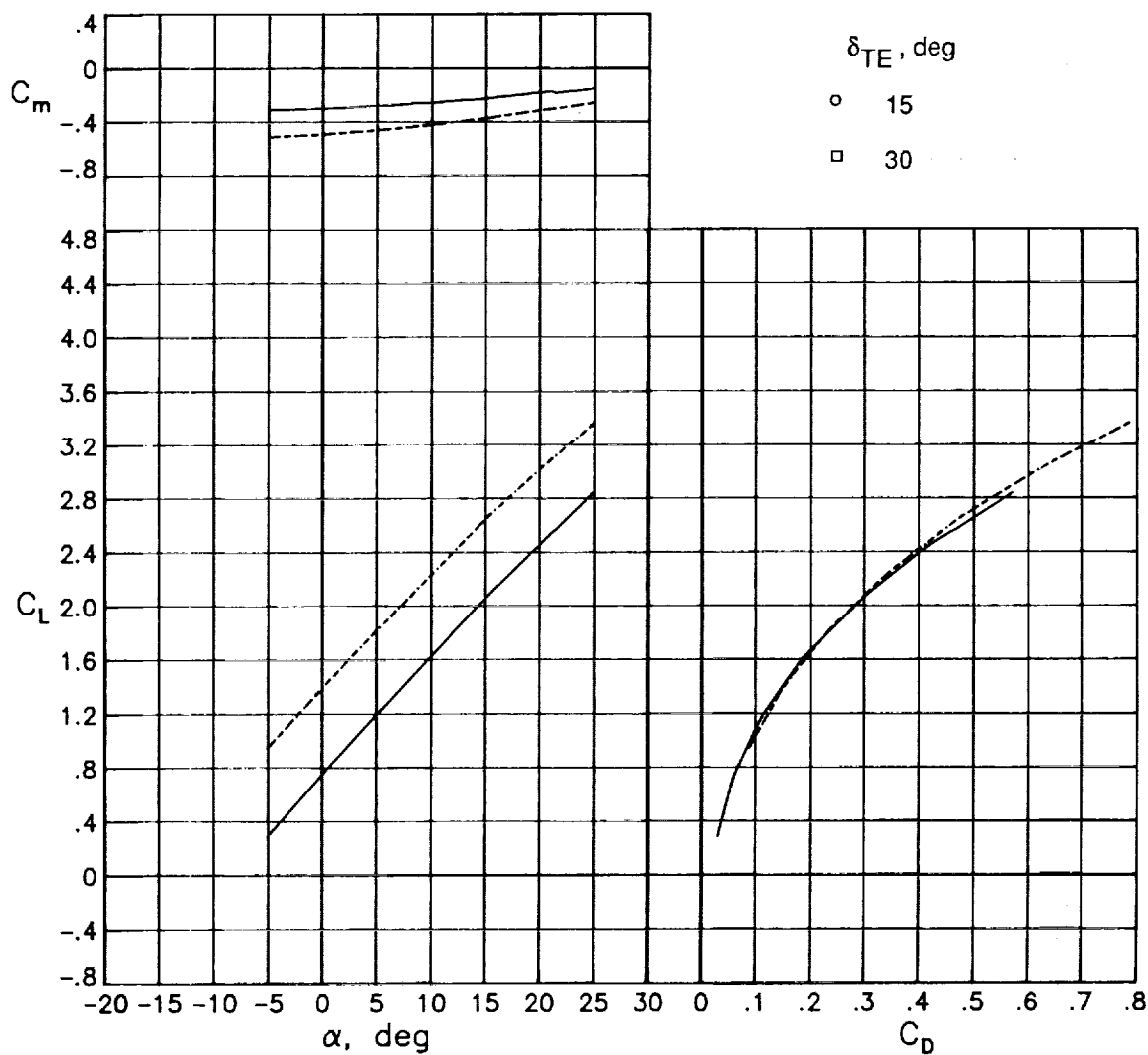
(a) MCARF prediction.

Figure 26. Prediction of effect of trailing-edge flap deflection on longitudinal aerodynamic characteristics for 12-percent leading-edge flap configuration. $\delta_{LE} = -55°$; $q_\infty = 30$ psf.
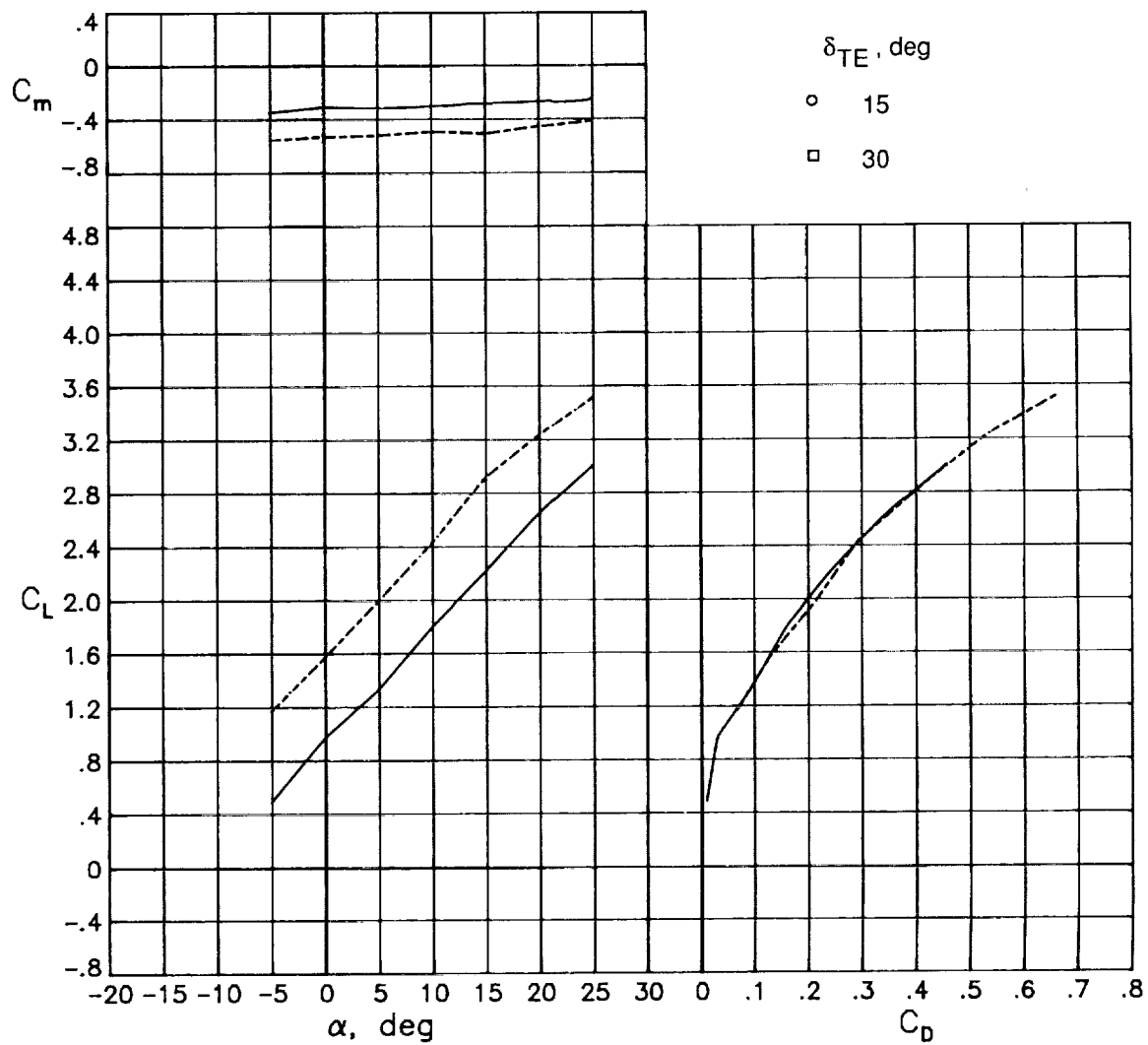
(b) VSAERO prediction.

Figure 26. Concluded.
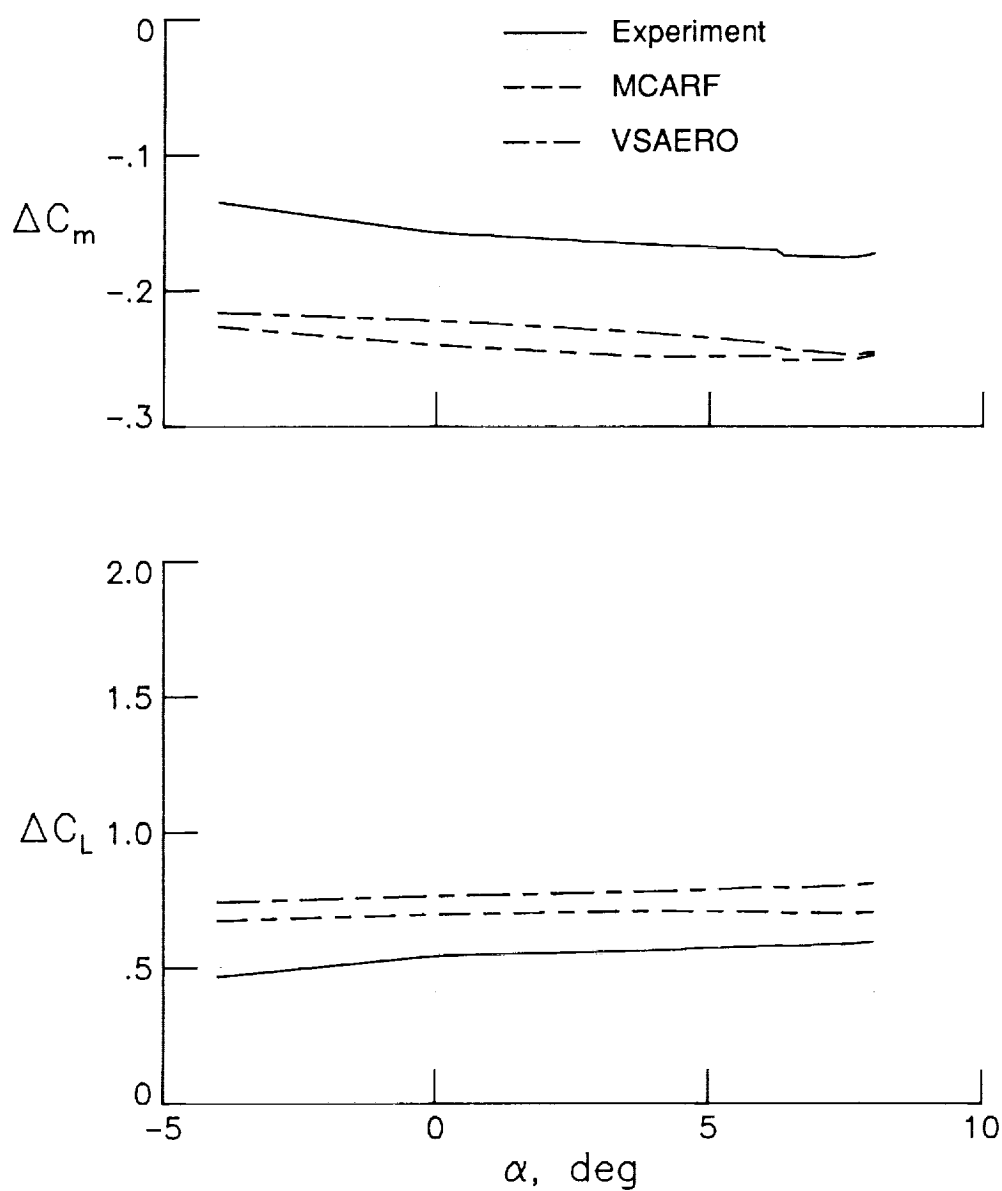
(a) Trailing-edge flap configuration; Δ for $\delta_{TE} = 15°$ − Cruise.

Figure 27. Predicted and measured effects of trailing-edge flap deflection on lift and pitching-moment coefficients. $q_\infty = 30$ psf.

(b) 10-percent leading-edge flap configuration; Δ for $\delta_{TE} = 30° - \delta_{TE} = 15°$.

Figure 27. Continued.

(c) 12-percent leading-edge flap configuration; Δ for $\delta_{TE} = 30° - \delta_{TE} = 15°$.

Figure 27. Concluded.
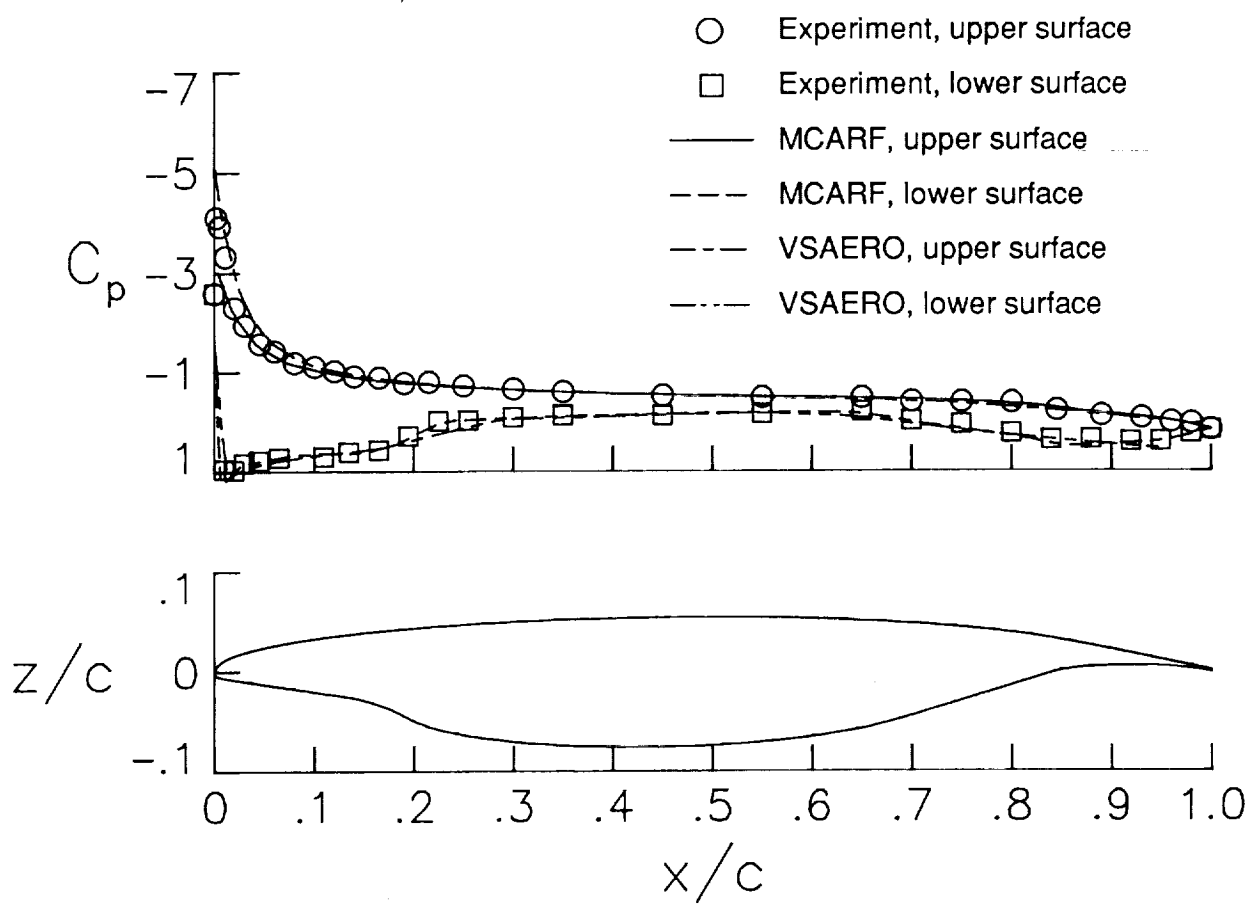
Figure 28. Predicted and measured pressure distributions for cruise configuration. $q_\infty = 30$ psf; $\alpha = 8°$.
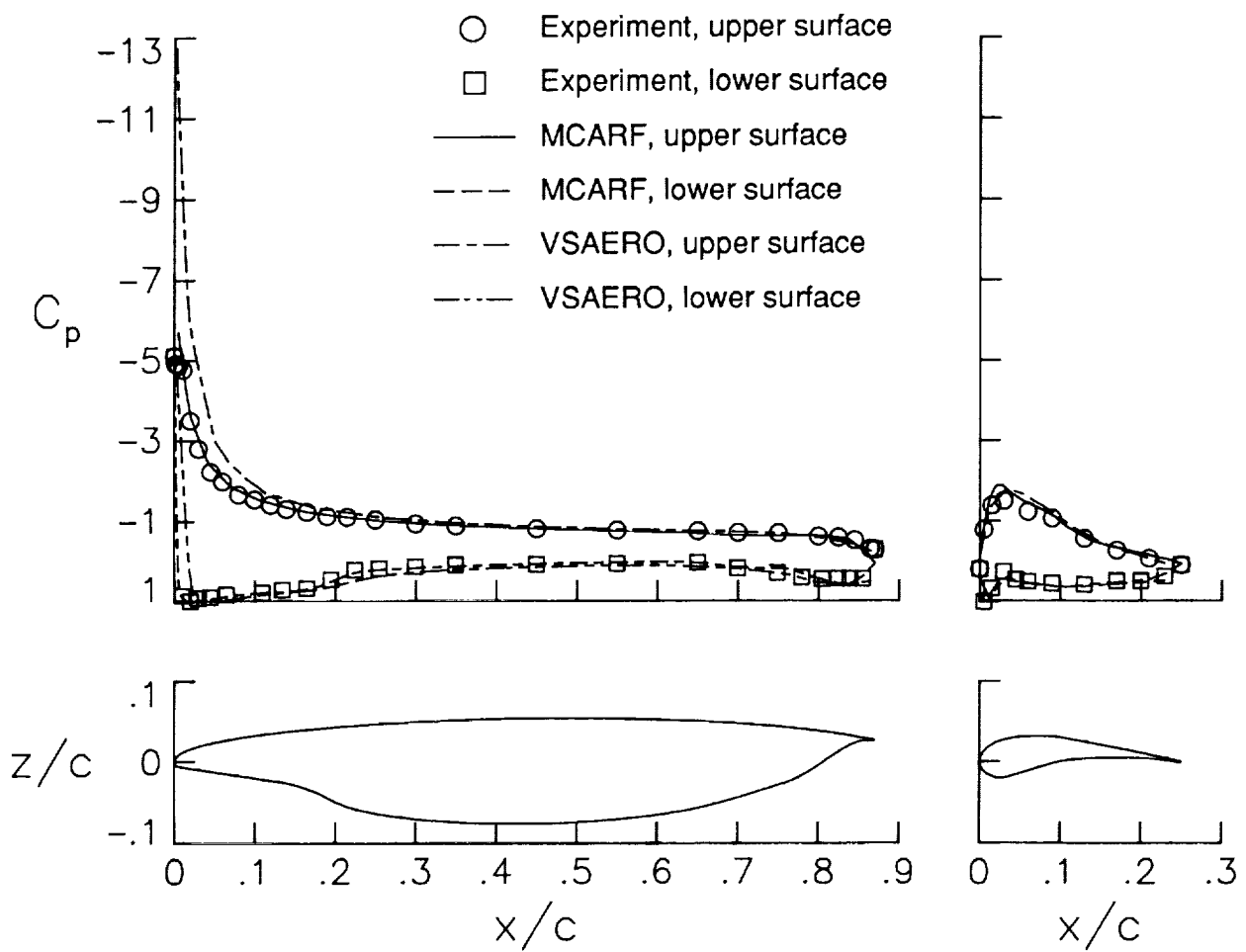
Figure 29. Predicted and measured pressure distributions for trailing-edge flap configuration. $\delta_{TE} = 15°$; $q_\infty = 30$ psf; $\alpha = 8°$.
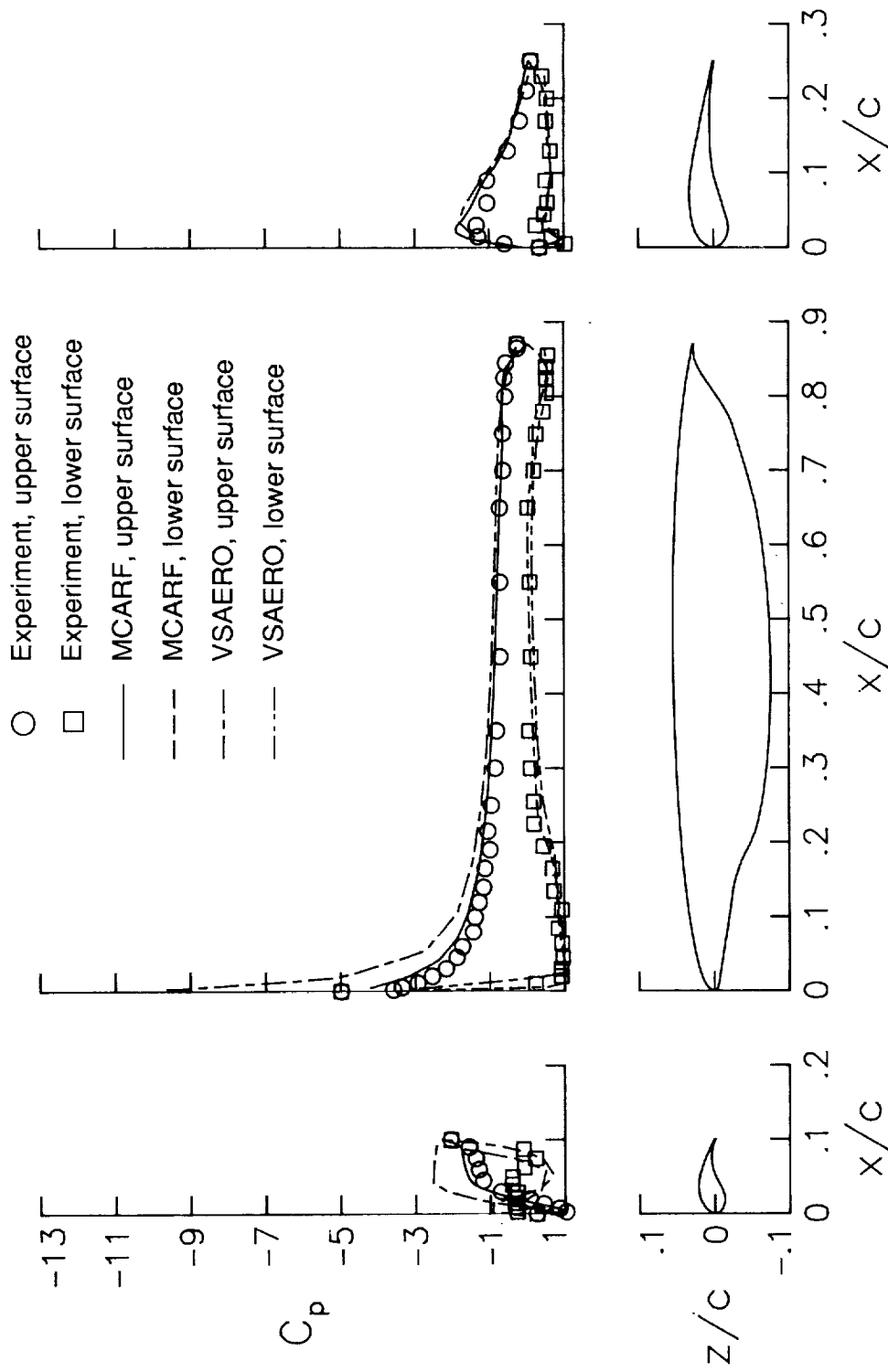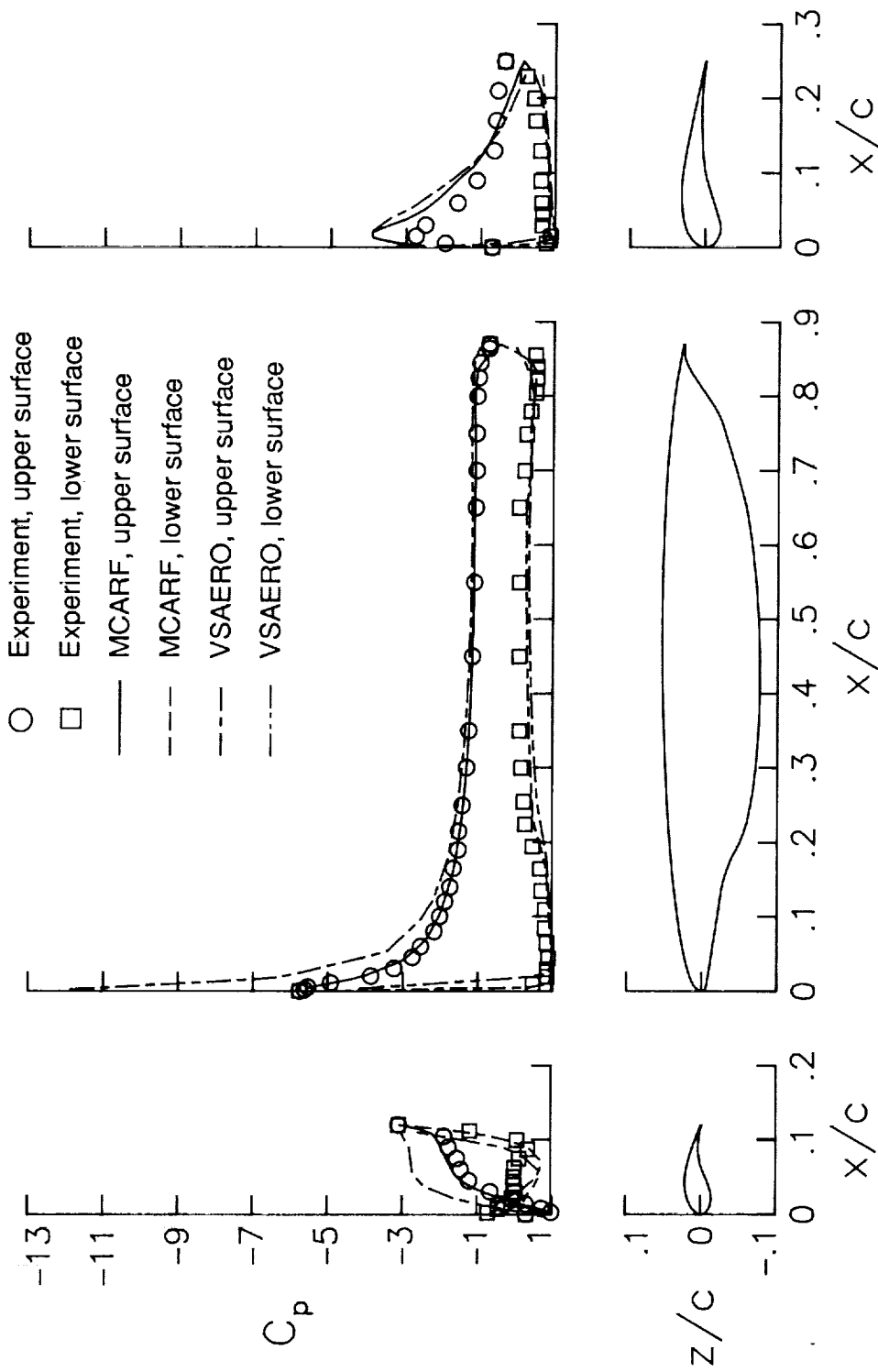
Figure 30. Predicted and measured pressure distributions for 10-percent leading-edge flap configuration. $\delta_{LE} = -55°$; $q_\infty = 30$ psf; $\alpha = 10°$.
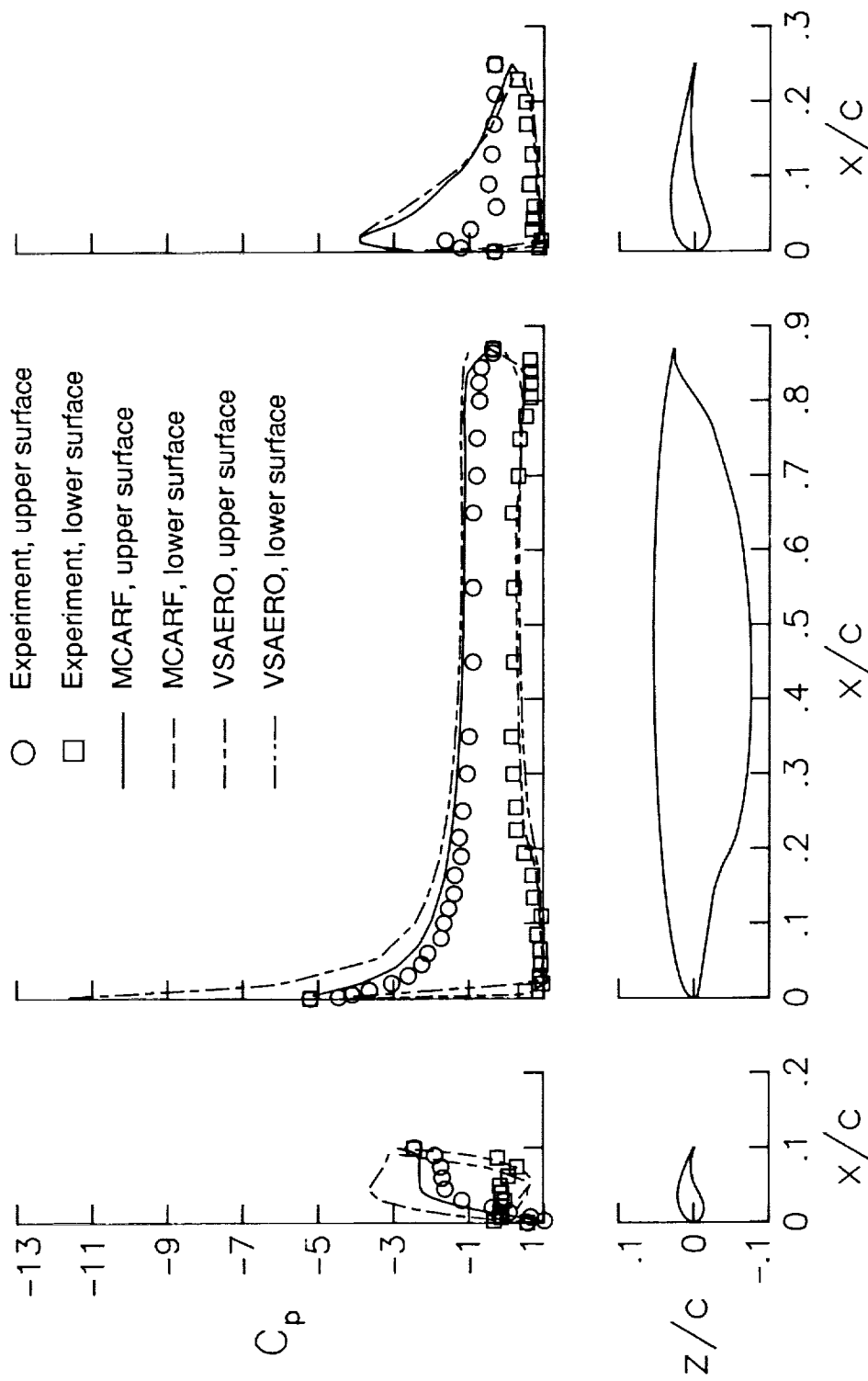
(a) $\delta_{TE} = 15°$.

(b) $\delta_{TE} = 30°$.

Figure 30. Concluded.
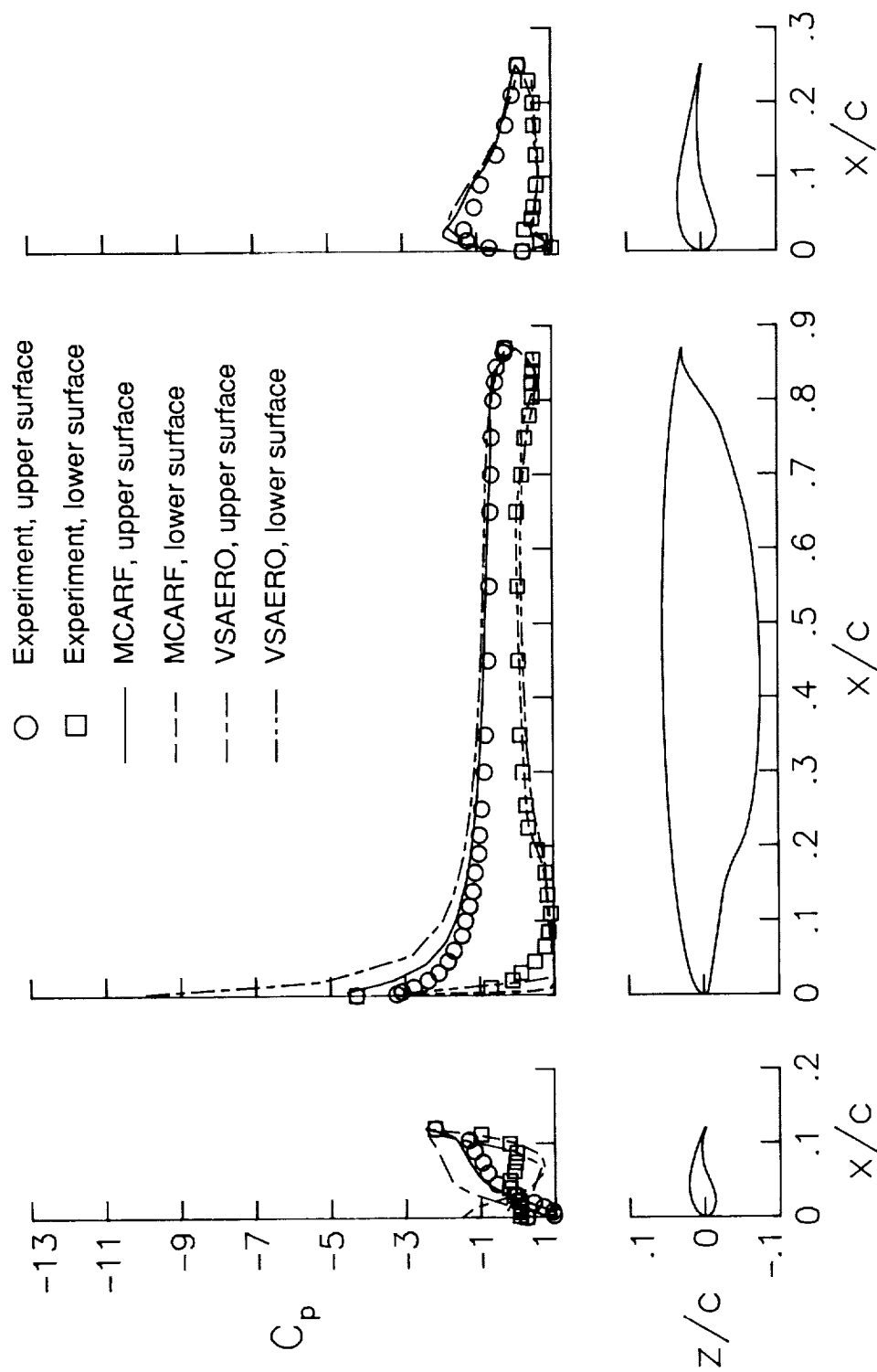
Figure 31. Predicted and measured pressure distributions for 12-percent leading-edge flap configuration. $\delta_{LE} = -55°$; $q_\infty = 30$ psf; $\alpha = 10°$.

(a) $\delta_{TE} = 15°$.

(b) $\delta_{TE} = 30°$.

Figure 31. Concluded.

16. Abstract

A study was conducted to compare experimental and theoretical aerodynamic characteristics of a high-lift semispan wing configuration that incorporated a slightly modified version of the NASA Advanced Laminar Flow Control airfoil section. The experimental investigation was conducted in the Langley 14- by 22-Foot Subsonic Tunnel at chord Reynolds numbers of 2.36×10^6 and 3.33×10^6. A two-dimensional airfoil code and a three-dimensional panel code were used to obtain aerodynamic predictions. Two-dimensional data were corrected for three-dimensional effects. Comparisons between predicted and measured values were made for the cruise configuration and for various high-lift configurations. Both codes predicted lift and pitching-moment coefficients that agreed well with experiment for the cruise configuration. These parameters were overpredicted for all high-lift configurations. Drag coefficient was underpredicted for all cases. Corrected two-dimensional pressure distributions typically agreed well with experiment, whereas the panel code overpredicted the leading-edge suction peak on the wing. One important feature missing from both these codes was a capability for separated flow analysis. The major cause of disparity between the measured data and predictions presented herein was attributed to separated flow conditions.